2019-07-30

Evaluating the utility of advanced MRI methods for monitoring structural changes in demyelinated lesions using two models of multiple sclerosis

Hossain, Md. Shahnewaz

UNIVERSITY OF CALGARY

Evaluating the utility of advanced MRI methods for monitoring structural changes in demyelinated lesions using two models of multiple sclerosis

by

Md. Shahnewaz Hossain

A THESIS

SUBMITTED TO THE FACULTY OF GRADUATE STUDIES

IN PARTIAL FULFILMENT OF THE REQUIREMENTS FOR THE

DEGREE OF MASTER OF SCIENCE

GRADUATE PROGRAM IN MEDICAL SCIENCE

CALGARY, ALBERTA

JULY, 2019

Thesis Abstract

The ability to precisely evaluate tissue pathologies and their functional correlates has been an ongoing challenge in patients with multiple sclerosis (MS). MS pathology is complex; however, much of them start from or are mediated by a demyelinating event. In this thesis, I have studied 2 common models of MS: a cuprizone mouse model, and an optic neuritis (ON) human model. I have particularly focused on the investigation of the potential of novel advanced magnetic resonance imaging (MRI) techniques including neurite orientation dispersion and density imaging (NODDI), diffusion tensor imaging (DTI), and MRI texture analysis. The first model evaluates the ability of these methods to assess the time course and regional preference of MS-like pathology following induced demyelination and spontaneous remyelination in mouse brain. The second model tests the feasibility of select imaging measures for detecting structural changes in the optic nerves and correlating clinical measures in acute optic neuritis (AON) as part of a clinical trial of high dose vitamin D. Through a focused study of the corpus callosum over an extended time series, the animal study shows that all MRI metrics have detected the expected changes over the de- and remyelination periods, consistent with histology quantified using a texture method, structure tensor analysis. The NODDI metric neurite density index is specific to myelin integrity, NODDI orientation dispersion index to axonal changes, and texture angular entropy specific to both myelin and axonal changes. Moreover, early de- and remyelination seems to occur in the genu of corpus callosum featuring relatively thin and high-density axons and early demyelination but relatively late repair in the splenium showing large caliber and comparably low-density axons. All NODDI metrics appear to outperform DTI metrics. In a clinical setting, the advanced imaging measures have successfully detected the structural changes in the affected versus non-affected optic nerves and angular entropy correlates with patient disability. Collectively, this thesis suggests that advanced MRI measures are powerful indices of MS-like pathology and could be used clinically for monitoring disease development and treatment responses, deserving further validation.

Preface

This thesis is the original work of the author, Md. Shahnewaz Hossain, prepared in the manuscript style format.

Chapter **Two** is an expanded version of a review in preparation at the time of this thesis submission

The data contained in Chapter **Three** make up a research manuscript in preparation for publication at the time of this thesis submission:

Chapter **Four** is part of an ongoing study and the basis of a future manuscript.

Acknowledgment

There are many people whom I would like to thank for their contributions, both directly and indirectly, to this thesis. I would first like to thank my supervisor, Dr. Yunyan Zhang. I will remain grateful to her for believing in my potentials and providing me the opportunity to work under her guidance. The example she sets as a leader is one I will aspire to if I ever find myself in a managerial role. She has inspired and guided me to work very hard to complete this thesis successfully. She somehow manages the mentorship of several graduate students, a lab that continues to grow in size, a list of committee involvements, and yet she is always there whenever you need her for support and guidance. I thank her for letting me try my strengths, for giving me the opportunity to fail at times, for encouraging me to learn new techniques and equipment, and for her constant support as my career goals have evolved. I appreciate her advice regarding academic, professional and personal life and look forward to always stay in touch with her in the future.

I am grateful to my graduate thesis advisory committee, Dr. Jodie Burton and Dr. Bradley Goodyear. Collectively, I would like to thank them for their continuous guidance and help in setting up my thesis project, analytical aspects as my thesis developed. Individually, I would like to thank Dr. Jodie, an excellent neurologist and one of the best mentors I have ever had, for always helping me keep perspective on where my research fits into the bigger picture and its clinical relevance. I would also like to thank Dr. Bradley Goodyear for consistently encouraging me to think of how to achieve accuracy in analyzing data and sharing his neuroimaging expertise in interpreting MRI outcomes. I would also like to thank my internal examination committee: Dr. Shigeki Tsutsui. Thank you for participating in my defense and thank you in advance for helping me strengthen my thesis.

Thanks to my friends and colleagues in my laboratory. Your kind support and endless source of advice have helped me immensely during my stay in this wonderful lab. Olayinka Oladosu taught me all the image processing software, was a source of support, adviser in science, and was a dear friend. Thanks to my present and past lab members Glen Pridham, Peng Zhai, Shrushrita Sharma, Zahra Hosseinpour, and Tim Lou for sharing your technical expertise. Now, I can realize the significance of teamwork toward success. Every single day has brought me new knowledge and experience in this journey.

Thanks to Dr. Vee Wee Yong and his lab for teaching me lab techniques, sharing their technical expertise, and continuous enthusiasm. Thanks to Dr. Andrew Vincent Caprariello, Dr. Vincent Ebacher from HBI AMP facility, David Rushforth from EIC, Dr. Wei Dong from MIF, Paul Romo from SFMRC for your technical support, advice, and good memories.

Thanks to my graduate program administrator Kiran Pandher and program director Dr. Paul Mains for their administrative support and my smooth transitioning into the program as an international graduate student.

I would like to convey my heartiest gratitude to my parents, who continuously inspired me to be what I am today. I am indebted to endless love, inspiration, and motivation from my siblings. Their support inspired me to believe in myself and to fight against all odds. And, lastly, thanks to my lovely wife for her inspiration, trust in me, and for being always there for me in my well and woes.

Table of Contents

Dedication

First of all, I want to dedicate this work to the most merciful Almighty Allah, who has gifted me this healthy life and granted me the opportunity to learn something new in every bit of my life.

To my mother **Sahida Begum**, father **Md. Delwar Hossain,** and my brothers **Shahriar Hossain and Shahadat Hossain** who believed in my ability and inspired me to stay strong.

And finally, to my beautiful wife **S. M. Nourin Sultana**. She is my best friend, my biggest fan, my source of motivation, and has been my strength in the most stressful moments of my life.

I feel honored to dedicate this work to the most precious persons of my life**.**

List of Tables

List of Figures

List of Abbreviations and Symbols

Abbreviations

AON	Acute optic neuritis
AD	Axial diffusivity
BOLD	Blood oxygen level dependent
C	Control
CHARMED	Composite hindered and restricted model of diffusion
Cho	Choline
CIS	Clinically isolated syndrome
CNS	Central nervous system
CPZ	Cuprizone
Cr	Creatinine
CSF	Cerebrospinal fluid
CV	Circular variance
DTI	Diffusion tensor imaging
DIR	Double inversion recovery
DWI	Diffusion-weighted imaging
EAE	Experimental autoimmune encephalitis
EC	Eriochrome cyanine R
EDSS	End disability status score
FA	Fractional anisotropy
FLAIR	Fluid-attenuated inversion recovery
fMRI	Functional MRI
FOV	Field of view
FT	Fourier transform
GCL	Ganglion cell layer
HARDI	High angular resolution diffusion imaging
^{1}H-MRS	Magnetic resonance spectroscopy
Ino	Inositol
Lac	Lactate

MBP	Myelin basic protein
MD	Mean diffusivity
MRI	Magnetic resonance imaging
MS	Multiple sclerosis
MTI	Magnetization transfer imaging
MTR	Magnetization transfer ratio
NODDI	Neurite orientation dispersion and density imaging
OCT	Optical coherence tomography
NAA	N-acetyl aspartate
NDI	Neurite density index
ODI	Orientation dispersion index
ON	Optic neuritis
OPC	Oligodendrocyte precursor cells
ORO	Oil red O
PFA	Paraformaldehyde
R^2	Coefficient of determination
RARE	Rapid imaging with refocused echoes
RAPD	Relative afferent pupillary defect
RD	Radial diffusivity
RF	Radio frequency
RNFL	Retinal nerve fiber layer
ROI	Region of interest
RRMS	Relapsing-remitting multiple sclerosis
SE	Standard error
SNR	Signal-to-noise ratio
SPIR	Selective partial inversion recovery
SPMS	Secondary progressive multiple sclerosis
STIR	Short tau inversion recovery
TE	Echo time
TEM	Transmission electron microscopy

TNF	Tumor necrosis factor
TR	Repetition time
VEP	Visual evoked potential
WAD	Week after diet
WOD	Week on diet

Symbols

B_0	Magnetic field
Mxy	Transverse magnetization
Mz	Longitudinal magnetization
1β	Interleukin
γ	Interferon
ω_0	Larmor frequency
ω	Frequencies

“An experiment is a question which science poses to Nature and a measurement is the recording of Nature's answer.”

— Max Planck

CHAPTER 1
Introduction

1.1 Overview of Multiple Sclerosis

Multiple sclerosis (MS) is a chronic inflammatory demyelinating and neurodegenerative disease of the central nervous system (CNS), affecting over 2.5 million individuals worldwide[1-3]. ~80% of the people start MS at 20-40 years of age and when their disease course still experiences recovery after an inflammatory demyelinating attack also known as relapsing-remitting MS (RRMS)[4]. However, many RRMS patients have already started to experience loss of neurological functions, making MS the most common cause of non-traumatic disability in young adults[5]. 10-15 years after disease onset, over 50% of RRMS patients follow a progressive course when physical disability increases relentlessly (secondary progressive MS)[6]. About 10-15% of MS patients experience disease progression directly from diagnosis (primary progressive MS)[7].

MS is the leading cause of non-traumatic neurological disability in young individuals. The prevalence of MS is 290 per 100,000 people in Canada, the so-called 'MS capital of the world'[8], affecting a total of 93,500 people; in fact, the prevalence rate in the prairies of Canada (Alberta, Saskatchewan, Manitoba) is the highest in the world, around 350 per 100,000 people[1]. MS is alarmingly on the rise and causes severe impact on individual health, social status, and economic stability.

MS patients present with a wide array of signs and symptoms affecting several parts of the body, vital to everyday function. Common MS deficits include vision problems, pain and spasms, muscle weakness, dizziness, tingling and numbness, fatigue, bladder issues, sexual dysfunction, and cognitive impairment[9]. The exact cause of the disease remains unknown. However, multiple factors may contribute[10] including latitude (i.e. distance from the equator/UV exposure), gender,

viral infection, low vitamin D level, and genetics[11]. Low serum vitamin D is thought to increase the susceptibility of MS in part in association with two genes, CYP27B1 and CYP24A1, which encode an enzyme that decreases serum vitamin D[12]. HLA-DRB1, considered as the strongest genetic predictor of MS risk, is also regulated by vitamin D[13]. People with MS typically have a mean serum 25(OH)D level of roughly 50 nmol/L, which is considered insufficient, and is lower than the values seen in the normal population (75-125 nmol/L) [14].

MS pathologically present either as both focal lesions[15] and diffuse abnormalities in the brain and spinal cord. The neurodegenerative changes in MS are thought to be in part due to inflammatory demyelination, axonal transection, and neuroaxonal loss in lesion and non-lesion areas. Much of The pathological change seen in MS are felt to be secondary to an autoimmune process targeting white matter which leads to an accumulation of astrocytes and microglia around the oligodendrocyte. Oligodendrocyte differentiation is then initiated through the release of cytokines and myelin sheath is damaged which results in neural signalling slowing or conduction block followed by glial scarring. If this damage occurs in an eloquent location, the patients will experience neurological deficits[16] (Fig. 1.1).

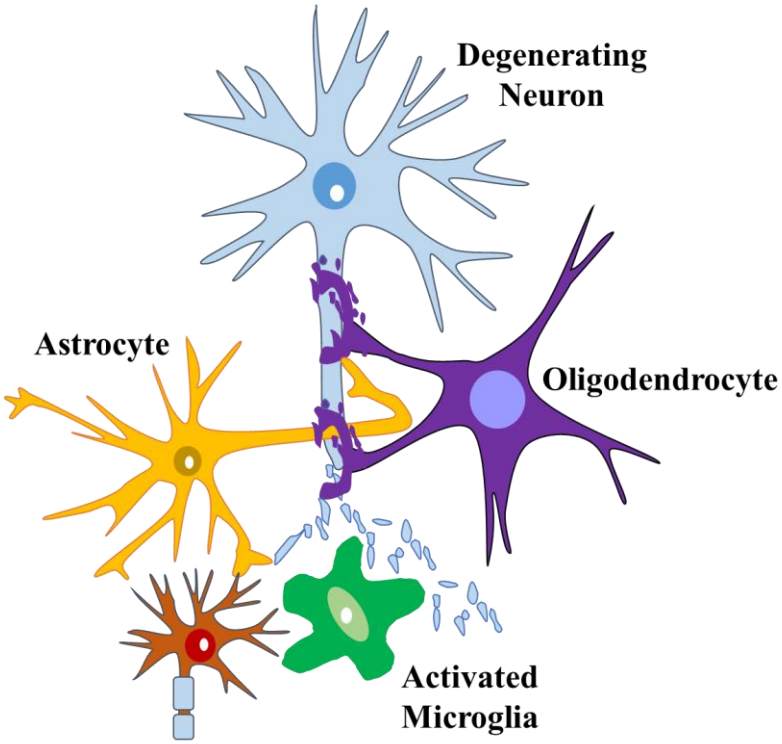

Fig. 1.1: MS pathology. A simplified schematic of pathological changes underlying MS (Image adapted from Henstridge CM *et al*[16]). Diagram showing lineage of oligodendrocyte and astrocytes leading to activation of microglia which aggravates neurodegeneration of axons.

Demyelination may occur early and be present throughout the disease process[15,17], causing ongoing axonal injury and disruption of any potential repair processes such as remyelination[15,18]. Demyelinated axons may remyelinate spontaneously after resolution of edema and inflammation, but is expected to only occur primarily during the early stages of the disease[18]; early repair may be enhanced by candidate treatments[19]. Remyelination is one of the critical repair processes in MS, allowing the reestablishment of structural integrity and protecting axons from neurodegeneration[20]. As the disease progresses, remyelination becomes increasingly incomplete and unpredictable due to the dynamic nature of MS[21]. Within an MS lesion, several pathological

processes may exist spontaneously including inflammation, demyelination, remyelination, and axonal changes[22,23]. These changes may interact with each other at any time, but when and how that occurs is unclear and unpredictable.

1.2 Overview of Research

Precise measurement of the dynamic processes including demyelination and remyelination is challenging in MS due to the complexity of the lesion environment and the unpredictability in timing and location of occurrence of disease processes. There are four different patterns of demyelination in MS. Pattern I and II exhibit T-cell mediated autoimmune encephalomyelitis and patterns III and IV involve oligodendrocyte dystrophy without autoimmune component of MS pathology[24]; all patterns exhibit different pathophysiology[25]. Pattern III demyelination distinguishes itself from other patterns by the relatively lesser degree of inflammation and considerable demyelination through extensive macrophage/microglia activation with oligodendrocyte apoptosis[24], which is the pattern of demyelination observed in the cuprizone mouse model and replicates demyelination in humans[26]. Histological analysis is able to provide informative snapshots of tissue pathologies, but these static manifestations lack the ability to fully describe ongoing dynamic processes[27]. Serial histological studies may help provide insight into disease development patterns and serve as a means for validating the *in vivo* measurements such as those derived from non-invasive imaging techniques.

Magnetic resonance imaging (MRI) plays a crucial role in the diagnosis and management of MS[28]. MRI permits non-invasive investigations of MS pathology. Conventional MRI methods have been successfully used in detecting lesions in MS and other demyelinating neurological disorders in the central nervous system (CNS), but conventional imaging methods are pathologically nonspecific[28,29]. Advanced MR imaging methods have shown improved specificity

to the pathological substrates of MS. While still under development, several MRI techniques warrant further validation. Example techniques that demonstrate the potential to detect both myelin and axonal properties include diffusion-based MRI such as diffusion tensor imaging (DTI), high angular resolution diffusion imaging (HARDI) based on neurite orientation dispersion and density (NODDI), and advanced image post-processing methods such as image texture analysis. Diffusion imaging indirectly measures the microstructural properties of a tissue using the random movement characteristics of water molecules; water moves more freely in tissue with fewer barriers such as along the long axis of axons and within damaged structures, leading to higher diffusivity[30]. Image texture analysis evaluates the distribution pattern of image pixels, which can be influenced by the integrity and organization of tissue structure. As such, this method highlights tissue properties more macroscopically than microscopically[31,32].

Given the complexity of MS pathology, relying completely on novel techniques may not be able to address all challenges, including the role of structural changes on patient function. In this regard, the use of pertinent disease models may help. There are couple of well-established animal models developed to probe the characteristics and evolution of MS pathology. One is the cuprizone model which results in demyelination of specific parts of the brain including both white matter tracts and grey matter and exhibits ongoing concurrent remyelination. Advantages of this model include ongoing axonal injury detection along with inter-relationship between remyelination and axonal survival in addition to studying demyelination whereas limitations include lack of inflammatory changes detection using this model[33]. Demyelination is achieved by feeding mice 0.2-0.3% cuprizone for 6 weeks to study acute demyelination and 12 weeks to study chronic demyelination[34]. This model features primarily de- and remyelination, but it also involves axonal loss, along with minimal inflammation[35-37]. Alternatively, optic neuritis (ON) in patients may

represent a robust model for understanding the consequences of inflammatory demyelination. Given the unique anatomy and anatomical location of the optic nerves and the accessibility of the afferent visual pathway, ON may also serve as a candidate model for interrogating the structural and functional relationships associated with MS. ON is a neuroinflammatory demyelinating disease of the optic nerves that occurs in around all MS patients and is the first presenting feature in 20-21% of MS patients[38,39]. Post-mortem studies of MS patients have revealed detectable optic nerve lesions in 94-99% MS patients[40,41]. Therefore, a study that includes both models may provide invaluable complementary information for understanding mechanisms associated with MS.

1.3 Hypothesis, Goals, and Specific Aims

The overall goal of this thesis is to identify and evaluate proof of concept that these new imaging techniques NODDI and texture angular entropy can qualify and possibly quantify tissue injury and repair in demyelinating diseases using the cuprizone and ON models of MS. I adapted multi-shell diffusion-weighted NODDI and MR Fourier transform (FT) power spectrum angular entropy texture measures to assess their ability to detect the structural integrity of nerve fibers in diffuse white matter areas in the CNS with variable degrees of de- and remyelination over time. I also investigated the presence and timing of pathological events such as de- and remyelination in different anatomical locations of corpus callosum, namely the genu, body, and splenium using NODDI and texture metrics, and compared them with conventional MRI measures. I validated my findings with a directly transferrable directionality based histology method, structure tensor analysis, in addition to conventional staining methods, using a toxin-induced mouse model of MS. I investigated the sensitivity of NODDI and texture angular entropy measures compared to conventional DTI measures. Finally, I tested the validated advanced imaging metrics in ON patients by determining whether they are able to detect the structural integrity of optic nerve.

My overarching hypothesis was that high angular resolution diffusion imaging NODDI and MRI texture analysis indices will bring additional information about de- and remyelination above and beyond current conventional MRI methods, and behave predictably, with regards to the structural properties of demyelinated lesions.

My specific aims are:

Aim 1: To evaluate if advanced MRI methods NODDI and texture angular entropy correlate with existing MRI methods and histological changes in the murine cuprizone model of MS with regard to de- and remyelination.

Aim 2: To evaluate the quality of information provided by novel and validated MRI measures of structural integrity and injury within the afferent visual pathway of patients with acute optic neuritis (AON).

1.4 Thesis Organization

Chapter one gives a brief overview of MS, the research goals, hypothesis, specific aims, and the structural organization of the thesis.

Chapter two is literature review describing the animal models commonly used in MS, and a systematic review of ON as a model of MS. This systematic review in this chapter includes currently available conventional and advanced MRI imaging techniques used in ON and MS and in measuring tissue injury and repair in general, followed by emerging MRI techniques and image post-processing methods including NODDI, along with its acquisition and application in demyelinating diseases. The review of image post-processing methods particularly highlights the utility of image texture analysis techniques, including a tissue directionality-based measurement approach known as structure tensor analysis, a promising method for quantitative analysis of histology images used to validate MRI. Prior to the MR imaging techniques, this chapter also

provides a brief overview of the methods commonly used for ON patients such as visual evoked potentials (VEPs) and optical coherence tomography (OCT).

Chapter three focuses on the effort to evaluate the ability of advanced MRI methods in characterizing evolving tissue pathology using the cuprizone model of MS. This study focuses on diffusion-based NODDI outcomes and the use of MR texture angular entropy in detecting de- and remyelination-driven pathological processes occurring in a distinct white matter structure, the corpus callosum. This chapter also correlates the findings of advanced imaging metrics with structure tensor analysis outcomes derived from myelin and axon stained images. The relationship between tissue morphology, such as axonal density and diameter in different corpus callosum regions, and MRI metrics is also explored. In addition, the chapter describes the sensitivity of advanced MRI metrics to myelin and axonal status, in comparison it with conventional MRI metrics.

Chapter four investigates the feasibility of advanced MRI and image texture analysis methods to detect the structural integrity of the optic nerves in patients with AON. The texture analysis is performed on clinically viable anatomical MR images of ON patients focusing on the lesion and non-lesion areas of the optic nerve, and the outcomes are compared between techniques. In addition, the chapter further investigates different MRI sequences for their ability to detect brain lesions in ON patients and correlates MRI metrics with available clinical measures.

Finally, **Chapter five** summarizes the key findings of this thesis, briefly discusses future directions to further enhance the utility of the thesis findings, and highlights the importance of this work in understanding disease progression in demyelinating diseases including MS and ON.

CHAPTER 2

Overview of the modeling and measurement strategies in MS

The use of dedicated models may help overcome some of the challenges in characterizing MS, thereby enhancing our understanding of disease mechanisms. Animal models can provide further insight into specific processes of MS pathology including de- and remyelination, and axonal injury[19]. In contrast, the ON model may be unprecedented in advancing our understanding of the consequences of inflammatory demyelination and the structural and functional relationships in MS. This chapter will present an overview of these two modeling approaches and the measurement methods associated with these models, and CNS de- and remyelination in general.

2.1 De- and Remyelination in MS

Inflammatory changes in the CNS can result in damage to the protective myelin sheath of neuronal axons known as demyelination, causing multiple areas of scar tissue around the nerve fibers and is the hallmark of MS[9]. Myelin is the protective layer of axons and is responsible for saltatory conduction across axonal nerve fibers[19] and provides trophic and ultrastructural support to the axons[33]. This protective myelin sheath layer and myelin forming cells (oligodendrocytes and their precursor cells) are damaged during demyelination, which in turn can lead to axonal injury[17,42]. Demyelination is observed throughout the CNS and both grey and white matter are affected[17] but typically white matter changes are looked upon due to the harder assessment of grey matter changes. Demyelination leads to impaired conduction of nerve impulses along the nerve fibers and is associated with a variety of neurological symptoms[43]. Ex-vivo, demyelination can be evaluated using a variety of histochemistry measures. These measures involve quantifying histology sections through myelin-specific staining such as eriochrome cyanine R (EC) or myelin

basic protein (MBP) and using ultrastructure imaging. But histology measures are site and time specific, limiting its ability to detect heterogeneous, dynamic pathology or a large region of interest (ROI)[27]. Non-invasive MRI has been used to qualify and quantify these pathological processes. Several advanced MRI metrics have shown sensitivity to specific pathological processes underlying MS[44].

MS pathology in the CNS is thought to involve inflammatory demyelination, axonal transection, and neuronal loss in the lesion and surrounding areas. There is also an early degenerative aspect of MS that is less well understood. Spontaneous remyelination is often seen in patients with acute MS attacks[45,46]. Spontaneous remyelination is hampered if axons are severely damaged after demyelination or are transected due to direct injury (Fig. 2.1)[43]. Oligodendrocyte precursor cells (OPC) may accumulate at the lesion site following demyelination and differentiate into mature oligodendrocytes (Fig. 2.2), creating functional myelin sheaths and facilitating myelination repair[47]. Macrophages can infiltrate the lesion site to clear out myelin debris prior to remyelination for optimal OPC survival[48]. Remyelination can be measured *ex-vivo* using specific stains or quantitative indices such as g-ratio. G-ratio quantifies the ratio between the axonal circumference to the remyelinated axonal circumference and is always less than 1. The smaller the g-ratio, the higher the degree of myelination (Fig. 2.3)[25,49]. Remyelinated axons are almost always shorter and thinner than healthy axons. Remyelination varies across tissues according to disease mechanisms, and it becomes insufficient, and eventually fails at later stages of the disease[47]. Earlier recovery/remyelination thus plays a vital role in enhancing functionality and neurological recovery of MS patients. Given the heterogeneity of pathological events underlying MS, non-invasive biomarkers are highly sought after. MR imaging measures validated through specific animal models may help in this regard[50].

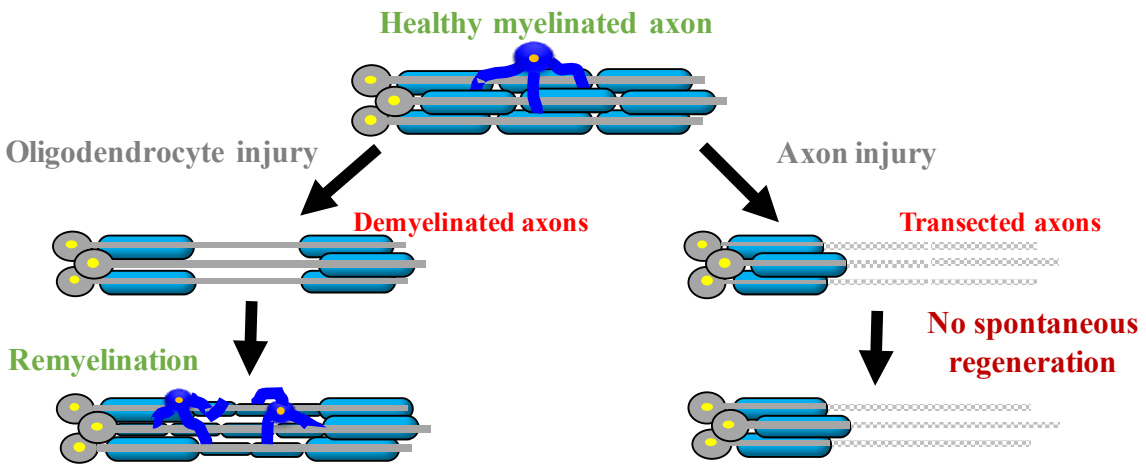

Fig. 2.1: De- and remyelination in MS. A simplified pictorial demonstration of de- and remyelination. Remyelination status is dependent on the mode of injury incurred by the axons. Injury to axons followed by oligodendrocyte dystrophy undergoes spontaneous remyelination after removal of tissue insult but permanent damage such as transected axons shows relatively low or no concurrent remyelination following injury (Diagram adapted from Lubetzki *et al.*[43]).

2.2 Animal Models of MS

Animal models are very suitable for investigating MS pathology, particularly in terms of white matter lesion injury and repair[51]. Although experimental autoimmune encephalomyelitis (EAE) is one of the most commonly used methods to study MS pathophysiology[51], comprehensive investigation of dynamic processes like de- and remyelination is challenging due to the unpredictability of the occurrence and location of demyelination[52]. Toxin-induced animal models are frequently used as preclinical models to study MS pathophysiology due to their ability to capture focal de- and remyelination, as they specifically target oligodendrocytes without affecting other cells, and they are established for studying processes related to de- and remyelination over

time[26,51]. Most commonly used toxic models of MS are cuprizone, lysolecithin, and ethidium bromide models. The cuprizone and lysolecithin models are more established to study both acute and chronic demyelination and progressive remyelination and the latter is commonly used to study chronic inflammatory demyelination and axonal loss[53].

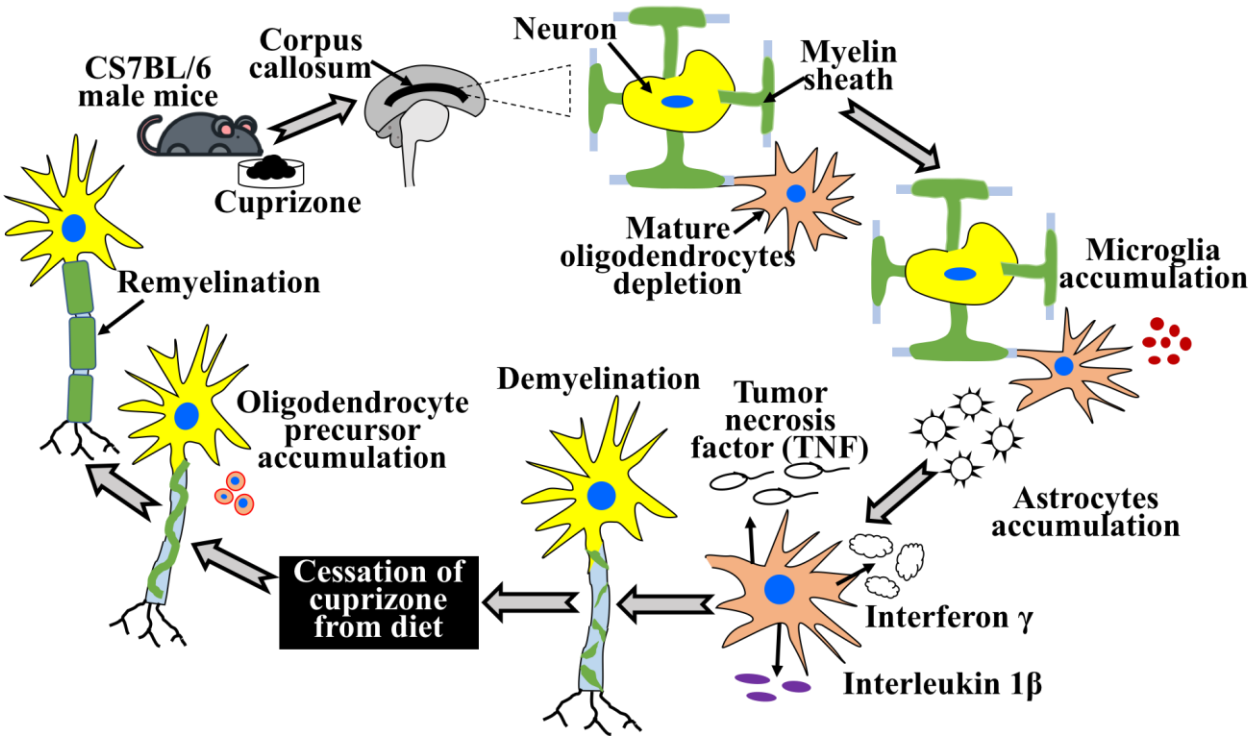

Fig. 2.2: MS pathogenesis in cuprizone mouse model. A schematic of the mechanisms of de- and remyelination after cuprizone induction in C57BL/6 male mice (Image adapted from Praet J *et al.*[54] and Gudi V *et al.*[36]). Cuprizone administration facilitates lineage of mature oligodendrocyte depletion leading to accumulation of microglia and release of cytokines, leading to demyelination. Removal of cuprizone from diet initiates accumulation of oligodendrocyte precursor/progenitor cells resulting in differentiation of oligodendrocyte progenitor cells and remyelination is seen.

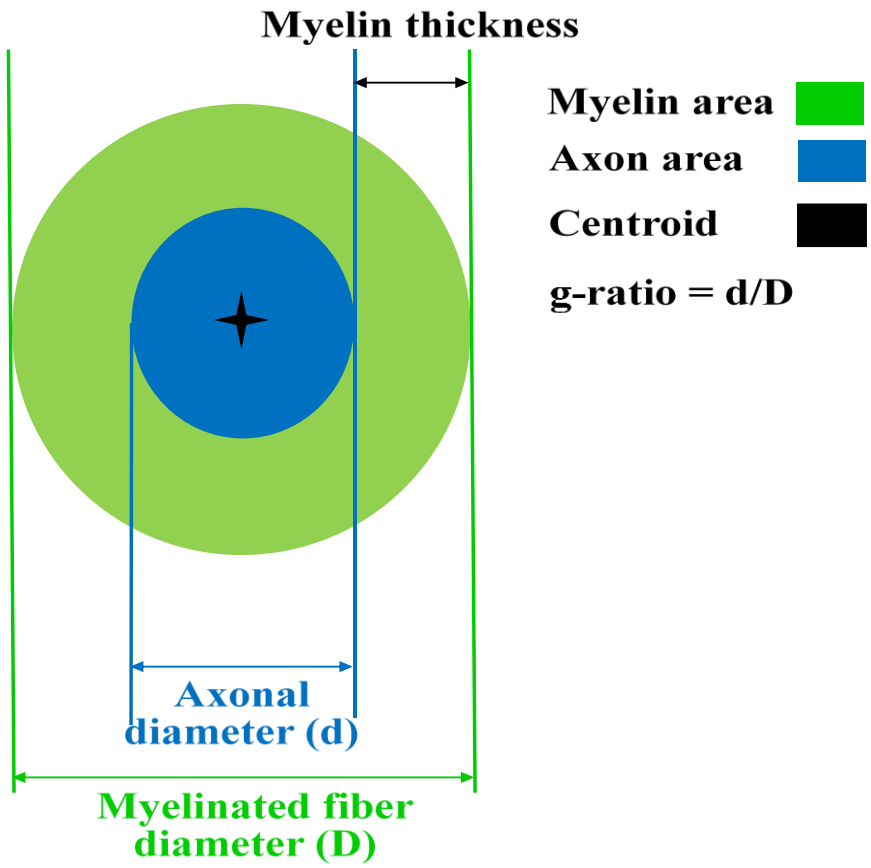

Fig. 2.3: Myelin g-ratio. A schematic of myelin g-ratio (Image adapted from Zaimi A *et al.*[49]). G-ratio gives information on myelin status from ratio of axon diameter compared to myelinated axon diameter. lower the g-ratio, higher the myelination.

2.2.1 The Cuprizone Model

Copper chelating agent cuprizone (bis-cyclohexanone-oxaldihydrazone) acts as a neurotoxin in murine animal models, which can induce tissue injury (i.e. demyelination) in a controlled way in distinct anatomical regions, most eminently within in the corpus callosum. This is typically followed by spontaneous remyelination after elimination of neurotoxin[25,34]. The pathology followed by cuprizone ingestion in a specific mouse strain (C57BL/6) is well defined and highly

reproducible[55]. Although the exact pathology behind cuprizone-induced demyelination is not known, it may be due to innate immune responses brought on by the toxic effects of cuprizone itself[56]. Cuprizone inhibits copper-dependent mitochondrial enzymes, cytochrome and monochrome oxidase, leading to apoptosis of mature oligodendrocytes in the CNS and inducing demyelination[34,57]. The mechanism underlying cuprizone-induced demyelination is thought to involve depletion of mature oligodendrocytes by the copper chelator cuprizone through direct killing. This leads microglia and astrocytes to accumulate around the affected oligodendrocyte and cytokines such as tumor necrosis factor (TNF), Interferon γ, and Interleukin 1β are released resulting in pro-inflammatory demyelination of axons. After removal of cuprizone from the diet, oligodendrocyte precursors accumulate around the affected axons and spontaneous remyelination is observed[54] (Fig. 2.2). Almost complete remyelination can be seen in demyelinated brain regions after removal of the toxin following cuprizone induction for 5 - 6 weeks which follows concurring remyelination even after continuation of cuprizone feeding[58]. Thus, cuprizone is induced for 6 weeks to see acute demyelination and up to 12 weeks to see chronic demyelination[34]. Cuprizone is an ideal and one of the most widely used model to study de- and remyelination, as this model produces these pathological events with minimal inflammation and keeping the blood-brain-barrier intact[35-37]. Disruption of the blood-brain barrier activates multiple contributing factors such as T-cell activation and creates a complex pathological process[59], not confined to de- and remyelination. Thus, it has widely been used for studying de- and remyelination and axonal changes[25]. The corpus callosum is also a major diseased area in MS, as this area shows lesions in more than 90% of the patients[60]. Although the corpus callosum is the primary target area to see pathological processes associated with de- and remyelination in this model, other white matter structures such as the dorsal hippocampal commissure and gray matter cortex have also shown

demyelination due to ingestion of cuprizone in mouse models[34,61,62]. C57BL/6 is the commonest strain used in the cuprizone mouse model, and male mice have been generally used in almost all studies conducted using this model[63]. Cuprizone is usually fed to 8 week old mice for a period of 6 - 12 weeks to detect acute and chronic demyelination, with a dosage of 0.2 - 0.3% (w/w) cuprizone mixed with normal rodent chaw. Spontaneous remyelination is observed immediately after cessation of cuprizone from the diet, and complete remyelination is thought to occur 8 weeks after[34]. This model enables well-characterized timelines for MRI to study tissue injury and repair simultaneously in a comprehensive way. The pros of cuprizone model includes ongoing axonal injury detection along with de- and remyelination which helps identify the relationship between axon and myelin in neurodegeneration[64]. The cons of cuprizone model includes higher induction time and effort to successfully implement this model in animals regardless of sample size and ongoing futile remyelination with concurrent demyelination which can lead to missed remyelination and faulty prediction of demyelination[65]. Also the involvement of immune system in MS is overlooked in cuprizone mouse model, thus, misses genetic aspects of complex MS pathogenesis[66].

2.2.2. Other Animal Models of MS

Lysolecithin (Lysophosphatidyl choline) is a commonly used toxin to induce robust focal demyelination in white matter, which is followed by spontaneous remyelination[19]. Lysolecithin causes focal demyelination in any white matter tracts regardless of age, gender, strain, and type of animal used[64]. Lysolecithin has successfully induced demyelination at the dorsal column of the thoracolumbar level of the spinal cord in mouse, rat, rabbit and cat, and has demonstrated de- and remyelination within 30 days of administration[67]. Focal demyelination has also been generated in the ventral aspect of the spinal cord white matter at the thoracic (T3 - T4) level using lysolecithin.

Alternatively, it is effective in the brain white matter tracts by introducing 0.5 µl of 1% lysolecithin in combination with other pharmacological/chemical compounds or alone by stereotaxic instrument, to see disease mechanisms and potential translational therapeutics for MS[19,52]. In either the brain or spinal cord, demyelination can be observed 1 - 3 days' post lysolecithin injection, and extensive demyelination is seen 7 - 10 days after. Remyelination in this model becomes prominent at 21- 28 days post-injection[52,68]. Lysolecithin causes active demyelination by administering a detergent effect of the toxin directly over the myelin sheath. However, lysolecithin does not affect the oligodendrocytes initially. Spontaneous accumulation of glial progenitor cells and their differentiation results in progressive remyelination[69]. Recruitment of T and B cells along with macrophages at the affected injury site after induction of lysolecithin also plays a positive role in the promotion of remyelination[67]. The spatiotemporal predictability of lysolecithin lesions has made this model advantageous for studying acute focal changes. Nevertheless, the challenges associated with producing injury at a specific site due to involvement of stereotaxic surgery and operator variability has limited its usage[70].

The experimental autoimmune encephalomyelitis (EAE) is probably the most commonly used animal model of MS due to its detection of complex autoimmune inflammation nature of the disease along with detection of concurrent demyelination and axonal loss[66]. EAE is initiated by either active immunization with myelin-derived proteins (myelin oligodendrocyte glycoprotein or myelin basic protein) or peptide in adjuvant, or by passive immunization by transferring activated myelin-specific CD4+ T lymphocytes[51]. Advantages includes similarities in inflammatory injury between EAE and MS and limitations includes flawed detection of remyelination repair with ongoing inflammation[33].

2.3 The ON Model of MS

ON is an inflammatory demyelinating disease of the optic nerve, followed by various degrees of axonal injury, gliosis, and repair[71]. In MS, ON is typically unilateral, whereas, in conditions such as neuromyelitis optica, it can be bilateral[72]. In either case, the afferent visual system is the main pathological target ranging from the retina, optic nerve, optic tracts, to the optic radiation, and visual cortex[73]. Common optic nerve involvement includes neuroretinitis of the optic disc, papillitis affecting the orbital optic nerve, retrobulbar neuritis affecting optic nerve behind the eyeball, and perineuritis that affects the optic nerve sheath.

The symptoms and signs of ON can present as a range of dysfunction. Central visual acuity loss is the hallmark of ON[74], likely due to conduction block of the optic nerve resulting from inflammatory demyelination, particularly during the acute phase[75]. Other symptoms include loss of color vision, pain during eye movement, and transient flashes of light[39]. In 1/3 of ON patients, there are also aberrant contrast sensitivity and visual field defects[74]. In unilateral ON, a relative afferent pupillary defect (RAPD) is commonly detected on exam[76]. The prevalence of ON is high in Caucasian, adult females, and those living in temperate regions, which also describes the prevalence of MS as well[29]. Recovery is often relatively rapid (within a matter of weeks) and often leads to a return to normal vision, likely due to remyelination and compensatory neuronal recruitment[77], and many people recover irrespective of treatment received[78,79].

ON can serve as a useful and relatively manageable model of MS, as both are impacted by inflammation, de- and remyelination, and axonal changes[22,23]. In AON, injury to the optic nerve corresponds to acute injury that impacts areas of the brain that subserve vision downstream[80]. Likewise, ON is the first presenting feature in 20 - 21% of MS patients[39,81,82], and >90% of MS patients show optic nerve lesions based on postmortem evidence[83]. Involvement of retrochiasmal

pathways is also common in MS[40]. Currently, various assessment tools exist in MS; however, it is difficult to correlate specific changes in structure to function. The optic nerve is the most approachable site of the CNS, which allows for a reliable and independent measurement of both structural and functional consequences of inflammatory demyelination[74,84]. Further, signs and symptoms of ON recover much faster than many other manifestations of MS, so it is also possible using this model to develop new therapies for both ON and MS patients[85]. In any case, a precise assessment of tissue injury and repair in ON is critical.

2.4 Measurement Strategies for ON

Investigations of ON focus on both acute diagnoses and disease monitoring. ON diagnosis requires thorough ophthalmic and neurological examination in addition to a detailed history, particularly for those with danger signs such as pain during eye movements and severe visual impairment, to exclude other diseases[86,87]. Ophthalmic examination includes pupillary and color vision assessment, evaluation for vitreous cells, dilated retinal examination, visual acuity, contrast, and field[88]. Neurological examination can detect evidence of involvement of other parts of the CNS, or systemic features that would suggest an alternative diagnosis[89]. In addition, screening for conditions such as sarcoidosis, neuromyelitis optica, anti-MOG disease, and collagen vascular disease requires serum and possibly cerebrospinal fluid (CSF) testing[90]. Improved and sophisticated imaging techniques have provided a unique opportunity for precise characterization of disease mechanisms and progression in ON, namely MRI approaches[74,87]. The visual pathway is one of the most understood and accessible parts of the CNS. Characterizing injury and repair mechanisms of ON, therefore, offers a unique opportunity for evaluating the consequences of inflammatory demyelination as commonly seen in MS. Several imaging metrics generated by

different imaging modalities suggests diverse pathological changes in ON and MS associated with underlying pathophysiology (Table 2.1).

2.5 Clinical Imaging Measures of Injury and Repair Associated with ON

2.5.1 OCT

OCT is a non-invasive ocular imaging technique that has become instrumental in assessing microstructural changes in ON, such as those in the retinal nerve fiber layer (RNFL) and ganglion cell layer (GCL)[91]. As these areas are nearly devoid of myelin, OCT serves as an ideal tool for dissociating the relationship between myelin and axons[92]. Acutely, there is often an increase in RNFL thickness in OCT with ON due to inflammation, followed by thinning secondary to atrophy[73,93,94]. Similarly, OCT has also shown sensitivity for detecting retinal ganglion cell dissociation in the macula after ON, equivalent to gray matter atrophy in MS[95,96]. Alternatively, visual recovery in patients with ON correlates to improvement in OCT-detected RNFL and GCL thickness[97,98]. There are two types of OCT available: time-domain OCT and spectral-domain OCT. Spectral-domain OCT has several advantages over time-domain OCT including better image resolution[99]. Spectral-domain OCT images of retinal layers correspond very well with disease progression of ON[100]. In addition, OCT can detect changes in RNFL thickness in the contralateral eye as early as two months after ON[101]. Therefore, given the promise of OCT, it has been used extensively in both clinical and research studies of ON. Nonetheless, due to the mechanism of OCT of passing light waves and collecting scans, it cannot detect underlying disease pathology precisely if the passing medium is opaque, which is common in acute conditions like AON due to underlying inflammation[99]. Previously, most of the OCT images were from time-domain OCT, and now most OCT images are spectral domain; as retinal RNFL thickness measured by these two modalities are not comparable, a significant number of data cannot be compared[93,102].

Table 2.1: Imaging metrics generated by different imaging modalities in ON and MS and their pathophysiological associations (adapted from Kolappan *et al.*[103] and Burton EV *et al.*[104]).

Imaging Modality	**Imaging Metrics/measures in ON and MS**	**Changes in metrics reflecting the pathophysiology**	
		Optic nerve	**Brain**
T1-weighted MRI	Hypointense lesion	Demyelination, edema	Acute state of the disease
	Conversion from hypointensity to isointensity of lesions	Resolution of inflammation	Repair
	Brain volume	Atrophy through thalamic measurements	Atrophy
Contrast-enhanced T1-weighted MRI	Gadolinium-enhancement	Neurodegeneration	Inflammation
	Hyperintense lesion	Inflammation, visual deficit	Active disease status, inflammation, and relapse
	Cessation of enhancement over time scan	Repair	Repair
T2-weighted MRI	Hyperintense lesion	Neuronal loss, loss of visual acuity	Edema, inflammation, demyelination, axonal

Imaging Modality	Imaging Metrics/measures in ON and MS	Changes in metrics reflecting the pathophysiology	
		Optic nerve	Brain
			loss, and gliosis
	Brain volume		Measurement of atrophy
STIR imaging	Hyperintense lesion	Neuronal loss, decreased optic nerve thickness	Neuronal loss around CSF
FLAIR imaging	Hyperintense lesion	Neurodegeneration ,decreased macular volume	Cortical and white matter neurodegeneration
	Hyperintense optic nerve sheath	Inflammation	
MTI	Brain Parenchymal Fraction (BPF) decrease		Atrophy
	MTR decrease	Axonal degeneration, demyelination	Axonal loss
	MTR increase	Myelination, repair	Remyelination
DTI	MD increase	Inflammation	Inflammation
	AD decrease, RD increase, and FA decrease	Axonal damage, demyelination, neurodegeneration	Axonal damage, demyelination, neurodegeneration

Imaging Modality	**Imaging Metrics/measures in ON and MS**	**Changes in metrics reflecting the pathophysiology**	
		Optic nerve	**Brain**
NODDI	ODI increase, NDI decrease	Neurite dispersion, demyelination, axonal loss	Neurite dispersion, demyelination, axonal loss
	ODI decrease, NDI increase	Repair, remyelination	Repair, remyelination
fMRI	BOLD signal decrease	Diminished visual function and reduced neuronal input	Neurodegeneration
	BOLD signal increase	Visual recovery and adaptation	Repair
^{1}H-MRS	NAA, NAA/Cr decrease	Neurodegeneration, inflammation	Axonal loss
	NAA, NAA/Cr increase	Recovery, resolution of inflammation	Recovery
Texture Analysis from T2-weighted MRI	For FT power spectrum: Angular entropy increase	Demyelination, tissue injury	Demyelination, tissue injury
	Angular entropy decrease	Remyelination, repair	Remyelination, repair
OCT	RNFL thickness decrease	Recovery of visual function, repair	
	RNFL thinning increase		

Imaging Modality	Imaging Metrics/measures in ON and MS	Changes in metrics reflecting the pathophysiology	
		Optic nerve	**Brain**
		Axonal loss, visual function deficit	
VEP	VEP amplitude and latency decrease	Neuronal loss, neurodegeneration	
	VEP latency and conduction increase	Repair, visual recovery	

Short tau inversion recovery (STIR), Fluid-attenuated inversion recovery (FLAIR), Magnetization transfer imaging (MTI), Diffusion tensor imaging (DTI), Neurite orientation dispersion and density imaging (NODDI), Functional MRI (fMRI), Magnetic resonance spectroscopy (^{1}H-MRS), Fourier transformation (FT), Optical coherence tomography (OCT), Visual evoked potential (VEP)

2.5.2 VEP

The VEP tests the functional integrity of the visual pathway and is recorded by electrodes placed on the scalp over brain centers responsible for visual activities[105,106]. There are two types of VEPs: conventional VEP and multifocal VEP. Multifocal VEP is more frequently used due to its higher spatial resolution, more accurate detection of ON/MS, and more reliable detection of underlying pathology due to a higher coverage over multiple directional orientation[107,108]. The waveform of the multifocal electroretinogram signal generates latency and amplitude information

when passing from the unmyelinated retinal ganglion cell axons to the myelinated portion of the optic nerve (post-lamina cribosa)[109].

VEPs can provide information on both myelin integrity and RNFL thickness in the visual field[110]. For example, latency prolongation and amplitude decline of the main VEP waveform highlights conduction delay or block, representing demyelination. In addition, reduced VEP amplitude from conduction block may also reflect axonal damage, as shown by a study suggesting that early prolongation of VEP latency predicts acute degeneration of demyelinated axons occurring during acute inflammation, consistent with evidence from OCT[91]. The ability of VEP to measure electrophysiological activity of both eyes makes it an essential tool for diagnosis and monitoring of ON. VEP may be more effective than OCT in measuring clinical and subclinical ON in some cases. In one study, the sensitivity of VEP was 21% higher than OCT in measuring RNFL after ON in the affected eye. In the same study, VEP showed a 75% accuracy in detecting subclinical abnormalities of ON in the affected eye, in contrast to OCT which was accurate in less than 1/5th of patients[111]. Many other studies have found similar trends where disease status was better predicted by VEP compared to OCT and VEP assessed remyelination given its measures on latency and dispersion[112,113]. Nonetheless, similar to OCT, the VEP lacks the ability to evaluate other parts of the visual pathways such as the optic radiation and cortex. This calls for imaging modalities that have the ability to examine both the anterior and posterior afferent pathways, such as MRI.

2.6 MRI Measures of Injury and Repair in ON and MS

MRI is the modality of choice for the diagnosis and monitoring of MS[28,114,115]. The use of MRI in ON varies. Historically, MRI for ON faces some challenges including artifacts from uncontrolled eye movement, the small size of the optic nerve, and signal interference from

surrounding tissues such as fat, bone, and CSF[103,116]. With the development of new MRI pulse sequences and the use of fast imaging technologies, high-quality MR imaging for ON is possible. Clinically, MRI can help make a differential diagnosis of ON and assess for evidence of MS-like lesions or other possible etiologies using sequences covering both the brain and optic nerves[117,118]. Various studies suggest that the risk of developing MS in ON patients who have brain white matter lesions (Fig. 2.4) can be three times greater than those who do not[119], even in AON where there is only mild optic disc edema as determined by OCT[120]. In fact, if there are >1 MS-like lesions in the brain at the time of first ON episode, the risk of subsequent MS over the next 15 years becomes ~70%[39]. In research studies of ON and MS, MRI has shown an increasingly important role. In particular, a variety of MRI methods have demonstrated the potential to measure tissue injury and repair following ON and MS in both focal lesions and the lesion-free areas. MRI methods can be divided into three categories: 1) conventional; 2) advanced, and 3) emerging new MRI and image analysis techniques, as detailed below.

2.6.1 Conventional MRI Methods

2.6.1.1 T1-weighted Imaging

Typically, the generation of MRI signal relies on the properties and amount of protons (hydrogen nuclei of water molecules) in the local environment of a tissue, in addition to the characteristics of the external magnetic field that (B_0) that interacts with the protons[121]. MRI signals of tissues are generally determined by the constant spinning (Larmor frequency, ω_0) of protons in their local environment which have their own magnetic fields, and are randomly oriented outside of strong magnetic fields. Thus, MR signal is generated[122,123]. Applying a radiofrequency (RF) pulse to a tissue in a magnetic field will excite the protons into an unstable status. When an external magnetic field B_0 is applied, a fraction of protons aligns positively or

negatively with the B_0 field generating a net magnetization vector (Mz) (green arrowed). When a RF pulse is applied, protons matching the frequencies (ω) of the RF pulse move to the higher energy orientation relative to B_0 shifting longitudinal (Mz) to transverse magnetization (Mxy). After removal of the RF pulse, protons lose energy shifting towards Mz from Mxy. The time constant that is associated with the time required by the protons to recover 63% of its maximum Mz value is called T1-relaxation time or T1, also referred to as longitudinal or spin-lattice relaxation[124]. To maximize T1 contrast between tissues in T1-weighted MRI, use of both short TE (time of echo) and short TR (repetition time)[125] is preferred. In ON lesions, tissue injury including demyelination, axonal injury, and inflammation can all cause T1 prolongation, and decreased number of protons left to recover their magnetization vector in affected tissue leads to hypointense signal intensity compared to the healthy tissues on T1-weighted MRI[126-128]. However, this change in T1 MRI signal intensity can be misleading as it can be due to the resolution of edema besides tissue repair[129], and the evaluation of signal change is primarily done visually.

Another important use of T1-weighted MRI is the measurement of tissue atrophy. For example, measurement of volume loss in the thalamus with or without ON, which is a key relay structure of the afferent visual pathway, is predictive of cerebral volume fraction in both RRMS and SPMS using high-resolution T1-weighted MRI and OCT. Similarly, there is a strong correlation between thalamic volume and GCL thickness in MS patients[130]. Nonetheless, similar to other conventional imaging, T1-weighted MRI suffers from 1) lack of specificity to lesion pathology[131], 2) only moderate correlation between T1 lesion volume and patient disability, and 3) persistence of lesions even after the acute state of ON[132,133].

Gadolinium is a paramagnetic contrast agent[134] which will shorten T1 and brighten the signal in areas with blood-brain barrier leakage[135,136]. In ON and MS, this sequence identifies acute

lesions suggesting active inflammation[137,138]. In 94% of AON cases, gadolinium-enhanced imaging successfully intensifies lesions, but it is not equally useful in the case of chronic recurrent ON. The detection of acute lesions in the optic nerve with ON can be increased to 96% with increased dosage of gadolinium[139]. The acquisition of gadolinium-enhanced MRI is straightforward. It takes around 5 minutes, typically 3-5 minutes after the collection of the pre-contrast T1-weighted MRI[140], accompanied by fat saturation to distinguish the enhancing areas.

2.6.1.2 T2-Weighted Imaging

The T2-weighted MRI sequence highlights differences in the T2-relaxation time of different tissues[125], which characterizes the transverse or spin-spin relaxation of the net magnetization vector[121]. The time required for 37% of the initial magnetization value to remain after application of RF pulse is called T2-relaxation time or T2-decay. T2-decay can result from the longitudinal relaxation of the T1 and spin-spin interaction of protons. In contrast to T1-weighted MRI, it requires long TR and TE for best acquisition[125]. In T2-weighted MRI, ON and MS lesions appear hyperintense compared to the surrounding tissue[141,142], and this sequence is widely used to identify the number and volume of clinically silent lesions[143,144]. T2 hyperintense lesions may represent any of the tissue changes including edema, inflammation, demyelination, axonal loss, and gliosis, or their combination[131,145]. T2 lesion load is shown to correspond with visual acuity; the more lesion load, the greater the visual dysfunction[4,146]. Conversely, a decrease in lesion volume may indicate repair or neurodegeneration mitigation, while increases suggest neurodegeneration[126,147,148]. In addition, T2-weighted imaging is also used for determining the cross-sectional area of the nerve and the thalamus to assess disease status, as volume decrease due to tissue atrophy following the loss of myelin and axons[71,149]. Limitations of T2-weighted imaging are similar to T1-weighted MRI regarding specificity and sensitivity[148,150], and clinical

correlates[141]. Moreover, the signal generated by the surrounding CSF and fat may be challenging in imaging the optic nerve using T2-weighted MRI, as the signal intensity increases with increase in T2-weighting, creating partial volume artifacts[151,152]. Consequently, several fat suppression sequences such as short tau inversion recovery (STIR) and selective partial inversion recovery (SPIR) have been developed[85,153].

2.6.1.3 STIR Imaging

With the potential of suppressing fat and other surrounding structures, STIR is commonly used in ON imaging. Similar to T2-weighted MRI, STIR uses a long TR and TE, which can efficiently negate the short T1 bearing fat signal[154,155]. Specifically, STIR utilizes a 180-degree RF pulse prior to applying the excitation pulse to invert the net magnetization. A short inversion time is then used so that the lipid signal is approximately zero whilst other tissues continue to give a negative signal. So, when the 90-degree excitation pulse is applied, the magnetization vector in these tissues will be flipped whereas the lipid signal will remain zero[125]. Arguably, STIR is the only method that can be used in a magnetic field with inhomogeneity and in low magnetic fields[156]. However, it requires a relatively long acquisition time due to long TR, and long TE leads to low signal-to-noise ratio (SNR) for which tissue contrast may be affected[125,157].

2.6.1.4 Fluid-attenuated inversion recovery (FLAIR) Imaging

FLAIR imaging is equivalent to T2-weighted MRI with the exception of darkening the free water components, such as CSF[125]. FLAIR is very sensitive to tissue abnormalities and is particularly useful in detecting lesions near the ventricles or CSF in MS and ON[132,141]. To reduce acquisition time and minimize partial volume effects in acquiring high-resolution images, there have been new multiple hybrid sequences developed including the fat-suppressed, fast spin echo (fsFSE) and SPIR, with or without FLAIR[153,157]. This fast T2-weighted inversion recovery

sequence can detect lesions in or near the cerebral cortex in MS patients beyond suppressing the CSF[158]. In a study comparing STIR, SPIR and SPIR-FLAIR in ON patients, SPIR-FLAIR was shown to be the most sensitive in detecting optic nerves abnormalities[159]. Lesion length was also the longest in SPIR-FLAIR, in the absence of the fsFSE sequence in that study. However, as part of the conventional imaging techniques, these sequences are either limited by sensitivity to tissue microstructure or specificity to pathology, highlighting the importance of more advanced MRI.

2.6.2 Advanced MRI Methods

2.6.2.1 Magnetization Transfer imaging (MTI)

Apart from mobile protons, there is another pool of protons in tissues which are bound to macromolecules such as proteins and lipid membranes that are rich in myelin and axons. Selective saturation of these bound protons creates a rapid exchange between them and the free protons, resulting in the transfer of magnetization. The magnitude of this exchanging effect is quantified as the magnetization transfer ratio (MTR)[160], and thus MTR is an indirect measure of macromolecular content[161]. Indeed, abundant evidence has shown that damage to myelin and axonal membranes leads to reduced MTR[162-164]. MTI can assess new, stable and resolved lesions, thus potentially improving our ability to monitor tissue damage and repair[165], including the treatment of myelin repairing and neuroprotective agents[166]. Advantages of MTI include further enhancement of focal changes in the contrast-enhanced T1-weighted and T2-weighted MRI of lesions in ON and MS patients, by suppressing surrounding tissue signal intensities[167]. Moreover, MTI can detect early demyelination or protein destruction earlier then routine MRI sequences[150,168], but it has limited use in a routine clinical setting as the technique is susceptible to motion-related artifacts, and MTR changes with disease stage[169]. Though MTI is widely used in assessing tissue injury and repair, it is not the focus of our research as MTI focuses mainly on myelin changes whereas we wanted to

detect axon and myelin interplay and region-wise structural changes more evident in NODDI and texture measures.

2.6.2.2 DTI

Diffusion-weighted imaging (DWI) is a sensitive method for detecting microstructural changes, particularly those in white matter tracts. DWI works based on the principle of the random movement of water molecules[30]. Changes in the diffusion pattern of water molecules compared to healthy tissue can signify disruption of the blood-brain barrier and suggests alterations in tissue microarchitecture[170,171]. Traditional DWI requires a minimum of three gradient directions to acquire, but it lacks the ability to reveal the directionality of diffusion. DTI resolves this issue by applying at least six gradient directions that allow the formation of a 3-D tensor matrix at each voxel[172,173]. In white matter tracts such as the optic nerve, nerve fibers are highly packed[174], resulting in greater diffusion along the long axis of the tracts and limited diffusion in the perpendicular direction. This restriction to diffusion is disturbed when there is a pathological process like demyelination, causing increased diffusivity and disruption of the directional selectivity (anisotropy) of diffusion along the fibers[30]. Several metrics from DTI have shown promise in detecting de- and remyelination and axonal injury, including fractional anisotropy (FA), axial diffusivity (AD), and radial diffusivity (RD). FA evaluates the amount of directionality in which water is being restricted on a zero to 1 scale[175]. DWI detects microstructural damage that is not visible with conventional techniques (Fig. 2.4). This imaging technique is used for a better understanding of ON pathophysiology due to sensitivity to fiber architecture[176]. FA, AD, and RD of the affected optic nerve correlates with OCT and VEP measures of RNFL thinning and multifocal VEP amplitude in ON patients, indicative of axonal integrity disruption, and correlates well with clinical outcomes[177-180]. FA predicts alterations in the optic radiation, and differentiates

healthy optic nerve from both affected and contralateral optic nerve in ON patients with MS[181]. DTI detects white matter microstructural alterations not only in lesion areas in MS patients but also in the surrounding normal-appearing white matter, suggesting decreased axonal density[173,181]. Limitations of DTI include poor correspondence of the diffusion-weighted signals to fiber arrangement that don't fit a Gaussian distribution, such as crossing fibers[182-184]. Consequently, multi-shell diffusion techniques have been developed, including NODDI (Fig. 2.5), and composite hindered and restricted model of diffusion (CHARMED), both of which use multi-compartment HARDI and can generate reliable surrogate markers of microstructural white matter abnormalities[185,186]. Other advanced DWI techniques such as diffusion kurtosis imaging uses alterations in the normative pattern in diffusion, diffusion spectrum imaging uses diffusion spectra to enable the resolution of intervoxel heterogeneity of diffusion, and Q-ball imaging uses spherical deconvolution and measures intervoxel fiber orientation and have also been used recently in a few MS studies[181,187-189]. All of the above-mentioned DWI techniques can prove beneficial for evaluating microstructural changes in ON and patients.

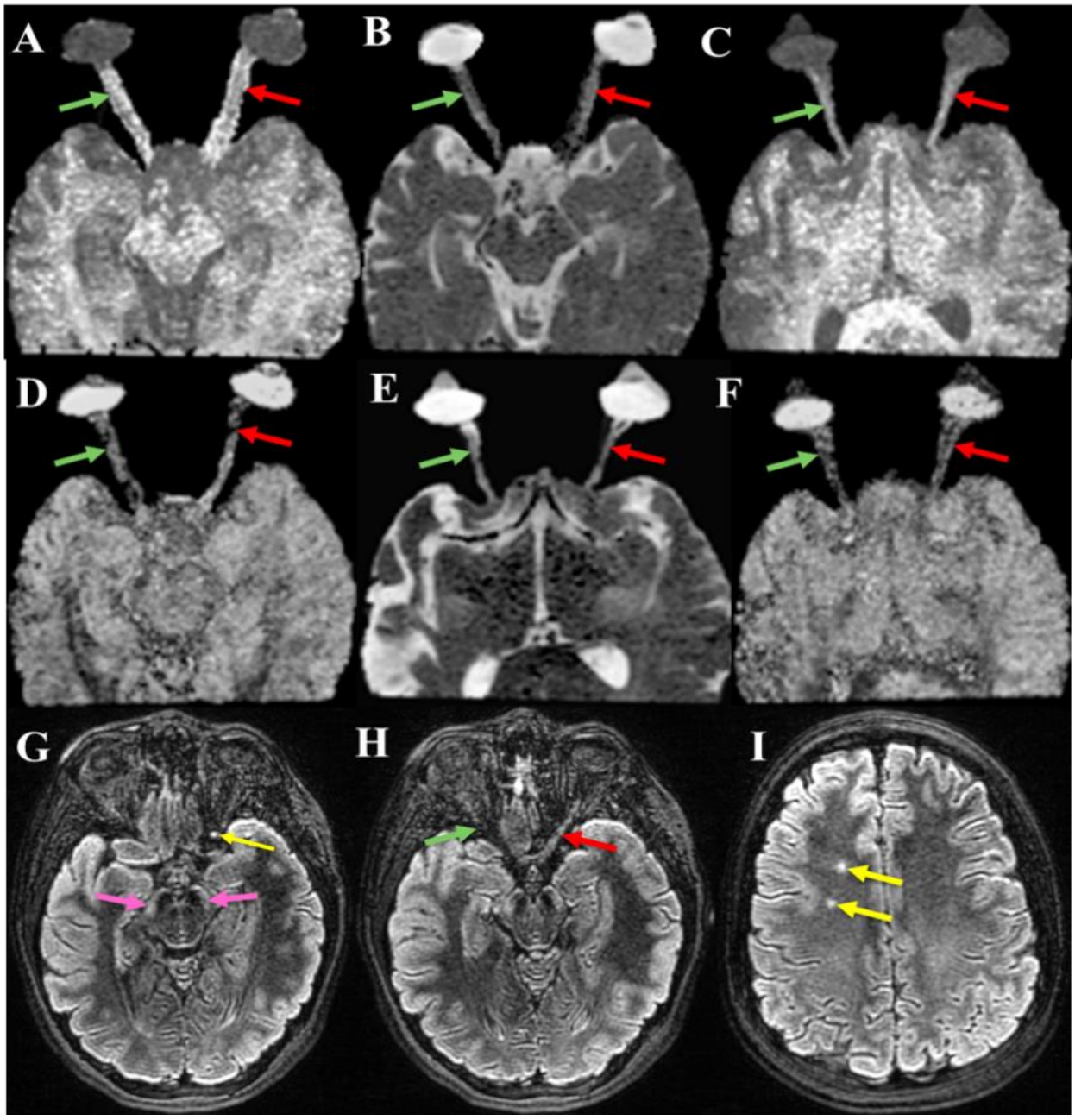

Fig. 2.4: Changes in ON patient MRI. Example DWI images of (A) FA, (B) MD, and (C) ODI maps at baseline showing decreased FA, increased MD, and increased ODI in affected optic nerve (red arrowed) compared to contralateral optic nerve (green arrowed) indicating tissue injury. (D) FA, (E) MD, and (F) ODI maps of the same patient at 12 months MRI show similar signal intensity

on affected and contralateral optic nerve indicating repair. Axial DIR images showed hyperintensities of (G) active lesion (yellow arrowed) on affected optic nerve and optic tracts (purple arrowed), (H) affected versus contralateral optic nerve, and (I) active lesions at brain WM suggesting neurodegeneration.

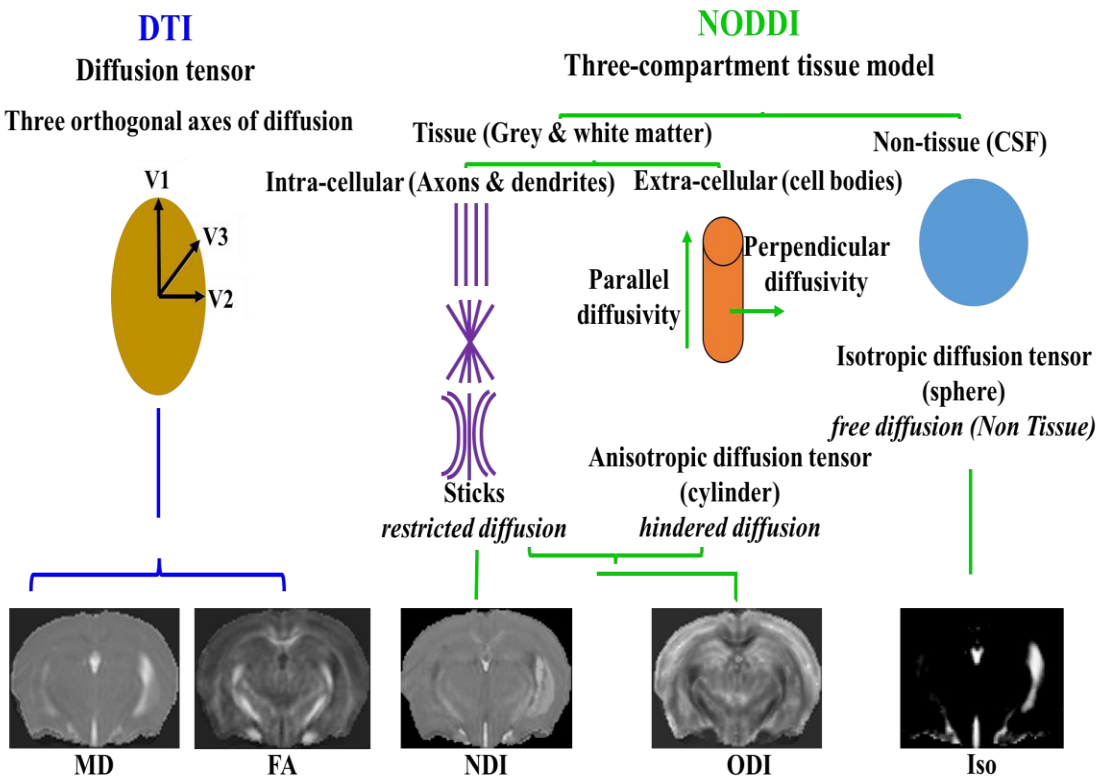

Fig. 2.5: NODDI and DTI principles. A diagram showing principles of diffusion tensor (DTI) and advanced multi-compartment model (NODDI) showing a Gaussian distribution problem in DTI and compartmentalization of different tissue signals in NODDI to overcome the issue (image was adapted from Barritt A. W. et. al.[190] and Tariq M. *et al.*[191]).

2.6.2.3 Functional MRI (fMRI)

fMRI allows mapping of neural activity by assessing the metabolic activity of brain cells based on blood oxygen level dependent (BOLD) contrast[192]. The BOLD signal changes with the performance of different tasks that activate different brain areas of a subject during imaging. Monitoring changes in the visual cortex following eye stimuli appears to be an indirect means of assessing tissue injury and repair in the afferent visual pathway[193,194]. Reduced activation of visual cortex has been reported in patients with either acute or previous ON, relative to controls, possibly representing reduced neuronal input following pathological changes in the optic nerve such as edema, inflammation, demyelination and axonal loss[195]. Conversely, decrease in BOLD signal in ON patients compared to controls correlated with both reduced Snellen's visual acuity score and increased angles in visual field defects in Arden contrast sensitivity measurements [196]. There is also increasing evidence for compensatory brain plasticity after the onset of ON, likely indicating repair in the visual pathway, although the location, timing and role of the contralateral optic nerve are still to be elucidated. Moreover, this detection can be technically challenging as it often relies on minimal changes of a low SNR signal[197]. In addition, outcomes of fMRI may be influenced by task performance, particularly in ON and MS patients, most of whom present with some form of disability[198]. As our aim one focused on cuprizone preclinical model of MS which does not induce visible functional disability, fMRI was not the focus of our research.

2.6.2.4 Magnetic Resonance Spectroscopy (^{1}H-MRS)

^{1}H-MRS is a non-invasive tool to measure the concentration of metabolites in the CNS, and is mainly performed for indirect evaluation of the visual system. Metabolites include N-acetyl aspartate (NAA), Choline (Cho), Inositol (Ino), Lactate (Lac), Creatinine (Cr), and lipids[199,200]. Changes in NAA in ON or MS, in particular, may provide visual pathway-specific

neurodegenerative information[201,202]. For an example, the RNFL thickness in ON has shown a significant correlation with visual cortex NAA concentrations but not with normal-appearing white matter NAA, whereas multiple ^{1}H-MRS studies in MS patients have shown decreased metabolite concentrations in the normal-appearing white matter compared to healthy tissue[50,203-205]. NAA concentrations in the visual cortex are also lower in patients with previous ON than patients with AON[204]. NAA concentrations in the optic chiasm, a major component in the anterior visual pathway, was lower in ON patients compared to the healthy optic chiasm[206]. These findings suggest a potential benefit of ^{1}H-MRS in illustrating the relationship between injury from the anterior and posterior visual pathways[203]. Disadvantages of ^{1}H-MRS include poor spatial resolution, low reproducibility, and unclear accuracy in some cases, and thus it is mainly used as a research tool[204].

2.7 Emerging MR Imaging and Analysis Techniques

In addition to the conventional and advanced imaging methods mentioned above, there are multiple potentially new approaches that may help improve the measurement of injury and repair associated with ON or MS. This includes both new acquisition-driven MRI technologies and methods based on image postprocessing.

2.7.1 A New MRI Acquisition-driven Method: NODDI

NODDI is a relatively new DWI modality, free from some inherent limitations of DTI by using a three-compartment model of diffusion, namely intracellular restricted diffusion inside nerve fibers, extracellular hindered diffusion in between nerve fibers, and fast isotropic diffusion in the free CSF[185]. DTI measures crossing fibers in the CNS using a Gaussian diffusion model. These measurements naïvely estimate nerve fiber bundle diffusion without considering the presence of axonal membranes and myelin sheaths[207,208]. Higher-order diffusion modelling used

by NODDI produces less equivocal metrics than DTI for characterizing microstructural changes. It produces complementary axonal density maps and the derived findings match electron microscopy fiber density values in both mouse and human brains and spinal cords[44,209]. NODDI has been used in several human and animal models of MS[44,181,209-214]. NODDI can assess axonal degenerative changes in lesional, perilesional, and normal-appearing white matter in MS patents[181]. Orientation dispersion and fiber orientation changes in both lesion areas and normal-appearing white matter have been observed using NODDI in MS patients[209,212]. NODDI generated neurite dispersion results indicative of demyelination in MS spinal cord explicitly match with histological findings[44]. Axonal neurite microstructure in the cervical spinal cord of MS patients shows decreased neurite density and increased dispersion in lesion areas compared to the surrounding global white matter and correlates with clinical outcomes[214]. Identification of cortical lesions along with microstructural myelin, axonal integrity disruption in MS patients indicative of gray matter pathology has been detected by NODDI. Moreover, one of its metrics orientation dispersion index (ODI), shows moderate correlation with clinical outcomes[213]. NODDI thus has potential in ON and MS, to further understand microstructural changes underlying tissue injury in the visual system and brain[215].

2.7.2 Image Postprocessing Methods

Image postprocessing methods, such as MRI texture heterogeneity, could also be used in MS and ON studies as it can foresee the extent of recovery of vision in AON[216]. Image postprocessing comprises of different analysis methods that allow for extracting additional, valuable information from the acquired images. Unique features of tissue are associated with specific distributions of image pixels, also known as image texture[217,218]. Advanced texture analysis methods have shown promise to evaluate myelin and axonal integrity. Texture can be measured through quantifying the

distribution of image pixels or frequency content of an image[217,218]. Texture features from MRI have detected neuroaxonal changes in brains and spinal cords of MS patients and have reported detection of remyelination in an animal model of MS[219-221]. Texture analysis of MRI correlates with tissue pathology underlying MS, using routine clinical MRI in lesions, normal-appearing white matter, and in healthy tissues[222,223]. Therefore, texture analysis is a potential candidate for evaluation of pathological processes underlying disease progression in MS. Angular entropy, another texture measure, is derived from the raw power spectrum of spectral domain information from an image through FT as an inverse measure of axon alignment. Texture angular entropy distinguishes controls, RRMS, and secondary progressive MS (SPMS) cohorts successfully[223].Texture features detect neurodegenerative changes in MS brains and spinal cord and significantly correlate with disability[219,220]. Texture analysis not only detects tissue injury, but repair such as remyelination as demonstrated in a study of an animal of MS[221]. One promising technique for characterizing image texture is the FT, which evaluates the integrity of a tissue structure through quantifying the frequency content of an image. Specifically, the power spectrum of the FT has shown the ability to detect demyelination and axonal injury in MS through analysis of the alignment of a tissue using angular entropy[224]. This may suggest the potential of such image postprocessing techniques for measuring injury and repair in ON and MS. However, the specificity of these methods is subject to further confirmation. Moreover, using a multi-scale, localized version of the FT, other researchers have also found that the texture heterogeneity of T2-weighted MRI of the optic nerve predicts visual function following AON[216,225].

2.8 Structure Tensor Analysis

Structure tensor analysis is a promising image post-processing technique that has recently been used to evaluate tissue injury and repair in demyelinated lesions in MS[226]. Structure tensor

analysis relies on variations in pixel intensities in tissue to estimate the structural properties such as tissue directionality, organization, and distribution[217,227]. Roughly speaking, it is also a type of texture analysis method. Structure tensor measures the 2-dimensional tensor matrix f (x, y) of an image in x and y directions and calculates different organizational properties of tissue by determining its dominant and minimal directions[228]. Structure tensor quantifies the predominant directions of gradients in a specified tissue and measures structural organization as coherency, dispersion of nerve fibers as energy, and local distribution differences between nerve fibers as orientation (Fig. 2.6)[228]. Budde *et al.*[229] quantified the orientation of brain microstructure in the CNS using structure tensor analysis of histology samples to validate their DTI findings and showed a strong positive correlation between these two measures. Circular variance as a substrate of orientation of axonal nerve fibers (Fig. 2.6) has recently been used to validate NDI in MS spinal cord and can be a potential biomarker of neurite dispersion[44], but needs further validation in other tissues such as the white and gray matter.

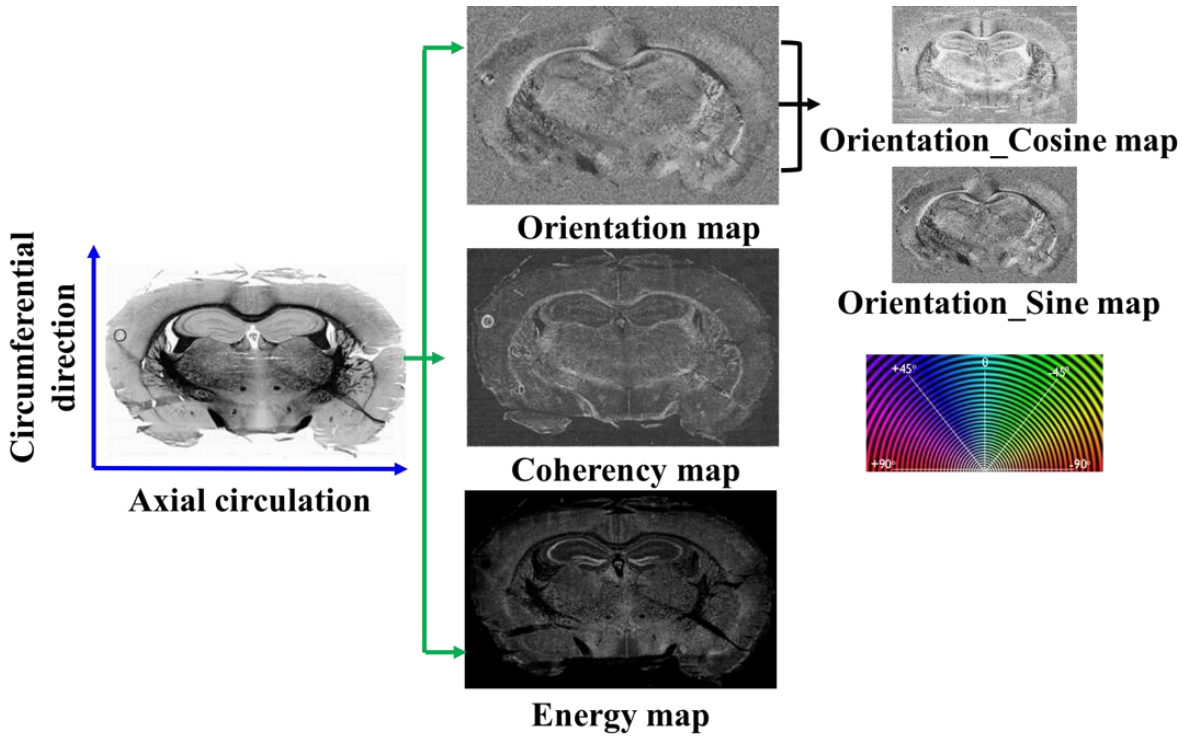

Fig. 2.6: Structure tensor analysis outcomes. Structure tensor analysis showing outputs such as orientation, coherency, and energy maps generated from different tissue directional properties. Circular variance, a measure of angular variability is measured from orientation maps in all the directions from +90° to -90° (image is adapted from Rezakhaniha R. *et al.*[228]).

Although there is a strong association between ON and MS, not all patients with ON develop MS[39,230]. In addition, histological validation of advanced non-invasive MRI measures in MS is also warranted to detect de- and remyelination specific metrics. Region-wise timing and prevalence of pathological processes such as de- and remyelination and their association with axonal pathology is scarce in MS research, using both advanced MRI and histology measures. Evaluation of advanced NODDI metrics in detecting additional microstructural changes in ON has

also not been attempted. These techniques are thus the focus of my thesis, and I used two well defined models of MS to identify and discover new imaging measures for assessing and understanding tissue injury and repair in demyelinating diseases for future development of new neuroprotective and reparative agents for MS patients.

CHAPTER 3

Investigating the value of advanced MRI in understanding the changes in MS-like pathology using a cuprizone mouse model

3.1 Introduction

Myelin and axonal changes are critical pathological manifestations in MS; however, the exact evolution of these pathological processes are unclear. Specifically, when and how myelin and axons repair after a demyelinating insult, and whether that presents in a specific region is difficult to determine in vivo, especially given the heterogeneity of MS pathology both within and between patients. Moreover, the density and diameter of axons vary widely between anatomical locations, even within the same neurological structure. Thick axons are wrapped with thick myelin sheath and seem to be more susceptible to pathological injury than thin axons according to prior studies[231]. Therefore, understanding the timing, injury and repair pattern of myelin and axons has critical implications for both disease monitoring and treatment.

Animal models serve as promising tools to understand disease mechanisms and validate in vivo measures. One such candidate is the cuprizone model. It is a toxicant-induced model of MS achieved through continued feeding of copper chelator cuprizone (bis-cyclohexanone-oxaldihydrazone) causing accelerated demyelination circumventing the autoimmune factor of the disease. This model features primarily demyelination initially through direct killing of mature oligodendrocytes, with minimal inflammation[35-37] and has widely been used for studying myelin and axonal changes similar to that occurring in pattern III MS lesion pathology[25]. The corpus callosum is a majorly target area in this model, as in MS, where more than 90% of the patients[60] show lesions in this structure[232]. Multiple studies show that the axonal diameter is small but density

is high in the genu of the corpus callosum whereas the body and splenium contain mainly large caliber axons with less density[233-235] making corpus callosum a favorable anatomical location in MS to study region-wise pathology[25,236-239]. The anatomical preference for such pathological changes in the corpus callosum is not well understood. Moreover, in spite of achieving highly reproducible pathology following cuprizone toxicity in most male mice, the degree of demyelination varies amongst animals (male mice are more susceptible to cuprizone damage than females[63,240]).

Several advanced MRI methods have shown the potential for assessing myelin and axonal properties in vivo, including diffusion-based techniques. DTI has the advantage of providing potential insight into the microstructural changes underlying tissues pathophysiology and has been widely used in both MS and its animal models[237,238,241,242]. DTI parameters such as AD, RD, and FA have shown correlations with axonal damage, myelin integrity, and overall injury, respectively in multiple MS studies[42,237,238]. But several studies have concluded that DTI metrics are sensitive but not necessarily specific to myelin and axonal changes, confounded by the impact of the co-localizing inflammation and the inherent limitations of poor fitting of diffusion signal in the presence of crossing fibers[182-184]. The new HARDI-based sequences such as NODDI may be of increased promise. NODDI outcomes like neurite density index (NDI) can inform about density of neurites and ODI about neurite (axonal) integrity. Axons and dendrites are together known as neurites[243] but some suggest NDI may be sensitive to myelin integrity along with neurites[44,244] making it a potential marker for myelin pathology. The complexity of the orientations and density of neurites is specific to axonal pathology[44] and has been used in several studies to detect microstructural changes underlying MS[44,185,210,213]. However, further histological validation is required to confirm their utility.

Advanced texture analysis methods have also shown the promise in evaluating myelin and axonal integrity in various diseases including MS. Texture refers to the distribution of image pixels[217,218]. Angular entropy is a relatively new texture measure, which is derived from the power spectrum of the FT and acts as a measure of tissue alignment, including that associated with myelin and axons[224,245]. Angular entropy detected the differences in tissue alignment of the corpus callosum between RRMS, and SPMS, and control cohorts successfully[223]. Structure tensor analysis is another novel texture analysis method. Structure tensor refers to the predominant directions of gradients in a specified tissue, and therefore this method focuses on the detection of alignment organizations of a tissue. Primary outcomes of structure tensor analysis include: coherency (directionality of nerve fibers and similar to anisotropy), energy (dispersion of nerve fibers), and orientation distribution[228]. Structure tensor analysis has shown success in validating DTI outcomes previously[229] and the ability to detect changes in myelin and axonal integrity and quantify subtle pathological changes in a lysolecithin model of MS following de- and remyelination in MRI and histology[210]. Alternatively, circular variance as a measure of dispersion of axonal nerve fibers has recently been used to validate NDI in MS spinal cord[44] histologically but this metric needs further validation for its ability to detect changes in other tissues such as brain.

In this study, we investigated the feasibility of using NODDI and novel texture analysis methods in comparison with DTI for assessing the time course and regional preference of myelin and axonal changes using a cuprizone model of MS. Specifically, we characterized: a) MRI diffusion and angular entropy changes in the corpus callosum of mouse brain 6 weeks on and 8 weeks off of cuprizone feeding; b) how these changes compare between the genu, body, and splenium of the corpus callosum; and 3) how MRI changes compare with quantitative histological

outcomes. Angular entropy calculations used T2-weighted MR images. Histological measures included circular variance and those from structure tensor analysis.

3.2 Materials and Methods

3.2.1 Animal Model

Twenty-nine 8-week-old male C57BL/6 mice (Charles River Laboratories, Quebec, Canada) were examined. All animals were allowed one week to adapt to their new environment prior to the experiment. All procedures conducted were in accordance with the guidelines of the Canadian Council on Animal Care and the University of Calgary Animal Care Committee. As one of the effective protocols[34,246] for induction of demyelination, 27 mice were fed *ad libitum* diet of 0.2% cuprizone (Sigma-Aldrich, Ontario, Canada) mixed with crushed up standard rodent chow for 6 weeks to induce progressive demyelination. All cuprizone mixed chow were stored in a vacuum sealed container at 4°C. Food was changed every alternate day, and food and water intake were monitored daily. The diet was changed to normal rodent chow pellets for an additional 8 weeks after 6 weeks cuprizone feeding, to investigate spontaneous remyelination repair. The remaining 2 mice were fed normal chow for 12 weeks and kept as controls.

3.2.2 MRI Protocol

All animals were scanned with a 9.4T ultra-high field MRI scanner (Bruker BioSpin GmbH, Ettlingen, Germany) using a 35-mm ^{1}H transmit-receive volume coil. The mice were stabilized under 4% isoflurane for induction and 2.5% for maintenance of anesthesia throughout the scan. Prior reports focused mainly on the remyelination course in this model, and so assessments were performed at 2 and 5 weeks, or 3 and 6 weeks after the cessation of cuprizone feeding[25,34]. To obtain comprehensive understanding of both de- and remyelination, we imaged the animals over an extended time course at 7 sequential time points: at week 2 on cuprizone diet to evaluate

initiation of demyelination, week 4 for progression of demyelination, week 6 for peak demyelination, and then at week 1, week 3, week 6, and week 8 after removal of cuprizone from the diet to detect spontaneous, progressive remyelination. MRI for one animal after week 3 could not be completed due to severe respiratory distress, likely resulting from anesthetic complications. After imaging session at each time point, 3-7 mice were sacrificed immediately for histological correspondence except for week 4 on cuprizone diet due to scheduling issues. Five mice were imaged throughout the 7 time points to observe true sequential changes in tissue pathology, and so were only sacrificed at the end of the experiment (longitudinal cohort). Two control mice fed a normal diet were also imaged at two time points; 2 weeks on and 6 weeks after cuprizone diet corresponding to the expected de- and remyelination time points of the cuprizone-fed mice. See Table 3.1 and Fig. 3.1 for experimental details and mice availability per time point.

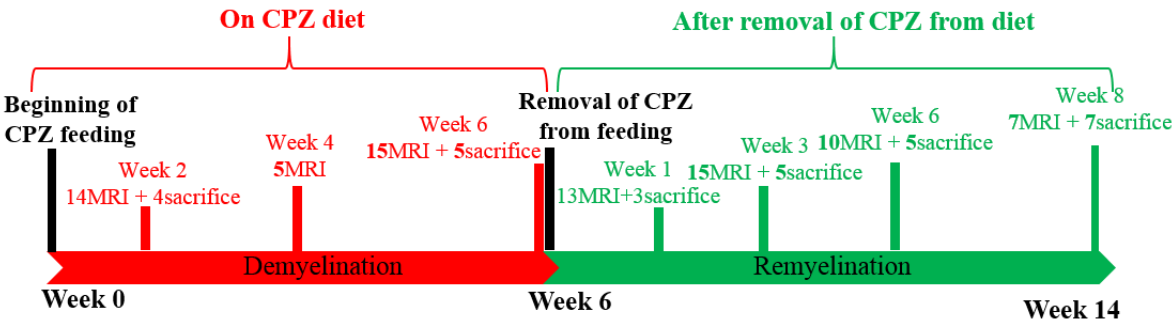

Fig. 3.1: Experimental plan. Experimental time points for toxicant-induced cuprizone mouse model of MS with the number of mice involved in MRI and histology to assess de- and remyelination.

Table 3.1: Experimental time points and number of animals involved at each time point including the control animals: number of MRI, number of perfusions, number of animals used in histology, and number of animals used in TEM. Abbreviations: CPZ=Cuprizone; MRI=Magnetic Resonance Imaging; C=Control; TEM= Transmission Electron Microscopy.

Experimental time points	No. of mice MRI scans	No. of mice Sacrificed	No. of mice for histology	No. of mice for TEM
Wk2 on CPZ	14 (2C)	04 (1C)	04 (1C)	-
Wk4 on CPZ	05	-	-	-
Wk6 on CPZ	15	05	05	-
1Wk after CPZ	12 (1C)	03	03	-
3Wk after CPZ	15	05	05	-
6Wk after CPZ	10 (1C)	05 (1C)	02	03 (1C)
8Wk after CPZ	07	07	04	03
Total	78 (4C)	29 (2C)	23 (1C)	06 (1C)

Imaging sequences consisted of a 2D anatomical high-resolution rapid imaging with refocused echoes (RARE) T2-weighted MRI for lesion confirmation as well as texture analysis, and a multi-shell HARDI sequence acquired using 2D echo-planar imaging for NODDI and DTI assessment. Imaging parameters for T2-weighted images were: echo time (TE)/ repetition time (TR)=48/4000 ms, slice thickness=0.5 mm, matrix size=256×256, field of view (FOV)=1.28×1.28 cm^2, acceleration factor=4, number of slices=18. The 2-shell HARDI parameters were: b-value = 1000 and 2000 s/mm^2, with 15 and 30 diffusion weighting directions, 5 b0 volumes/unweighted scans, TE/TR=30/5000 ms, slice thickness=0.5 mm, metric size=128×128, FOV=1.28×1.28 cm^2,

pixel size=100 μm^2, and number of slices=18. Total acquisition time was approximately 90 minutes.

3.2.3 MRI Processing

MRI images first underwent several pre-processing steps. Initially, the raw MR images were converted into a NIfTI-1 format using ImageJ (NIH, Bethesda, MD, U.S.) for use in the subsequent image processing pipeline. Then, manual skull-stripping was performed for both the T2 and diffusion images to enhance image quality, reliability, and reduce computation time. Manual skull-stripping was done due to the inability of the available software such as FSL (FMRIB Software Library, Oxford, UK) for processing mouse images. Next, the metadata file from the Bruker source protocols was used to extract the required information for calculating diffusion metrics, diffusion weighting and gradient directions (bval and bvec), using DSI-Studio (Yeh, Fiber Tractography Lab, Pittsburgh, U.S.). Diffusion data were further pre-processed using FSL and DSI-Studio for correcting potential eddy current-induced distortions and subject motion.

Conventional DTI data analysis was performed with FSL using only the b=1000s/mm^2 shell. Both FA & mean diffusivity (MD), two of the commonest maps were obtained. Only the low b-value data were considered for DTI due to ill-fitting of b-value data above 1500s/mm^2 with the DTI model[247]. Concatenated diffusion data from both shells were used to generate NODDI parameters using an open-source NODDI toolbox (UCL, England) in Matlab (Mathworks, Natick, MA, U.S.). Two of the most commonly used metrics, NDI and ODI, were calculated. To ensure comparability across outcomes both within and between time points, we performed the following enhancing procedures. Diffusion parametric maps generated from DTI and NODDI were co-registered to the T2-weighted images at the same time point to ensure the maximum comparability between all imaging outcomes. The longitudinal diffusion maps were subsequently co-registered

to their first available time point T2, after over-time co-registration of the T2 images to ensure position alignment between time points. All the aforementioned image co-registration procedures were done using the FLIRT linear registration tool of FSL. FLIRT works by transforming images of different datasets in different planes into one coordinate system to achieve spatial alignment without significant data loss[248]. Specific settings used at the co-registration steps were: rigid body transformation with 6 degrees of freedom; correlation ratio as a cost function for inter-modal and normalized correlation for intra-modal registration; and Hanning window sinc interpolation (Fig. 3.2).

Image texture analysis was done using a reported method built in-house[223]. Prior to quantification, histogram standardization was done for the T2-weighted images after skull-stripping to reduce potential intensity variations between scans across time points and to match tissue spatial information[249] using a standardized procedure built in Matlab. Angular entropy calculation was based on the FT power spectrum using a method implemented with Eclipse (Eclipse Foundation, IDE Inc., Canada). Briefly, this method computes 1) the total content of the frequencies of a selected image area with different aligning directions by identifying the dominant aligning angle of the nerve fibers; 2) the corresponding power spectra of dominant alignment of frequency information in a polar coordinate system according to the tissue organization and pattern; 3) the distribution of frequencies based on the anatomical trajectories of the nerve fibers by angle (-90 to +90)°[250]. This provided a spectrum of alignment strength for each potential aligning directions of a tissue. As previously tested using the corpus callosum at human brain in both healthy and MS subjects, tissues with highly aligned white matter tracts show higher anisotropy than those with low alignment as expected in MS or its models[223].

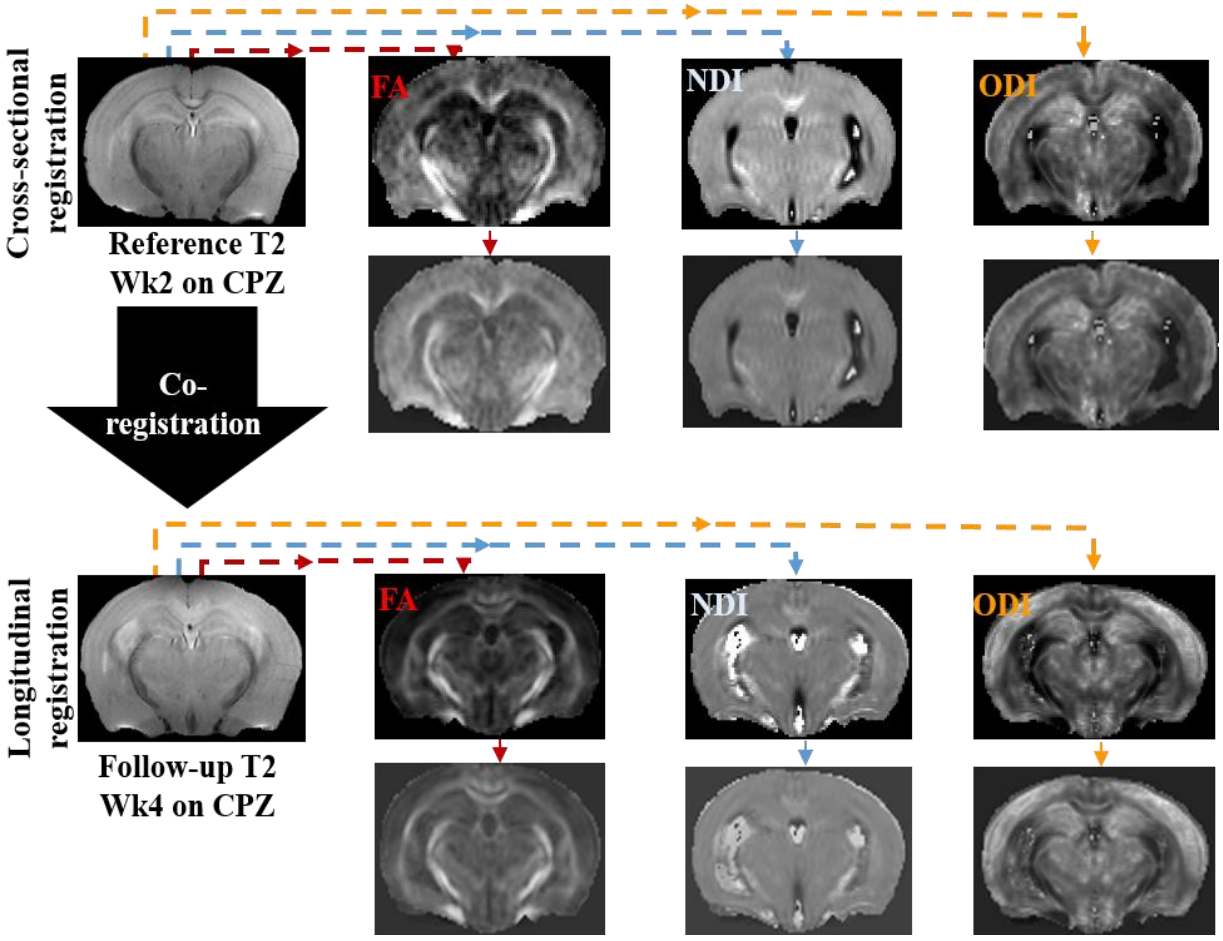

Fig. 3.2: Image registration steps. Example image registration between different MRI outcomes in the same CPZ mice. Cross-sectional image registration was done using high-resolution T2-weighted images of that experimental time point as the reference image for spatial alignment of diffusion outcomes. Longitudinal registration included co-registration of the cross-sectionally registered diffusion metrics to the first available experimental time point T2-weighted image of the same animal.

3.2.4 MRI Analysis

Outcome analysis focused on the corpus callosum, the largest interhemispheric white matter brain structure wherein the fiber tracts are highly organized and is easily identifiable on MRI[25]. Regions of interest (ROIs) were drawn within the corpus callosum over the genu, body, and splenium. ROIs used in DTI and NODDI metrics were drawn initially over the T2-weighted images with reference to the corresponding location to the histology. To ensure ROI confidence and to identify the distinct anatomical regions of the corpus callosum, the Allen Mouse Brain Atlas (Allen Institute for Brain Sciences, U.S.A.) and the Waxholm Space Atlas of the C57BL/6 Mouse Brain (Duke University Medical Center for in Vivo Microscopy, U.S.A.) were used. Slice numbers 9, 14, and 15 out of 18 showed the best representations of the splenium, body, and genu (Fig. 3.3) on MRI respectively, so these 3 slices were analyzed to quantify diffusion indices at the corresponding regions from DTI and NODDI. The averaged values were used for group analysis. To minimize cross-image variability, all the diffusion indices were normalized according to the following formula:

$$\text{Normalized value} = \frac{(\text{ROI generated corpus callosum value} - \text{intraslice 3rd ventricle value})}{\text{Intraslice 3rd ventricle value}}$$

The 3rd ventricle was used as it is a region of the mouse brain in this model where no pathology-associated changes are expected. The texture measurement was performed in slice number 17 of the T2-weighted images where the corpus callosum presents as a blob over the genu, and was the only MRI slice sufficient to draw a reasonably sized ROI (6×6 pixels or more) to allow enough tissue structural content for calculating angular entropy[223].

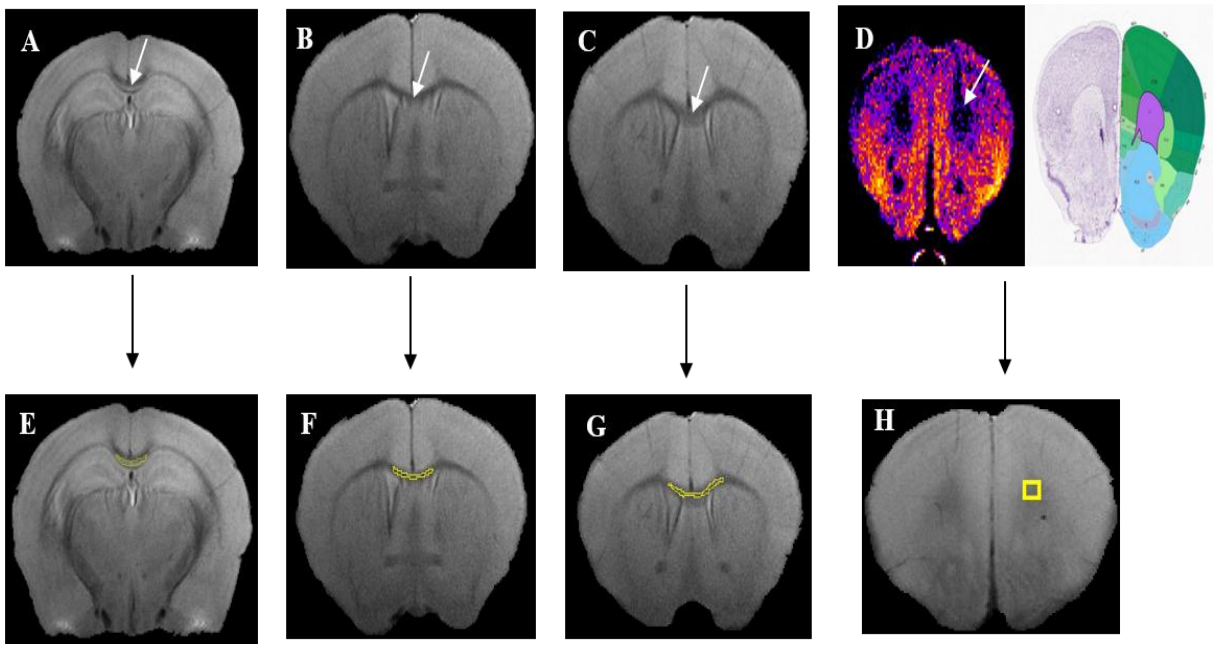

Fig. 3.3: ROI selection over corpus callosum. Example ROIs in cuprizone animal model for quantifying MRI outcomes. Corpus callosum (white arrowed) at (A) slice 9 representing splenium, (B) slice 14 representing body, and (C) slice 15 representing genu were identified to validate ROIs. (D) Corpus callosum is seen as a blob (arrowed) and was used for texture analysis. ROIs were then drawn over corpus callosum at (E) slice 9, (F) slice 14, (G) slice 15, and (H) slice 17 to assess MRI outcomes.

3.2.5 Histological Preparation

A total of 3 - 7 mice were sacrificed immediately after each imaging time point through transcardial perfusion. Specifically, the mice were perfused with 4% paraformaldehyde (PFA) for primary fixation of tissues under anesthesia using 0.625 μl/gm of ketamine+xylazine injected intraperitoneally. Mice brains were then harvested, post-fixed in 4% PFA at 4°C overnight, cryoprotected with 30% sucrose at 4°C for 3 days, embedded in optimal cutting temperature

compound (Fisher Scientific, EDM, Canada), and rapidly frozen in dry-ice cooled 2-Methylbutane prior to preserving the samples finally in an -80°C freezer for histology. 20-μm coronal sections were cut on a cryostat, 3 sections per slide, region matched with MRI, and stored at -20°C freezer prior to staining.

Fixed, frozen brain sections were stained for myelin with EC (Sigma-Aldrich Canada Co., ON, Canada) resulting in light blue appearance of myelinated brain regions and counterstained with 1% Neutral Red (Avantor, EDM, Canada) for cell nuclei visualization[251]. Oil Red O (ORO) (Sigma-Aldrich Canada Co., ON, Canada) staining was done on brain samples to visualize myelin debris to evaluate the degree of demyelination[25]. To detect signals against myelin, a rat monoclonal antibody to MBP (Abcam, MA, U.S.) was used. To visualize healthy phosphorylated axons, rabbit polyclonal antibody to Neurofilament heavy (NF-H) (ENCORBIO, FL, U.S.) was used. MBP (1:100) and NF-H (1:500) used as primary antibodies were diluted with an antibody dilution buffer and incubated overnight to stain for myelin and phosphorylated axons. Corresponding secondary antibodies Alexa Fleur 488-conjugated donkey anti-rat IgG and Alexa Fleur 594-conjugated donkey anti-rabbit IgG (Jackson Immuno Research, PA, U.S.) to MBP and NF-H in 1:400 dilutions were mixed with nuclear yellow (Abcam, MA, U.S.) in 1:800 dilutions for 1 hour in dark room at room temperature after adding secondary antibodies[68].

For TEM, transcardial perfusion was done using a cocktail of ice-cold 2.5% glutaraldehyde (EMS, PA, U.S.) and 4% PFA. The brains were post-fixed in a fixative containing 2.5% glutaraldehyde and 2% PFA for 1 hour. A 1-mm^3 thick section from midline splenium of the corpus callosum was segmented for TEM analysis after further fixation of the tissue in 2.5% glutaraldehyde + 4% PFA in 4°C overnight. Finally, brain sections were post-fixed in 1% osmium tetroxide (OsO_4) in 0.1M cacodylate buffer.

3.2.6 Histological Analysis

Brain sections were digitized using an Olympus VS120 virtual slide scanner for further evaluation. Based on anatomical location and similarity, histological images were matched to the MRI slices and the same number of histology slices were analyzed per animal to the MRI slices.

Quantitative assessment was performed using structure tensor analysis (OrientationJ, Biomedical Image Group, Switzerland) implemented as an ImageJ plugin. The EC and ORO color images were downsized and histogram equalized prior to quantitative analysis. generating coherency, orientation, and energy maps[228]. Downsizing was done to achieve relatively high-resolution parametric maps[226] while maintaining reasonably low computation time. To balance the two, an image size of 7168×4579 was chosen. Histogram equalization was done to reduce staining intensity inhomogeneity using a standardized procedure (saturation threshold of 0.3%) for all the RGB images[252]. The downsized color images were split into 3 gray-scale image channels (red, green, and blue) and then, the gray-scale image with the highest contrast (red for EC and green for ORO staining) was chosen to generate structure tensor maps[253]. Immunostained images only underwent downsizing and histogram equalization as they were generated as 16-bit mono-color images by default. The ROIs were drawn manually over the corpus callosum complementing the ROIs used in the MRI, and their values were averaged for statistical analysis. For analyzing orientation maps, directional statistics were used from circular variance to observe predominant orientational changes over time.

Further evaluation of myelin and axons was performed through TEM image analysis, done at week 6 and week 8 after removal of cuprizone from the diet. A total of 5 cuprizone fed mice and 1 control mouse was used for TEM image analysis. The post-fixed 1 mm^3 sampled tissue sections mentioned above were dehydrated in ascending concentration of alcohol series and

embedded in epoxy resin prior to TEM image collection and analysis prior to semi-thin sectioning (2 μm) of the tissues using a microtome. Cut section of tissues were then lightly stained with Toluidine Blue and visualized under a light microscope (Olympus BX43) to detect desired anatomical location of the corpus callosum. Ultrathin sections (500 nm) of midline splenium were prepared thereafter. TEM images were captured on an electron microscope (Hitachi H-7650, 120 kV, Japan) and analyzed using ImageJ for g-ratio calculation. This was done at 2 time points over the remyelination period focusing on the splenium of corpus callosum where large caliber axons are expected to optimize calculation accuracy. The g-ratio is a unique measure of myelination status of axons calculated as the ratio between the axonal diameter and myelinated axonal diameter: $\mathrm{g-ratio} = \frac{\text{Axon Diameter}}{\text{(Myelin+Axon) Diameter}}$. Lower g-ratio indicates greater myelin thickness. Remyelinated axons show relatively higher g-ratio suggesting thinner, immature myelin[254].

3.2.7 Statistical Analysis

Data analysis used averaged ROI values from the whole corpus callosum or from different locations: genu, body, or splenium. All results were expressed as mean ± standard error (SE). The corpus callosum as a whole provided an overall trend and the sub-regions for location-specific analysis. Over time differences in MRI parameters were determined using the non-parametric Wilcoxon rank-sum test followed by the Holm-Sidak's test to correct for multiple comparisons either overall or longitudinally. Region-wise and location-specific analyses in MRI and histology along with overall histology were done using the non-parametric Kruskal-Wallis test followed by Dunn's test to correct for multiple comparisons due to the relatively low sample sizes, and the same applies to the assessment of TEM outcomes. Linear regression analysis was done to evaluate relationships between MRI and histological metrics. This was done for all the stained images after matching of animals who had both MRI and histology samples available at that time series. To

further determine the correlation between MRI and histology metrics, coefficient determination between MRI and histology measures was done using linear regression. In addition, to determine the specificity of MRI metrics to histology, multivariate regression with exhaustive search was performed with every possible permutation. Specifically, this analysis focused on the coherency measure in histology given its promise shown previously[255]. All the statistical analyses were performed using GraphPad Prism 6 (GraphPad Software, San Diego, CA, U.S.). A p-value ≤ 0.05 was considered statistically significant.

Table 3.2: Overall percent changes across de- and remyelination time points in MRI metrics with associated trends (arrowed).

Time Points	Overall Percent (%) Difference between time points				
	FA	MD	NDI	ODI	Angular entropy
Week 2 to week 4 on diet	(31 ± 4)%↓	(81 ± 8)%↑	(15 ± 5)%↓	(41 ± 3)%↑	(50 ± 14)%↑
Week 4 to week 6 on diet	(20 ± 3)%↓	(17 ± 1)%↑	(27 ± 1)%↓	(22 ± 3)%↑	(54 ± 9)%↑
Week 6 to 1week after diet	(16 ± 6)%↑	(5 ± 1)%↓	(6 ± 1)%↑	(51 ± 6)%↓	(111 ± 27)%↓
1week to 3week after diet	(24 ± 5)%↑	(3 ± 1)%↓	(6 ± 1)%↑	(19 ± 3)%↓	(72 ± 11)%↓
3week to 6week after diet	(19 ± 6)%↑	(12 ± 1)%↓	(6 ± 1)%↑	(16 ± 5)%↓	(33 ± 10)%↓
6week to 8week after diet	(22 ± 6)%↑	(15 ± 4)%↓	(10 ± 2)%↑	(12 ± 4)%↓	(24 ± 10)%↓

Table 3.3: Longitudinal animal percent changes across de- and remyelination time points in MRI metrics with associated trends (arrowed).

Time Points	Longitudinal cohort (%) Difference between time points				
	FA	MD	NDI	ODI	Angular entropy
Week 2 to week 4 on diet	(24 ± 3)%↓	(93 ± 22)%↑	(13 ± 5)%↓	(42 ± 4)%↑	(53 ± 11)%↑
Week 4 to week 6 on diet	(20 ± 9)%↓	(22 ± 5)%↑	(25 ± 5)%↓	(29 ± 7)%↑	(88 ± 8)%↑
Week 6 to 1week after diet	(21 ± 8)%↑	(11 ± 1)%↓	(5 ± 1)%↑	(54 ± 10)%↓	(600 ± 89)%↓
1week to 3week after diet	(17 ± 5)%↑	(4 ± 2)%↓	(2 ± 0)%↑	(30 ± 14)%↓	(105 ± 39)%↓
3week to 6week after diet	(18 ± 3)%↑	(9 ± 1)%↓	(5 ± 1)%↑	(11 ± 4)%↓	(18 ± 9)%↓
6week to 8week after diet	(19 ± 5)%↑	(13 ± 4)%↓	(11 ± 3)%↑	(13 ± 9)%↓	(68 ± 9)%↓

3.3 Results

3.3.1 Sample Characteristics

Demyelination was successfully induced in all 27 mice fed with cuprizone. Lesions were seen in the corpus callosum over multiple slices of MRI while on the cuprizone diet in each animal, followed by progressive remyelination and axonal recovery after cessation of cuprizone diet for a sample animal (Fig. 3.4, 3.5, 3.6, 3.7, 3.8). None of the 2 control mice show any pathological changes at any imaged time point. This observation revalidates the reliability of the cuprizone model in successful induction of de- and remyelination.

3.3.2 MRI of the Whole Corpus Callosum Detected Changes Associated with De- and Remyelination over Time and Across all the Animals

We first examined the overall trend of tissue injury and repair in the cuprizone model using different MRI metrics (FA, MD, NDI, ODI, and angular entropy), quantified over the whole corpus callosum. Overall, all normalized diffusion and texture metrics showed significant changes ($p \leq 0.05$) over multiple time points. FA and NDI decreased whereas MD, ODI, and angular entropy increased during demyelination time points relative to week 2 on diet. The opposite trend was observed across all the metrics at remyelination time points (Fig. 3.9). In addition, when observing changes over the 5 longitudinal animals imaged throughout the study period over all 7 time points, the similar pattern of changes was detected in all MRI metrics (Fig. 3.10).

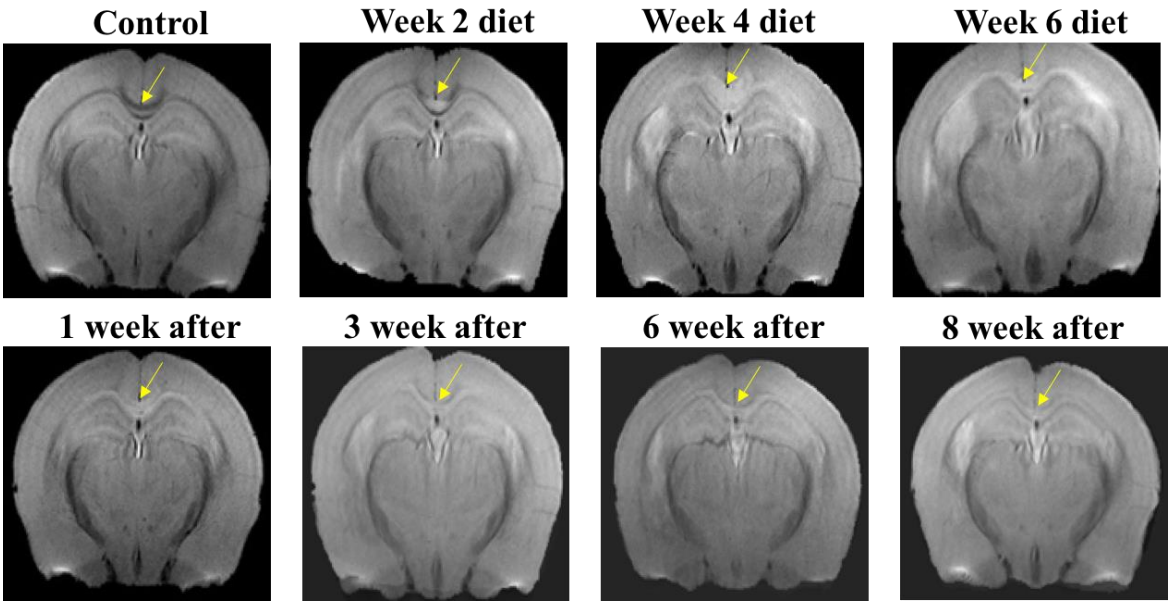

Fig. 3.4: Changes in signal intensity on T2 MRI. Example MRI metrics showing changes in signal intensity of corpus callosum region splenium (arrowed) over time. T2-weighted images showed increase in signal intensity over corpus callosum on cuprizone diet and gradual decrease in signal intensity after cessation of cuprizone from diet.

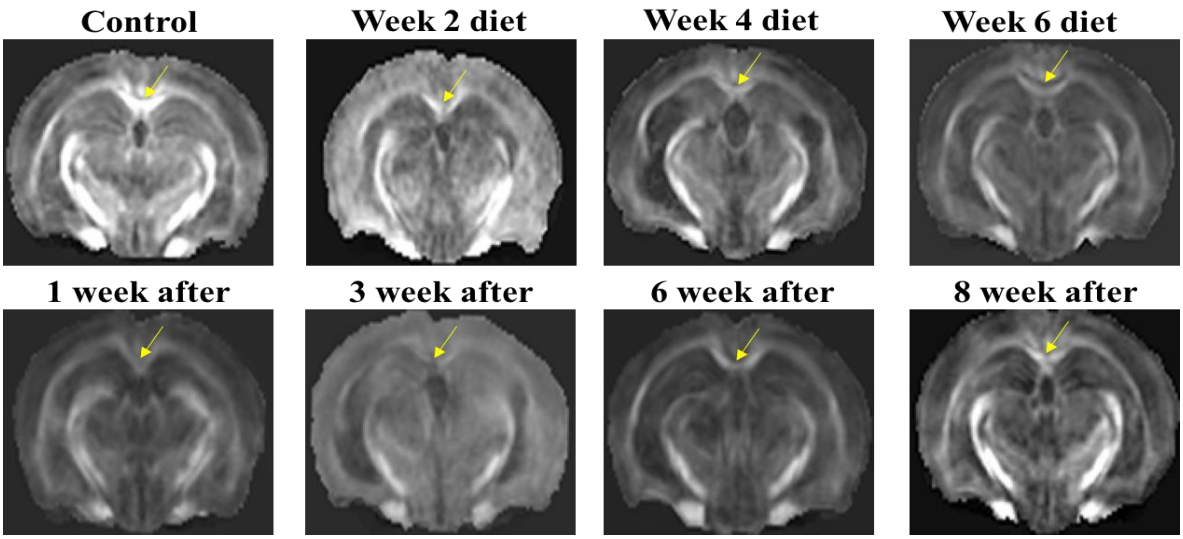

Fig. 3.5: Changes in signal intensity on DTI metric FA. FA showed gradual signal intensity decrease (arrowed) on cuprizone diet and increase over time after cessation of cuprizone from diet.

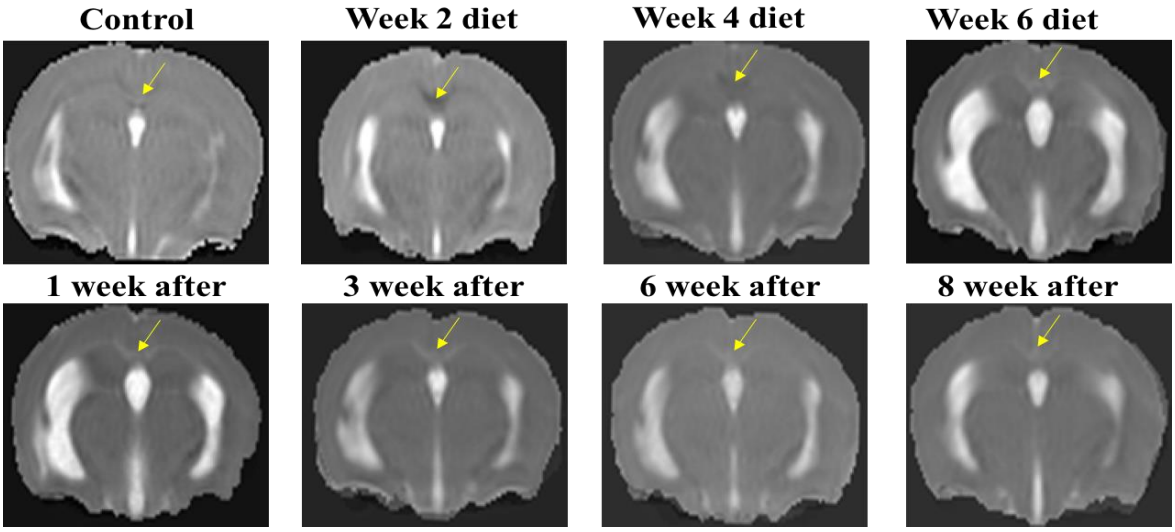

Fig. 3.6: Changes in signal intensity on DTI metric MD. MD signal intensity increased on cuprizone diet (arrowed) and decreased after cessation of cuprizone from diet.

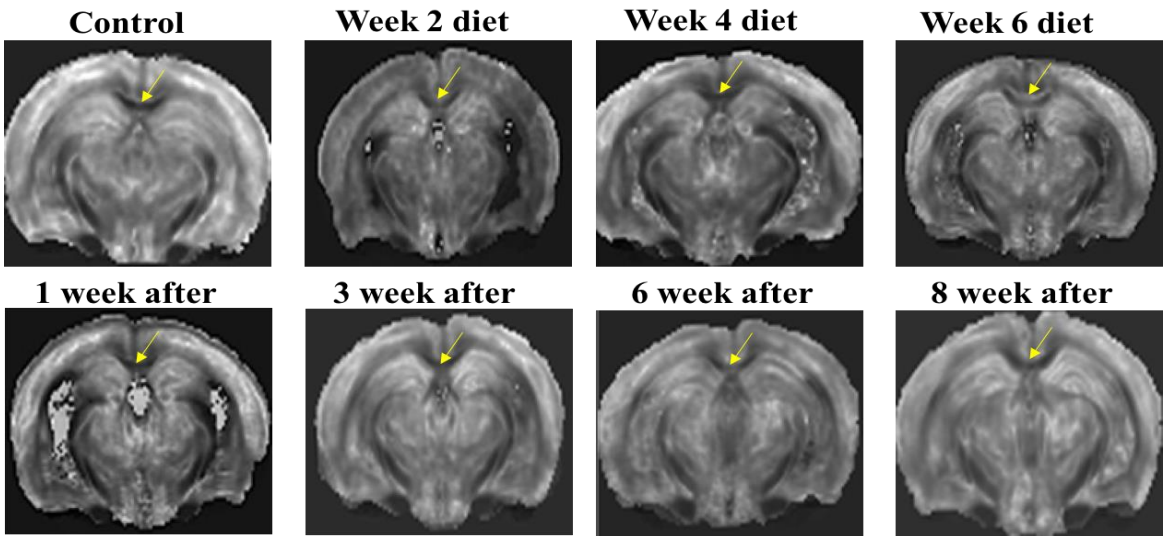

Fig. 3.7: Changes in signal intensity on NODDI metric ODI. ODI signal intensity increased on cuprizone diet (arrowed) and decreased after removal of cuprizone from diet.

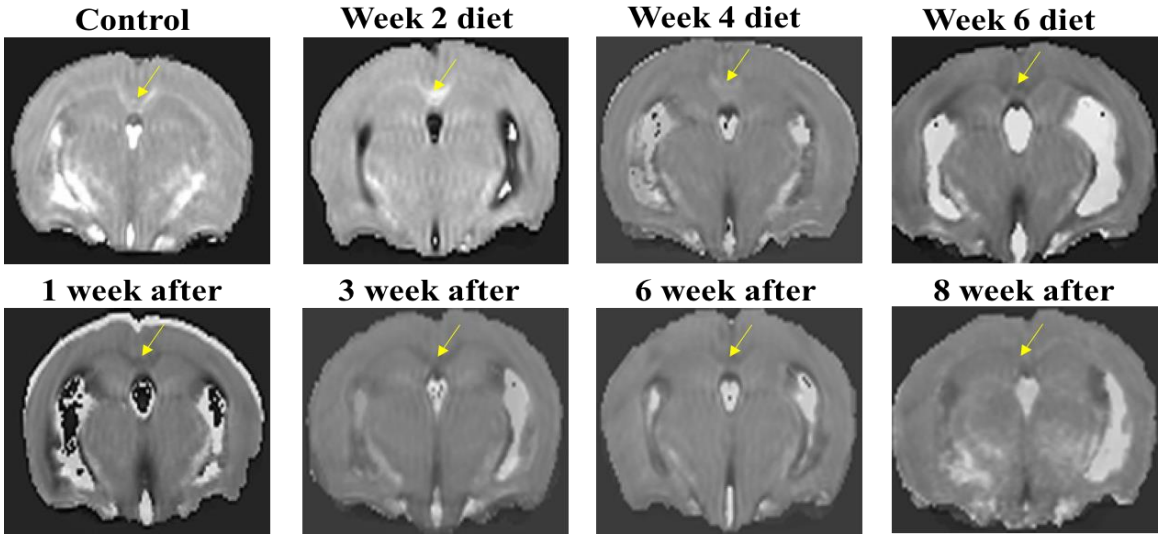

Fig. 3.8: Changes in signal intensity on NODDI metric NDI. NDI signal intensity decreased on cuprizone diet (arrowed) and increased gradually after cessation of cuprizone from diet.

Specifically, FA decreased by (51 ± 7)% from week 2 to week 6 on cuprizone diet across all the animals; (44 ± 12)% decrease in the longitudinal mice. After cessation of cuprizone from diet, FA increased (16 ± 6)% after 1 week, and (65 ± 16)% from 1 week to 8 weeks; (75 ± 21)% in the longitudinal mice (Table. 3.2, 3.3) (Fig. 3.9A, 3.10A). Likewise, for all and the longitudinal cohorts respectively, the MD increased by (98 ± 9)% and (115 ± 27)% from week 2 to week 6 on cuprizone diet, and decreased by (35 ± 7)% and (37 ± 8)% after cessation of cuprizone (Table. 3.2, 3.3) (Fig. 3.9B, 3.10B).

In a similar trend, from week 2 to week 6 on cuprizone diet, the decrease in all and longitudinal mice respectively was (42 ± 6)% and (38 ± 1)% in NDI, (63 ± 6)% and (71 ± 11)% increase in ODI, and (104 ± 23)% and (141 ± 19)% increase in angular entropy. Conversely, after removal of cuprizone from diet, there was an increase in the mice that was (28 ± 5)% and (23 ± 5)% in NDI, (98 ± 18)% and (108 ± 37)% decrease in ODI, and (240 ± 58)% and (7 1 ± 146)% decrease in angular entropy for all and longitudinal cohorts respectively (Table. 3.2, 3.3) (Fig. 3.9C, 3.9D, 3.9E, 3.10C, 3.10D, 3.10E).

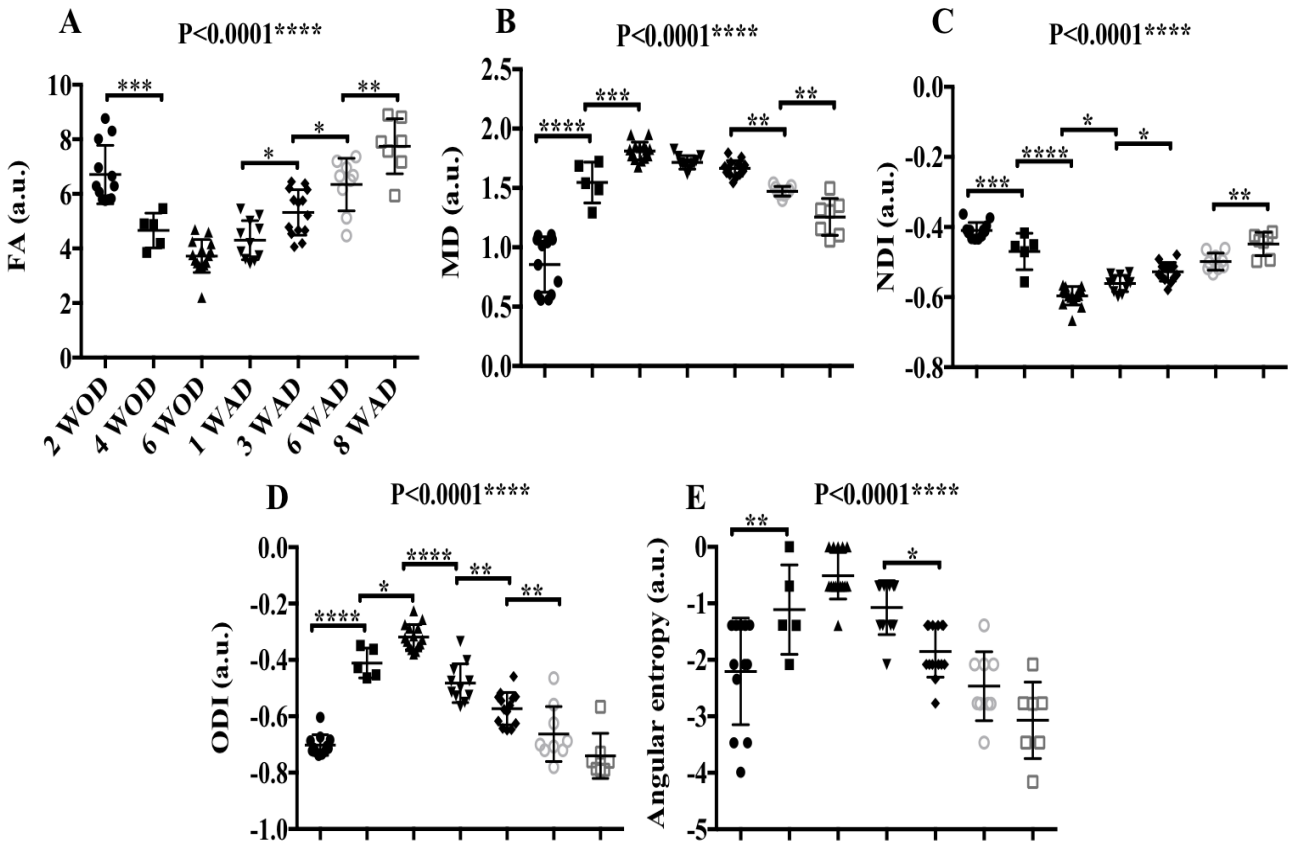

Fig. 3.9: Overall MRI trend in corpus callosum across all animals. MRI metrics by quantifying corpus callosum as a whole over time detected demyelination with axonal changes on cuprizone diet (WOD) and remyelination with axonal recovery after removal of cuprizone from diet (WAD) in FA (A), MD (B), NDI (C), ODI (D), and Angular entropy (E).

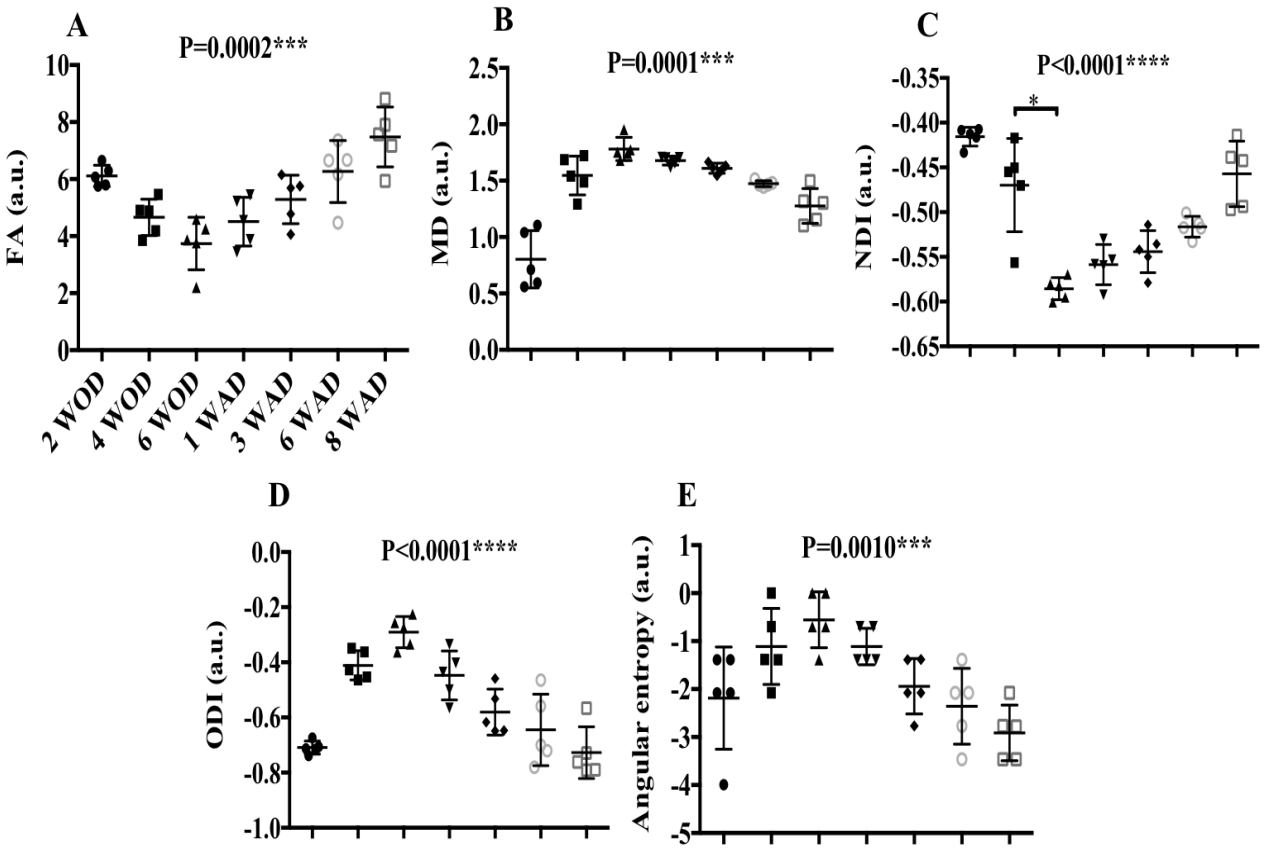

Fig. 3.10: Overall MRI trend in corpus callosum across longitudinal animals. MRI metrics by quantifying corpus callosum as a whole over time series to detected axonal changes with de- and remyelination in FA (A), MD (B), NDI (C), ODI (D), Angular entropy (E) and showed similar changes as all.

3.3.3 Histological Structure Tensor Analysis and TEM Measures Corresponded to Advanced MRI Metrics

De- and remyelination status over the whole corpus callosum on structure tensor analysis outcomes showed similar changing patterns to that from MRI, and this was consistent across all stained images: EC, ORO, MBP, and NF-H. There was a gradual decrease in coherency and an

increase in energy and circular variance values in mice during the period of cuprizone diet. An inverse relationship in all the maps across all the staining was seen after cessation of cuprizone from diet. All the structure tensor maps showed significant changes ($p \leq 0.05$) over multiple time points. Visually, the EC and MBP showed progressive loss of myelin staining during the demyelination time points and gradual resolution of myelination status over remyelination time points. The NF-H staining showed the similar pattern of changes in axons of the corresponding regions of the corpus callosum. The ORO suffered the most tissue distortion and bubbling as compared to the other staining methods, the pattern of presence and removal of myelin debris appeared to support the time course of de- and remyelination (Supp. Fig. 3.1 - 3.4).

Quantitatively, the EC coherency decreased by $(15 \pm 2)\%$ from week 2 to week 6 on cuprizone diet across all the animals and increased $(16 \pm 5)\%$ after cessation of cuprizone from diet (Fig. 3.11A). Likewise, the ORO decreased by $(21 \pm 4)\%$ from week 2 to week 6 on cuprizone diet and increased by $(39 \pm 5)\%$ after cessation of cuprizone (Fig. 3.11B). In a similar trend, from week 2 to week 6 on cuprizone diet, the decrease in all mice respectively was $(11 \pm 3)\%$ in MBP and $(19 \pm 3)\%$ in NF-H. Conversely, after removal of cuprizone from diet, there was an increase in the mice that was $(12 \pm 4)\%$ in MBP and $(29 \pm 4)\%$ in NF-H coherency (Fig. 3.11C, 3.11D). Coherency maps in all the staining showed significant changes across multiple remyelination time points; with the MBP map showing the least change.

The EC energy increased by $(108 \pm 8)\%$ from week 2 to week 6 on cuprizone diet across all the animals and decreased $(33 \pm 27)\%$ after cessation of cuprizone from diet (Fig. 3.15A). Likewise, the ORO increased by $(91 \pm 36)\%$ from week 2 to week 6 on cuprizone diet and decreased by $(58 \pm 45)\%$ after cessation of cuprizone (Fig. 3.15B). In a similar trend, from week

2 to week 6 on cuprizone diet, the increase in all mice respectively was (6 ± 9)% in MBP and (107 ± 26)% in NF-H. Conversely, after removal of cuprizone from diet, there was a decrease in the mice that was (14 ± 21)% in MBP and (26 ± 35)% in NF-H energy (Fig. 3.15C, 3.15D). MBP energy maps in both de- and remyelination time points did not show significant changes.

The EC circular variance increased by (30 ± 14)% from week 2 to week 6 on cuprizone diet across all the animals and decreased (24 ± 19)% after cessation of cuprizone from diet (Fig. 3.19A). Likewise, the ORO increased by (45 ± 14)% from week 2 to week 6 on cuprizone diet and decreased by (41 ± 20)% after cessation of cuprizone (Fig. 3.19B). In a similar trend, from week 2 to week 6 on cuprizone diet, the increase in all mice respectively was (16 ± 14)% in MBP and (17 ± 9.0)% in NF-H. Conversely, after removal of cuprizone from diet, there was a decrease in the mice that was (40 ± 21)% in MBP and (34 ± 15)% in NF-H circular variance (Fig. 3.19C, 3.19D).

Based on TEM analyses, the mean ± standard error myelin g-ratio was 0.8206 ± 0.0509 in cuprizone-fed mice 6 weeks after cessation of cuprizone diet, and 0.7357 ± 0.0285 in control mice at the same time point. At 8 weeks after cessation of cuprizone diet, the g-ratio was 0.7543 ± 0.0383 in the cuprizone mice, decreased by (8 ± 1)% from 6 weeks after in these mice. Compared to controls, the cuprizone-fed mice showed a (12 ± 2)% and (3 ± 1)% increase in myelin g-ratio at 6 and 8 weeks after cessation of cuprizone diet respectively (Fig. 3.23).

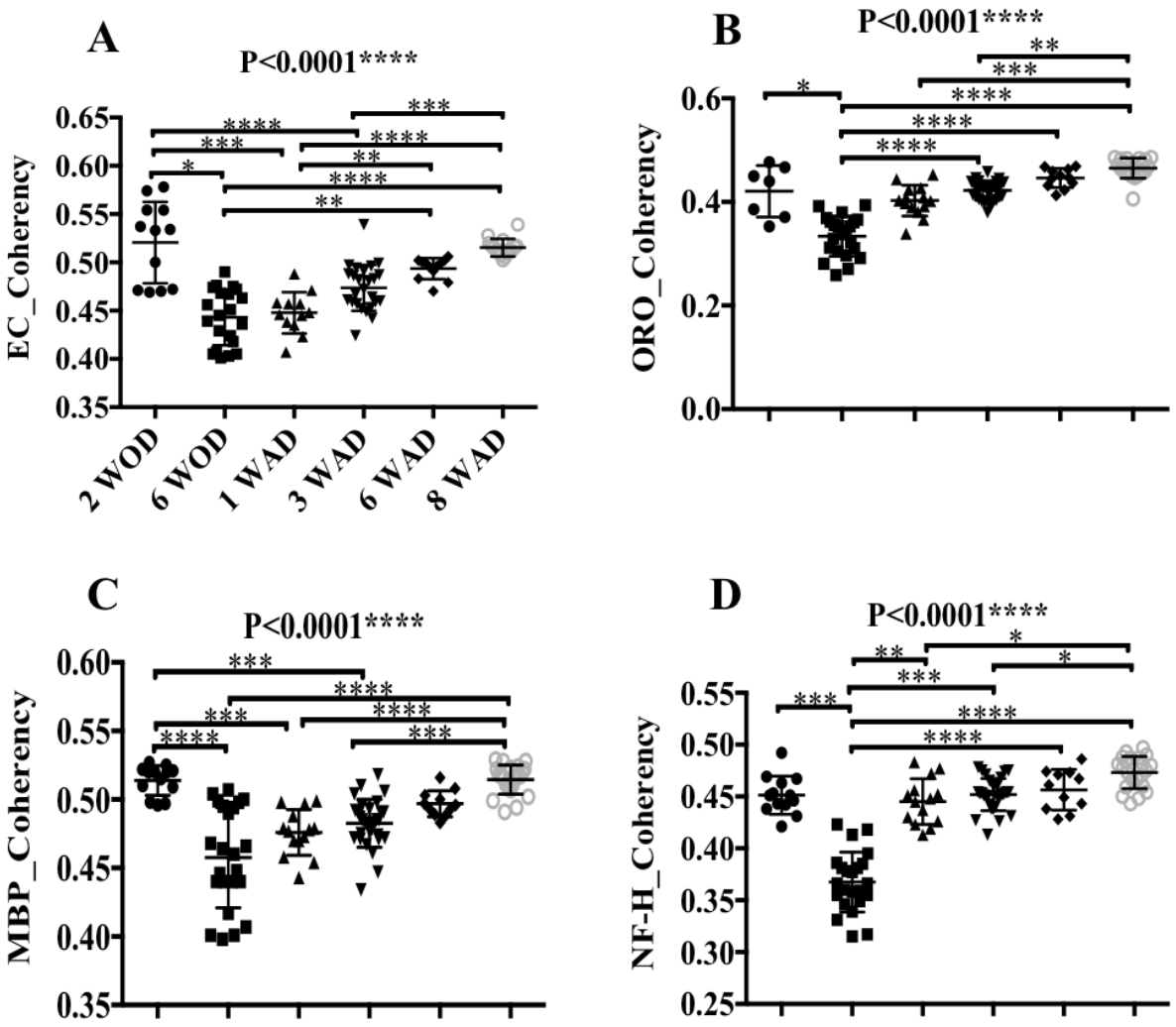

Fig. 3.11: Overall structure tensor coherency changes. Histology structure tensor coherency maps in corpus callosum showed decrease in coherency on cuprizone diet and increase after removal of cuprizone from diet in EC (A), ORO (B), MBP (C), and NF-H (D) over time.

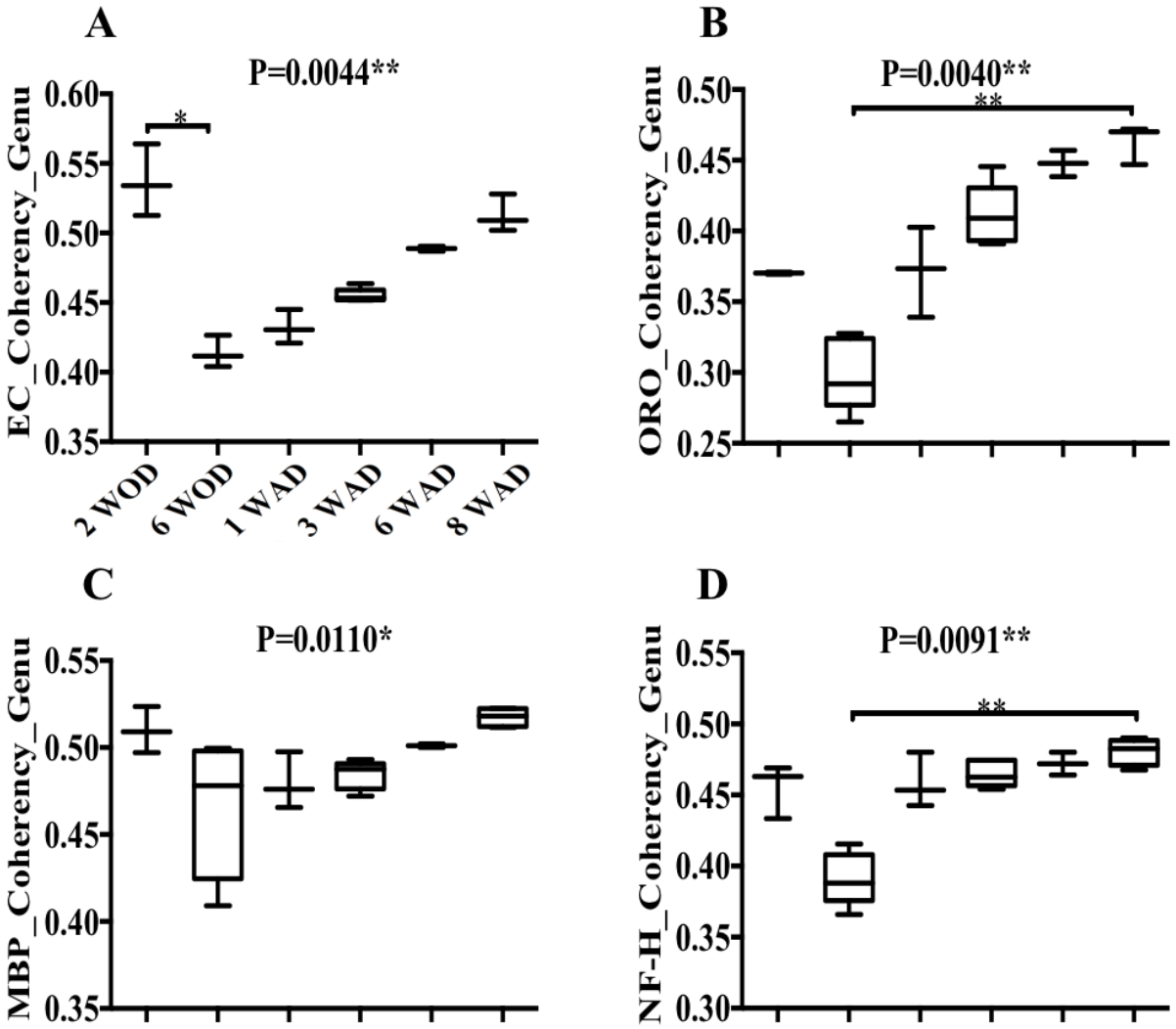

Fig. 3.12: Region-wise coherency changes in genu. Histology structure tensor coherency maps over genu showed similar trend as overall in EC (A), ORO (B), MBP (C), and NF-H (D).

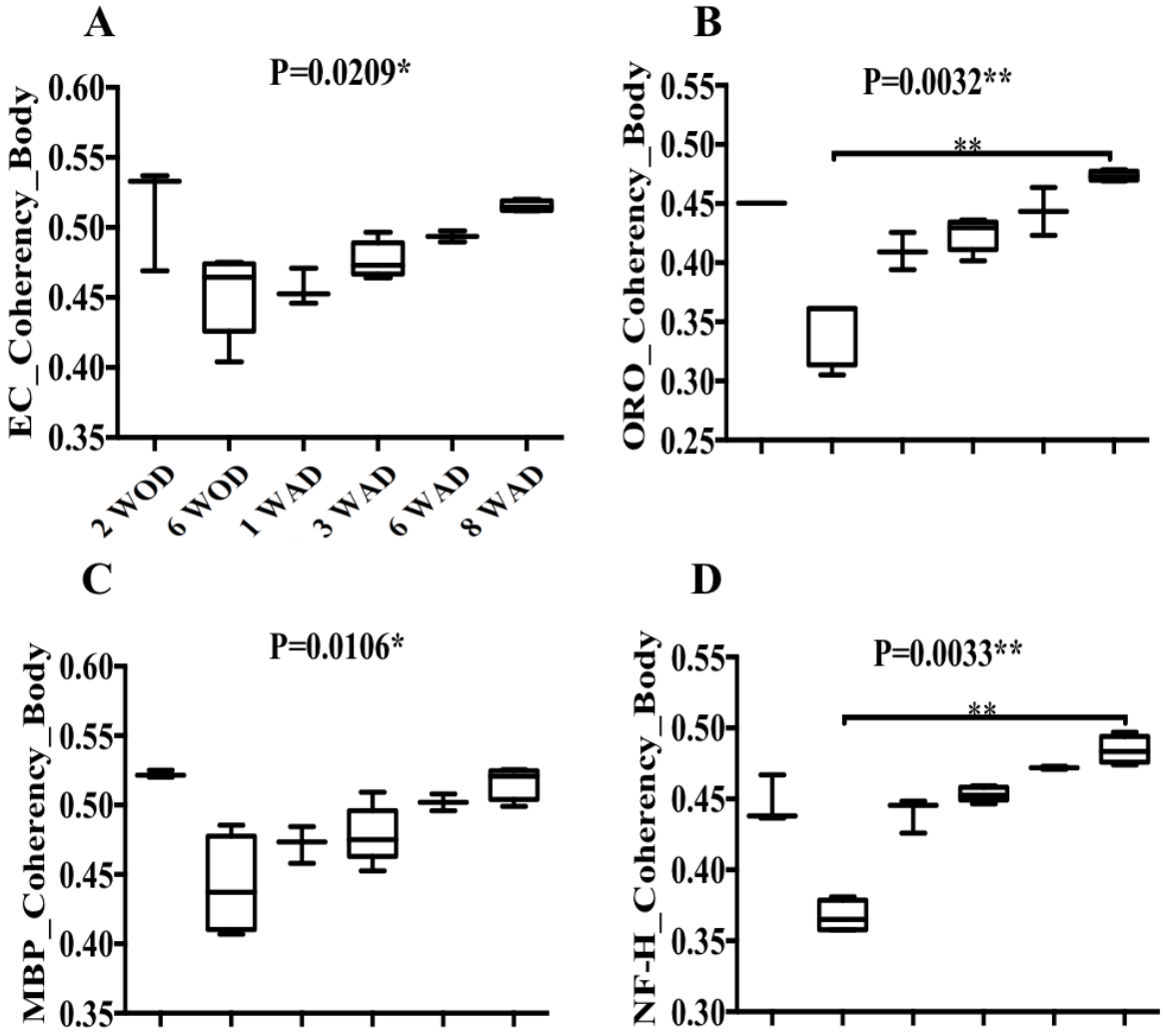

Fig. 3.13: Region-wise coherency changes in body. Histology structure tensor coherency maps over body showed similar trend as overall in EC (A), ORO (B), MBP (C), and NF-H (D).

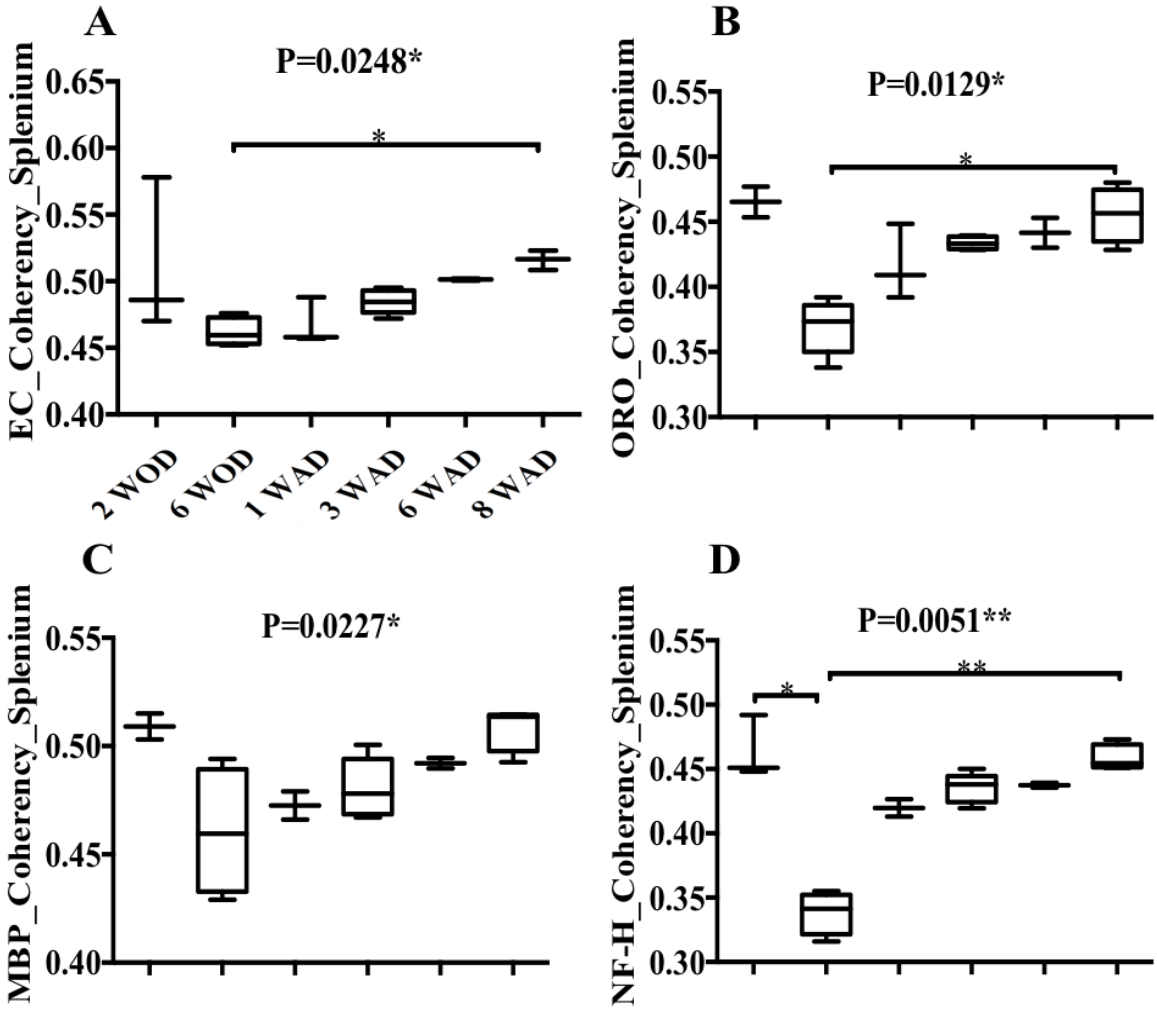

Fig. 3.14: Region-wise coherency changes in splenium. Histology structure tensor coherency maps over splenium showed similar trend as overall in EC (A), ORO (B), MBP (C), and NF-H (D).

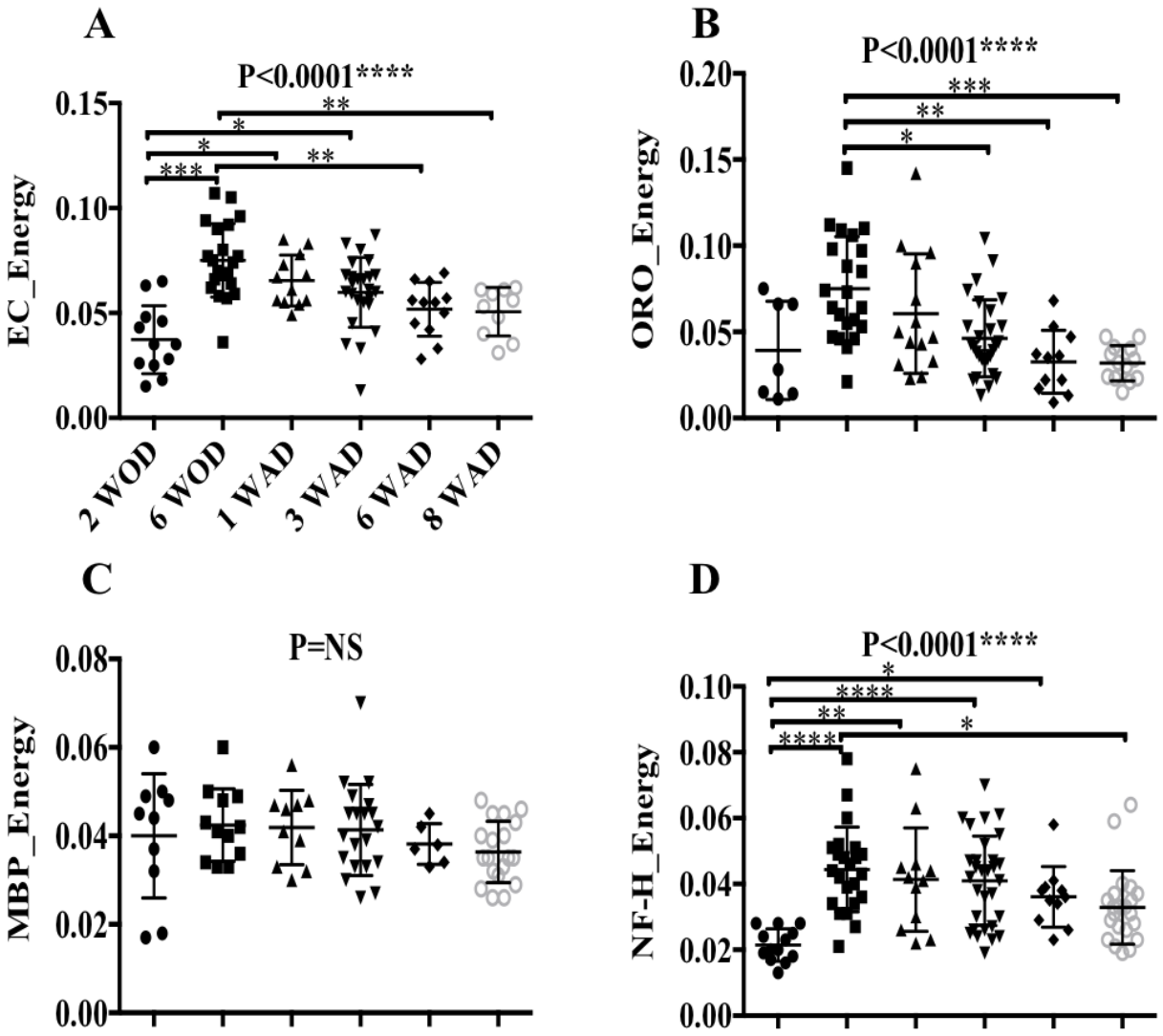

Fig. 3.15: Overall structure tensor energy changes. Histology structure tensor energy maps in corpus callosum showed increase in energy on cuprizone diet and decrease after removal of cuprizone from diet in EC (A), ORO (B), MBP (C), and NF-H (D) over time.

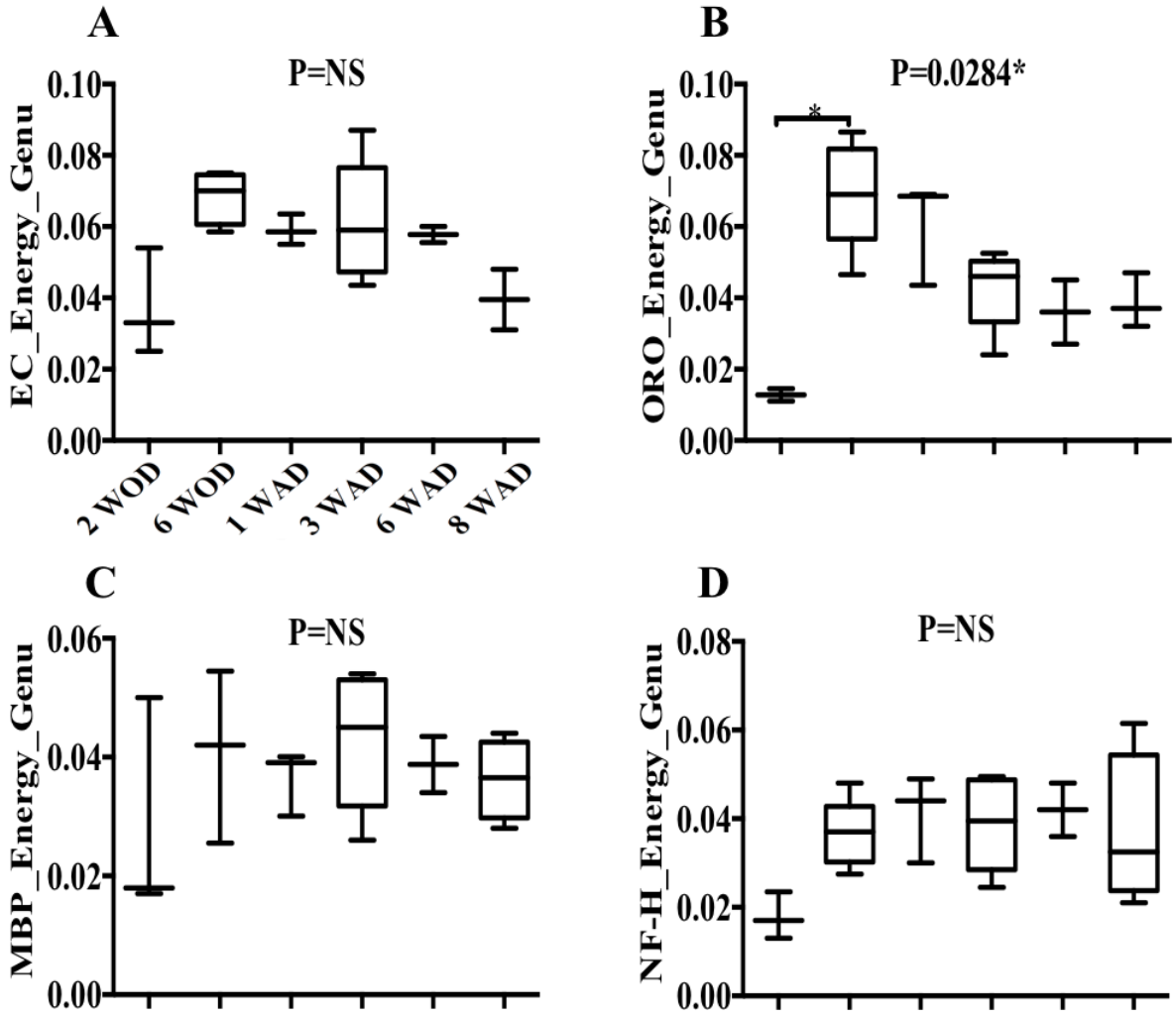

Fig. 3.16: Region-wise energy changes in genu. Histology structure tensor energy maps over genu showed similar trend as overall in EC (A), ORO (B), MBP (C), and NF-H (D).

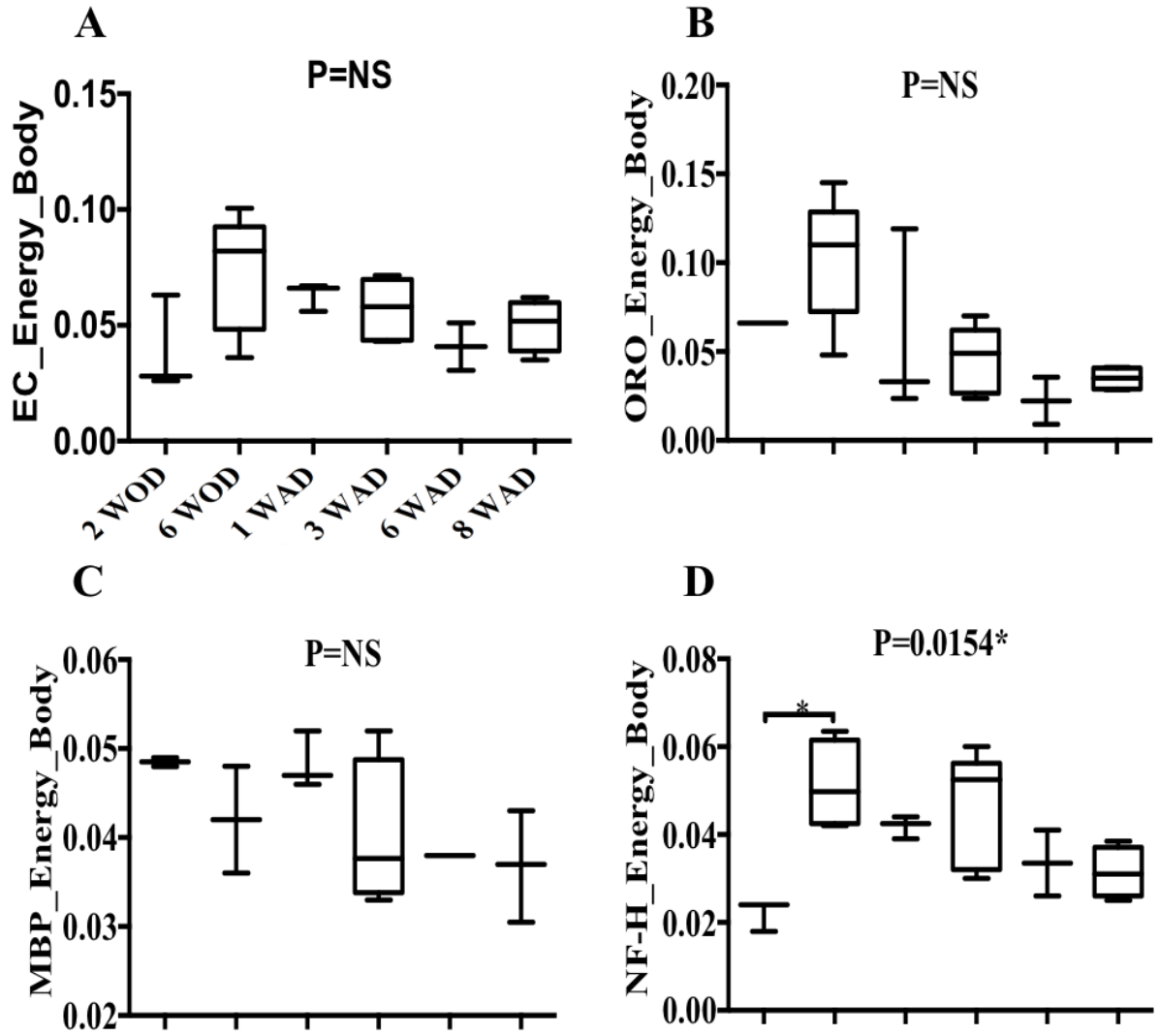

Fig. 3.17: Region-wise energy changes in body. Histology structure tensor energy maps over body showed similar trend as overall in EC (A), ORO (B), MBP (C), and NF-H (D).

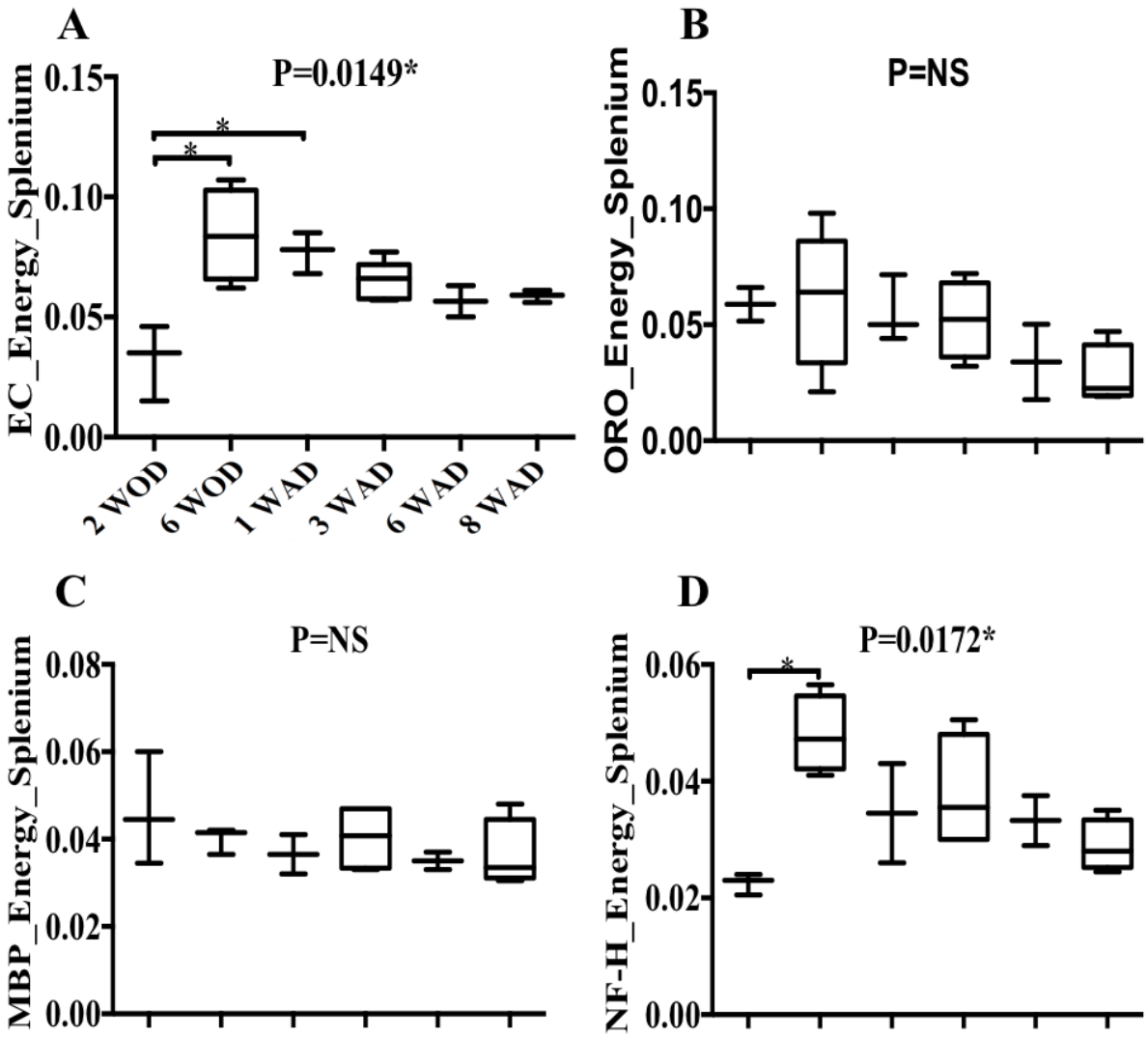

Fig. 3.18: Region-wise energy changes in splenium. Histology structure tensor energy maps over splenium showed similar trend as overall in EC (A), ORO (B), MBP (C), and NF-H (D).

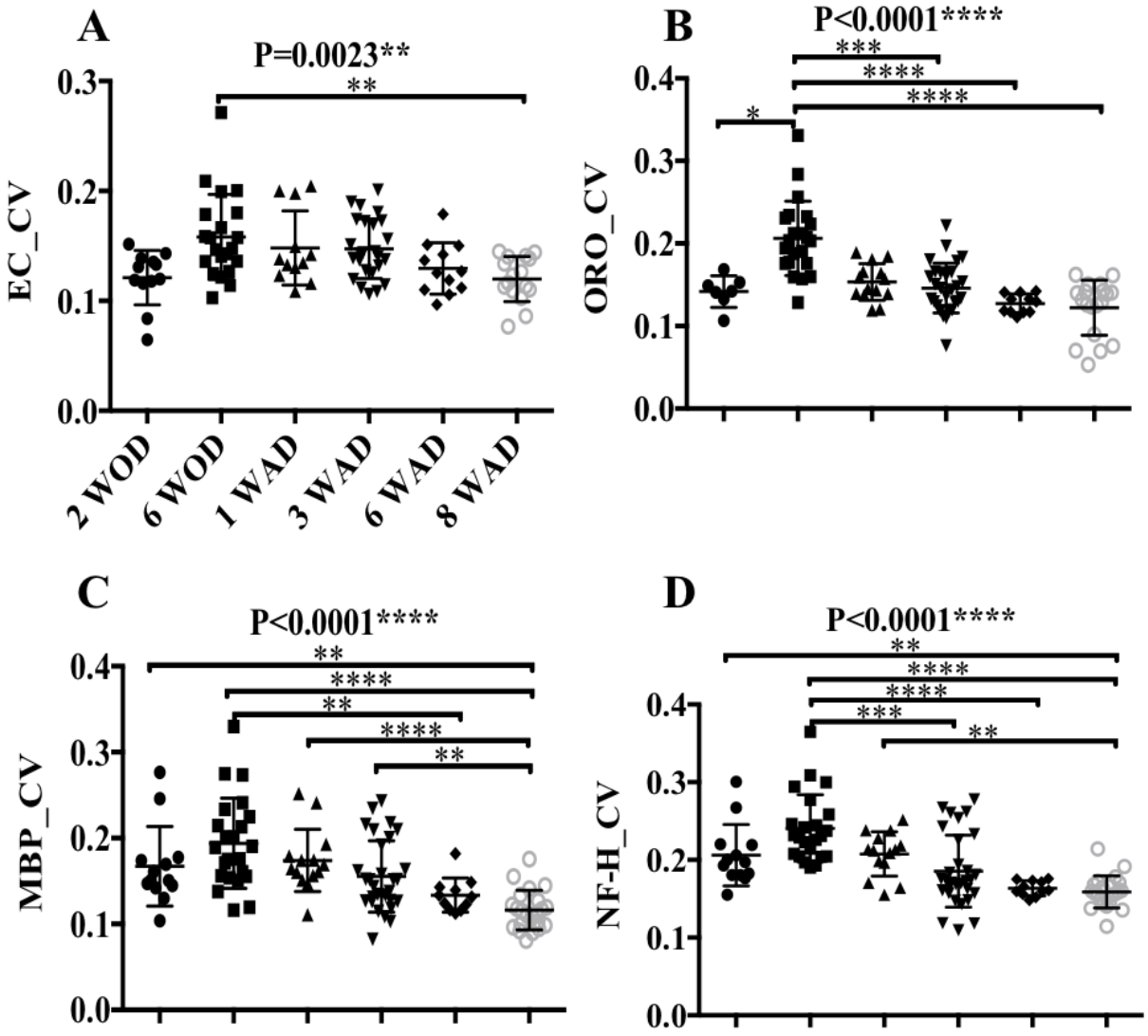

Fig. 3.19: Overall structure tensor circular variance (CV) changes. Histology structure tensor CV maps in corpus callosum showed increase in variance on cuprizone diet and decrease after removal of cuprizone from diet in EC (A), ORO (B), MBP (C), and NF-H (D) over time.

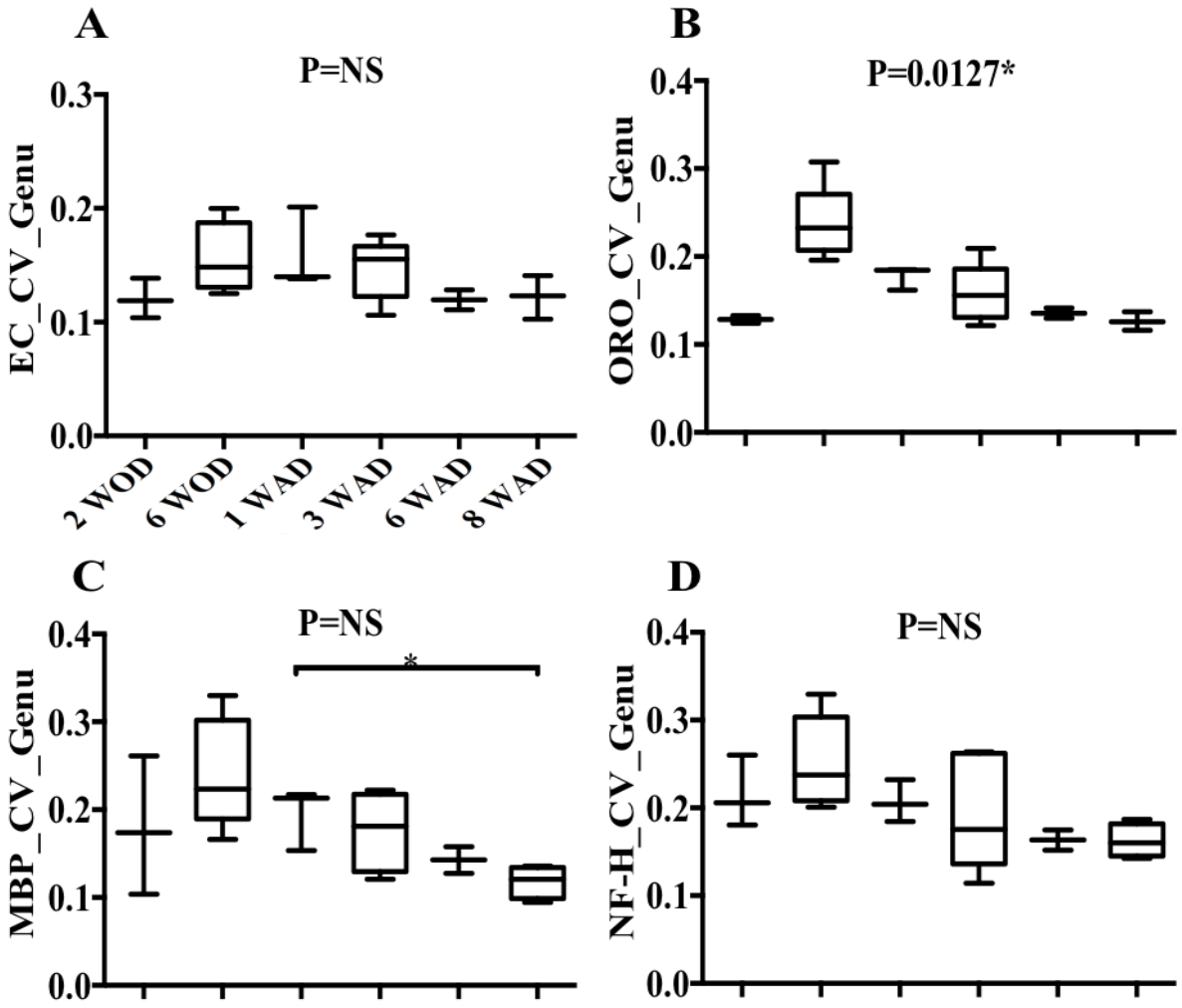

Fig. 3.20: Region-wise CV changes in genu. Histology structure tensor CV maps over genu showed similar trend as overall in EC (A), ORO (B), MBP (C), and NF-H (D).

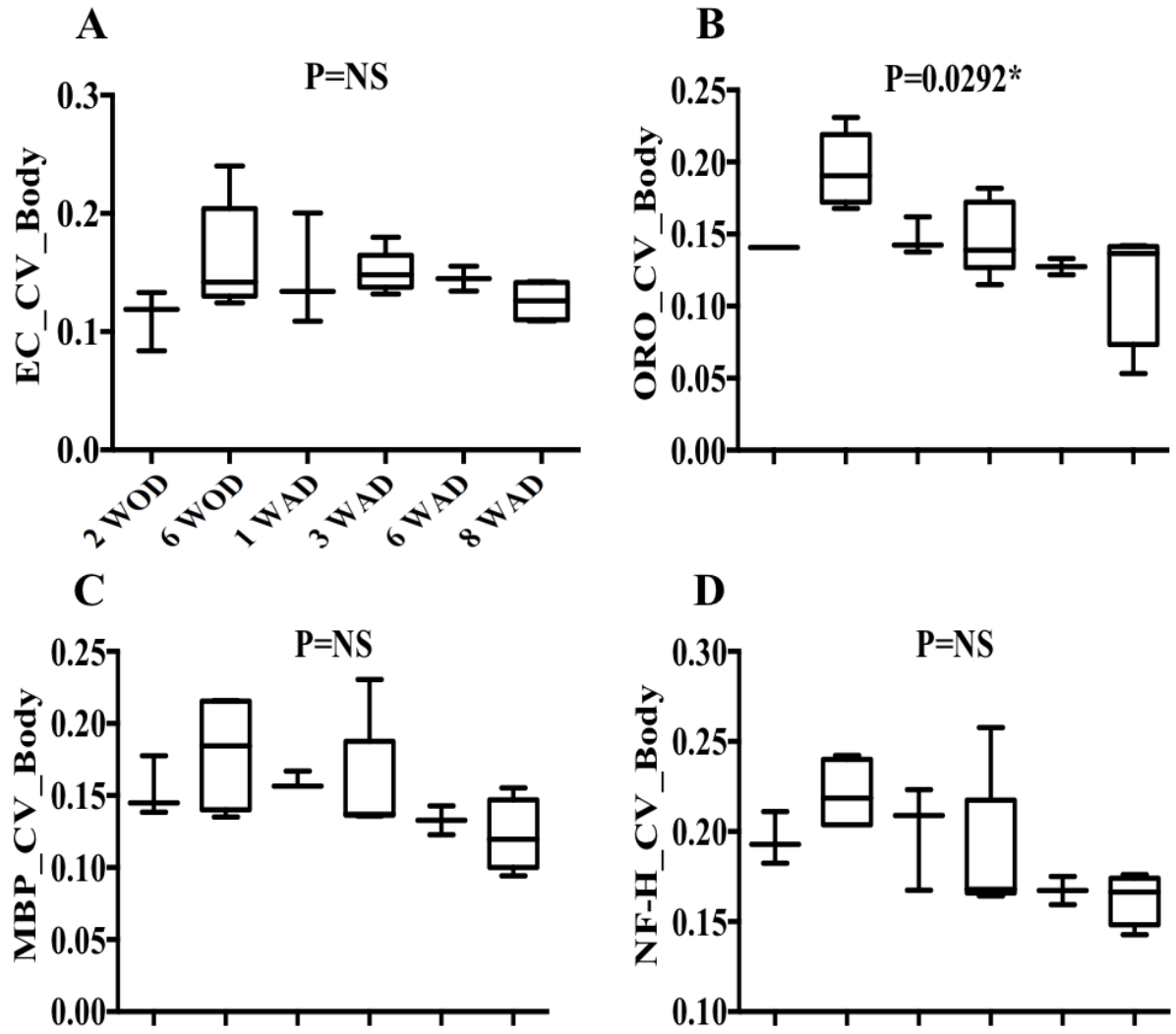

Fig. 3.21: Region-wise CV changes in body. Histology structure tensor CV maps over body showed similar trend as overall in EC (A), ORO (B), MBP (C), and NF-H (D).

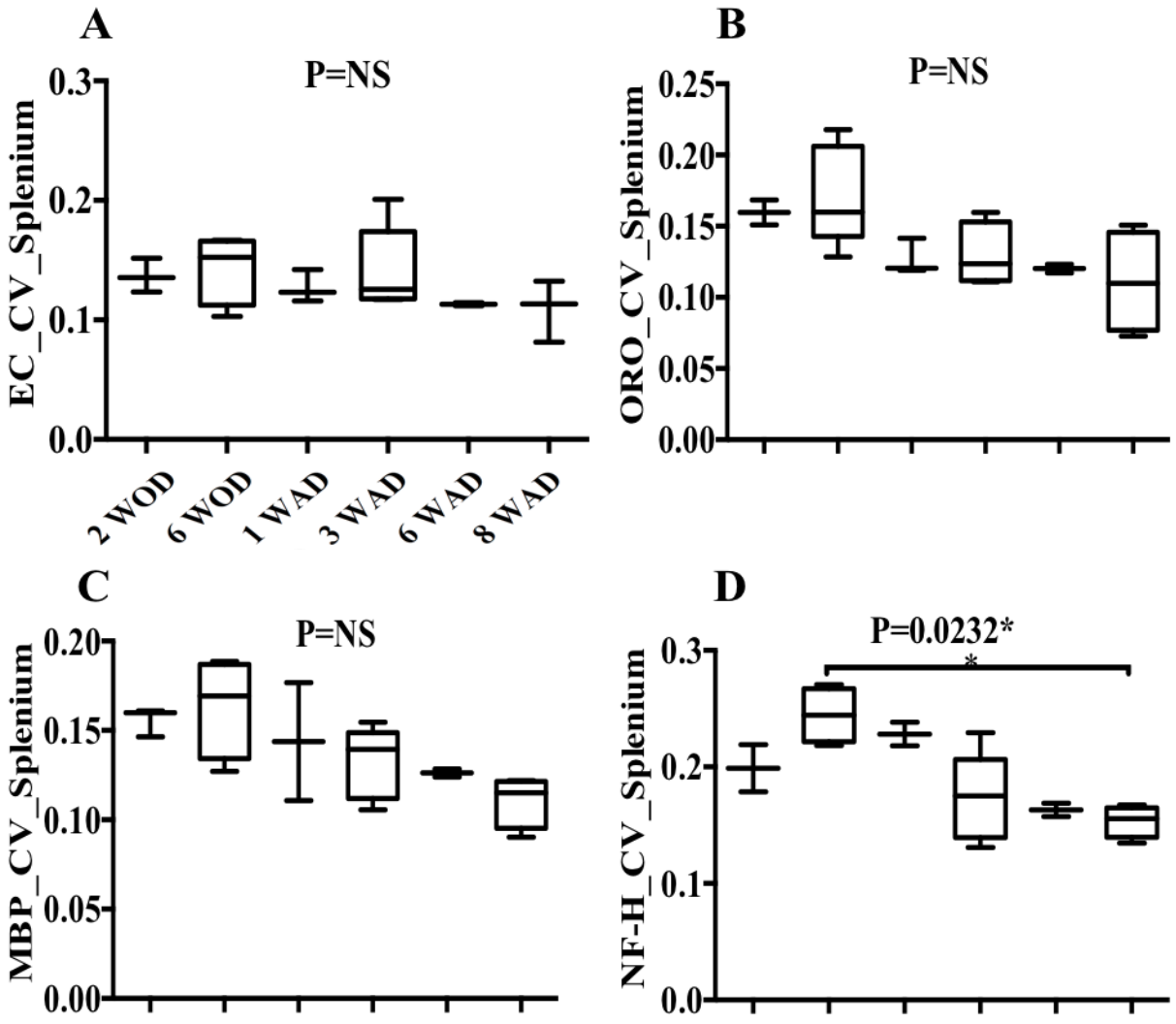

Fig. 3.22: Region-wise CV changes in splenium. Histology structure tensor CV maps over splenium showed similar trend as overall in EC (A), ORO (B), MBP (C), and NF-H (D).

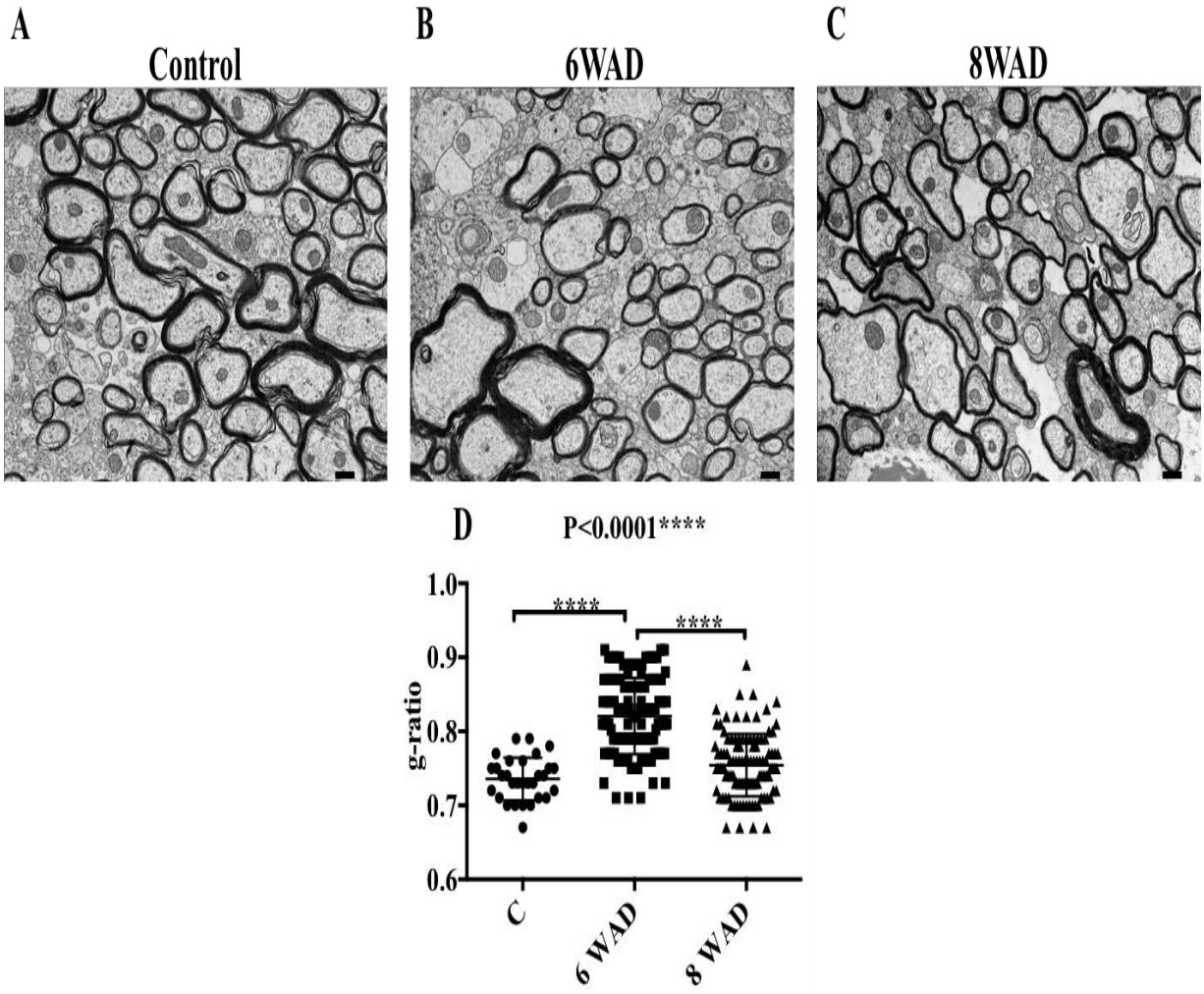

Fig. 3.23: Myelin g-ratio. Example TEM image of control, cuprizone-fed mice at 6 WAD, and 8 WAD showed remyelination of cuprizone-fed mice over time. Control animal splenium had uniform myelin sheath around axons (A), 6 WAD animal had axons with variable degree of remyelination (B), and 8 WAD animal had relatively higher myelinated axons (C). Control animal g-ratio was lower indicating healthy myelinated axons whereas cuprizone-fed animals had higher g-ratio indicating remyelinated axons (D). Scale bar represents 500 nm.

3.3.4 The Genu Showed Early De- and Remyelination and The Splenium Showed Early Demyelination but Relatively Late Repair

Region-wise analysis of MRI in the genu, body, and splenium of the corpus callosum showed trends consistent with analysis of the whole corpus callosum in all except MD (Fig. 3.24, 3.25, 3.26). The map results showed significant changes ($p \leq 0.05$) over multiple time points in each region but the NODDI metrics NDI and ODI ($p < 0.0001$) showed more significant changes at demyelination time points than DTI metric, FA ($p < 0.01$). The genu had a $(20 \pm 4)\%$ decrease in NDI compared to $(9 \pm 2)\%$ decrease in the body and $(13 \pm 3)\%$ decrease in the splenium from week 2 to week 4 on cuprizone diet. The genu, body, and splenium had a further $(27 \pm 1)\%$, $(20 \pm 1)\%$, and $(36 \pm 1)\%$ decrease in NDI respectively from week 4 to week 6 on diet. The genu had an $(8 \pm 1)\%$ increase in NDI from week 6 on cuprizone diet to 1 week after diet whereas body and splenium had a $(3 \pm 1)\%$ and $(7 \pm 2)\%$ increase (Fig. 3.24C, 3.25C, 3.26C). The genu had a $(51 \pm 8)\%$ increase in ODI compared to $(35 \pm 6)\%$ increase in the body and $(37 \pm 4)\%$ increase in the splenium from week 2 to week 4 on cuprizone diet (Fig. 3.24D, 3.25D, 3.26D). The genu, body, and splenium had a further $(19 \pm 5)\%$, $(12 \pm 4)\%$, and $(38 \pm 4)\%$ increase in ODI respectively from week 4 to week 6 on diet. The genu had a $(45 \pm 6)\%$ decrease in ODI from week 6 on cuprizone diet to 1 week after diet whereas the body and splenium had a $(67 \pm 3)\%$ and $(46 \pm 3)\%$ decrease.

FA values gradually decreased in all the corpus callosum regions while on cuprizone diet with a $(20 \pm 31)\%$, $(32 \pm 30)\%$, and $(12 \pm 25)\%$ decrease in the genu, body, and splenium respectively from week 4 to week 6 on cuprizone diet (Fig. 3.24A, 3.25A, 3.26A). The genu had an $(8 \pm 23)\%$ increase in FA at 1 week after diet compared to week 6 on diet, the body had a

(20 ± 47)%, and the splenium had a (12 ± 43)% increase in FA over the same time period. FA values progressively increased in all the corpus callosum regions after removal of cuprizone from diet but the increase of FA in the genu ($p<0.05$) was lower than the body ($p<0.01$) across remyelination time points (Fig. 3.24A, 3.25A, 3.26A). MD showed variable changes and was least sensitive across de- and remyelination time points (Fig. 3.24B, 3.25B, 3.26B).

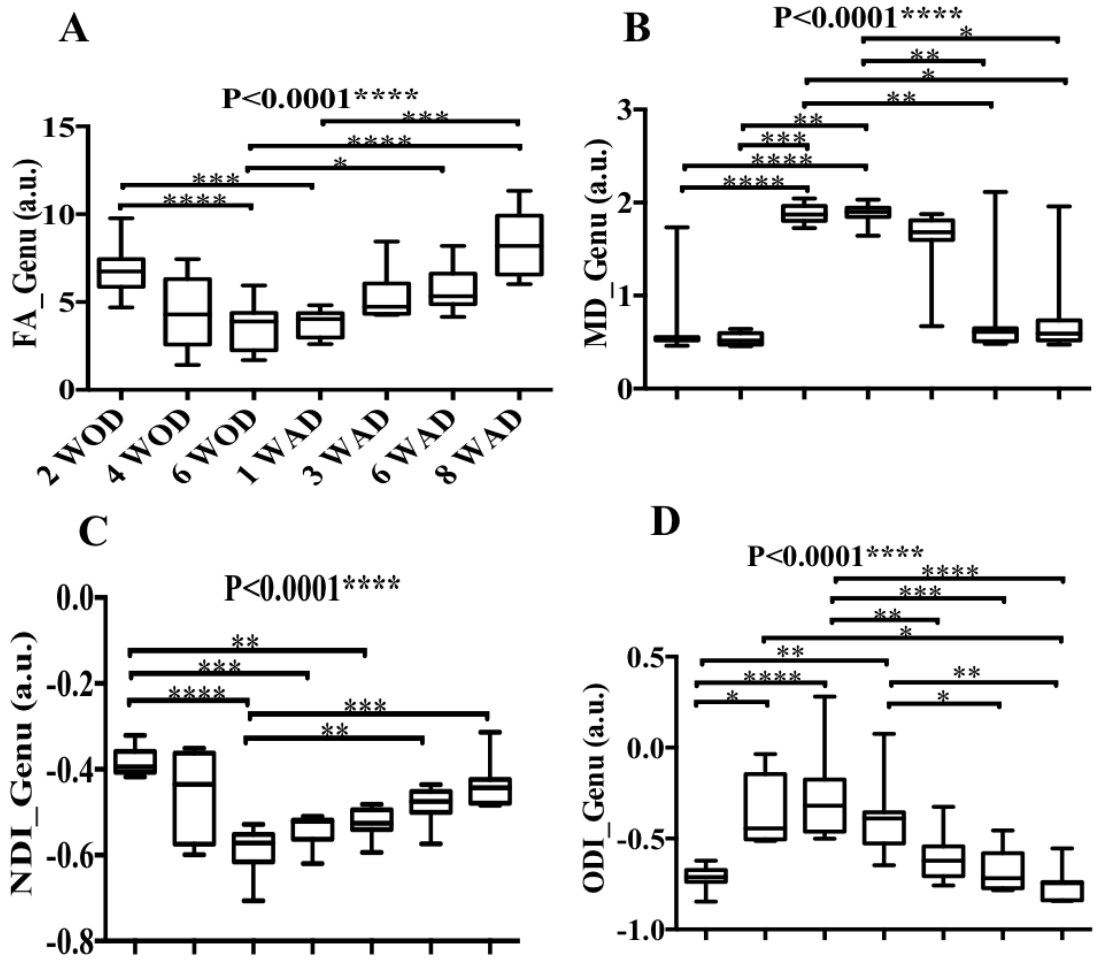

Fig. 3.24: Region-wise changes in MRI on genu. DWI metrics over time detected significant changes over multiple time points in FA (A), MD (B), NDI (C), and ODI (D) in corpus callosum genu and similar trend as overall.

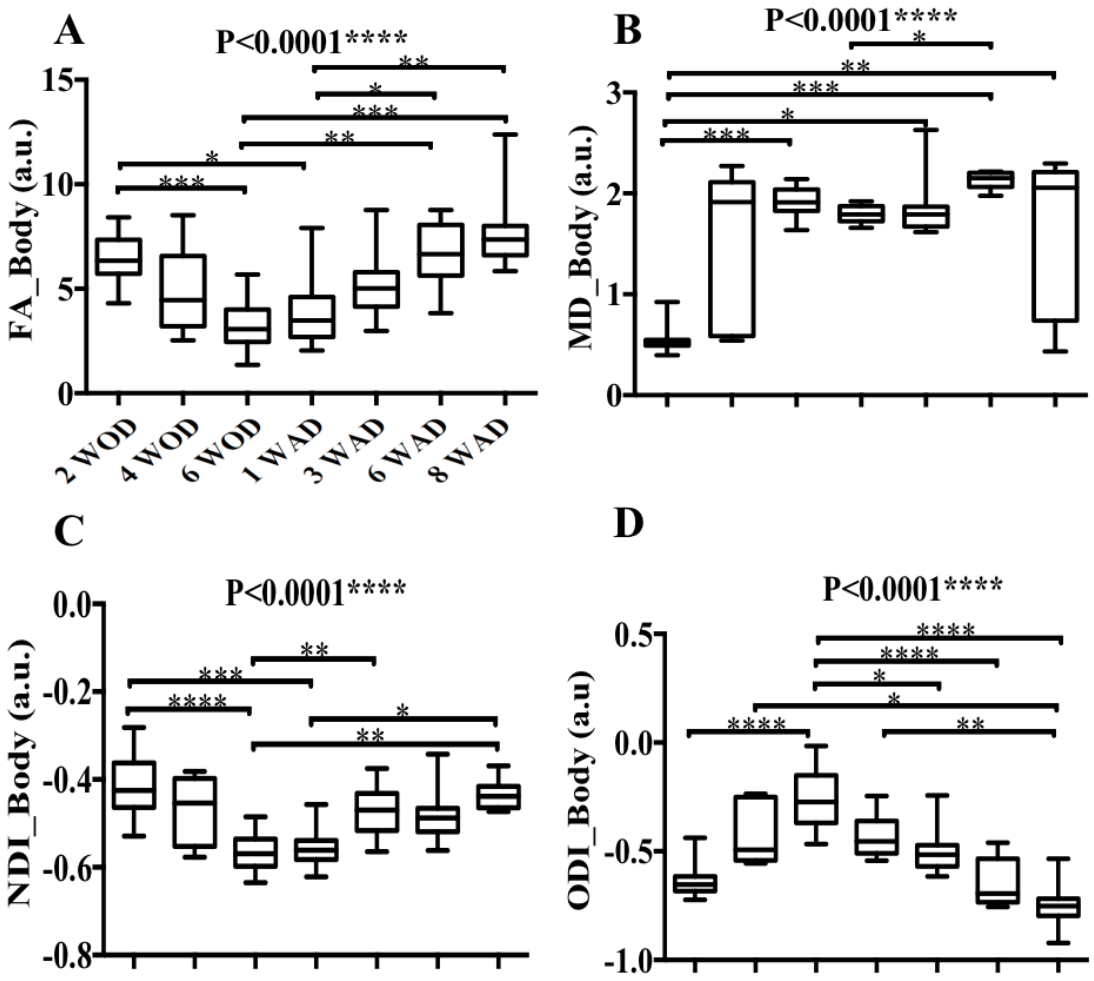

Fig. 3.25: Region-wise changes in MRI on body. DWI metrics over time detected significant changes over multiple time points in FA (A), MD (B), NDI (C), and ODI (D).

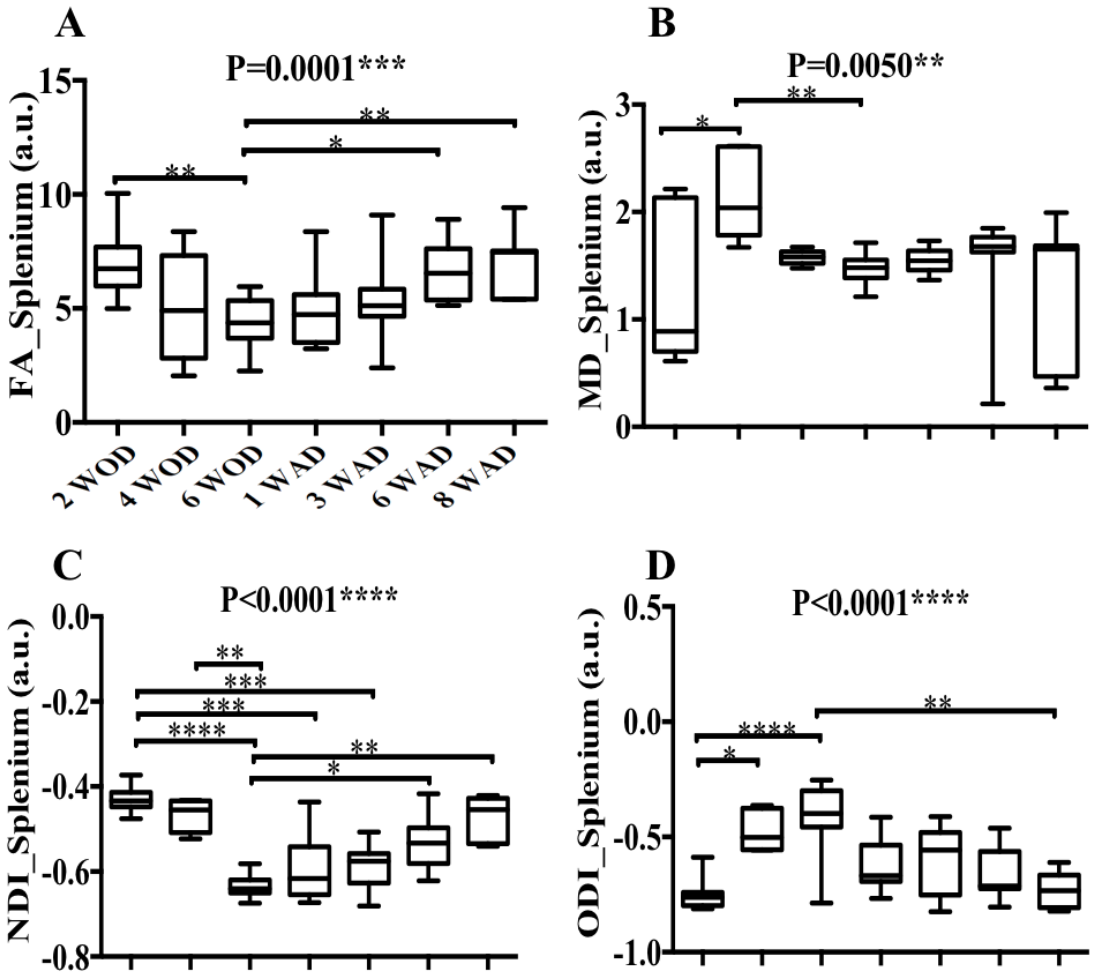

Fig. 3.26: Region-wise changes in MRI on splenium. DWI metrics over time detected significant changes over multiple time points in FA (A), MD (B), NDI (C), and ODI (D).

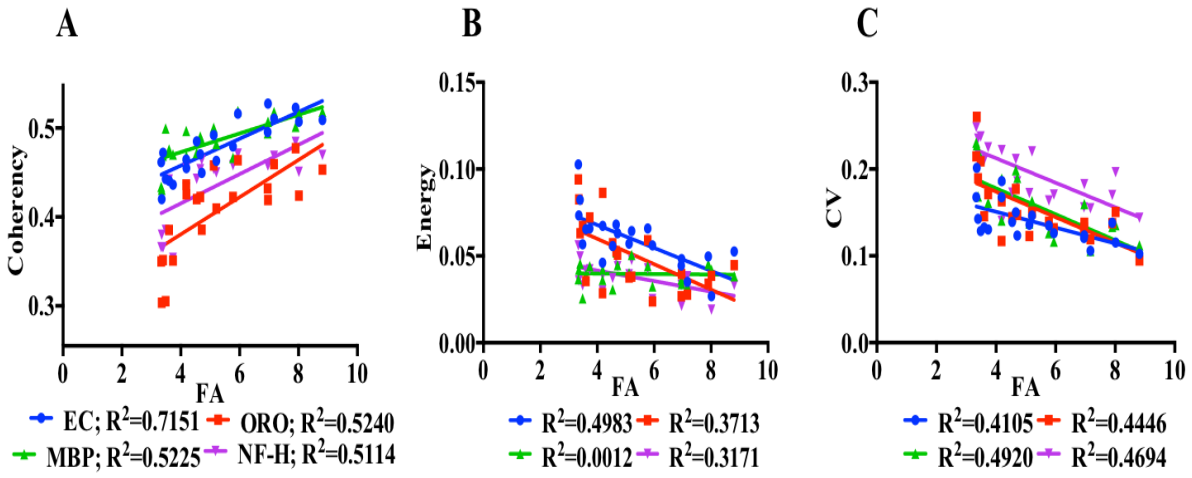

Fig. 3.27: FA correlation with histology structure tensor maps. Linear regression of FA showed strong correlation with histology structure tensor EC coherency map (A), moderate to low correlation with energy maps (B), and circular variance maps (C).

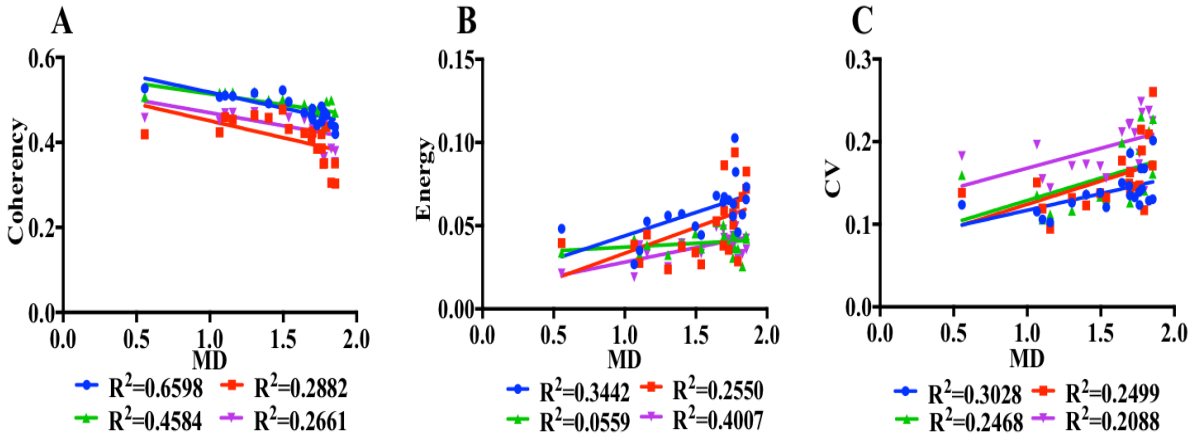

Fig. 3.28: MD correlation with histology structure tensor maps. Linear regression of MD showed strong correlation with histology structure tensor EC coherency map (A), moderate to low correlation with energy maps (B), and circular variance maps (C).

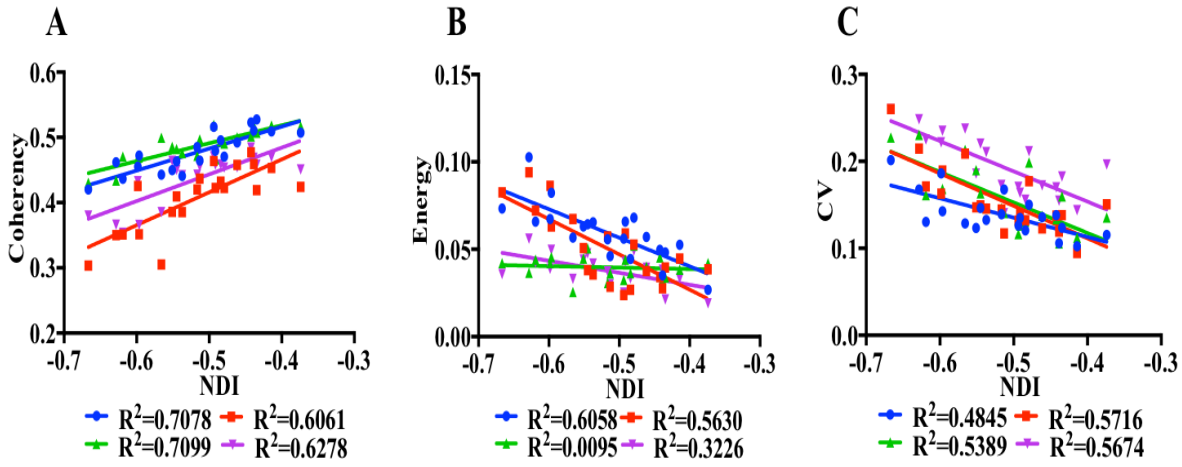

Fig. 3.29: NDI correlation with histology structure tensor maps. Linear regression of NDI showed strong correlation with histology structure tensor EC and MBP coherency maps (A), energy maps (B), and moderate correlation with circular variance myelin maps (C).

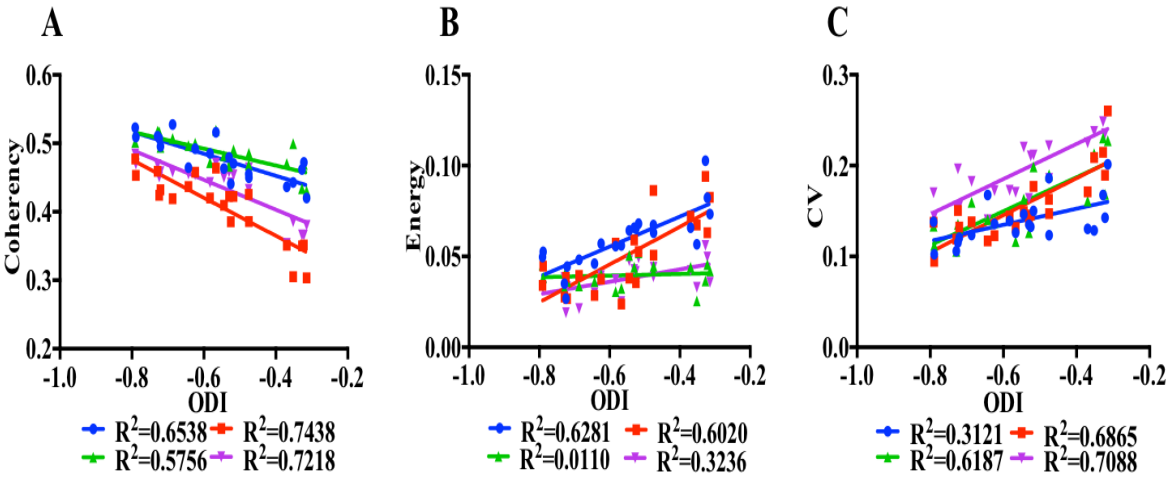

Fig. 3.30: ODI correlation with histology structure tensor maps. Linear regression of ODI showed strong correlation with histology structure tensor NF-H coherency map (A), moderate correlation with energy maps (B), and strong correlation with circular variance axon map (C).

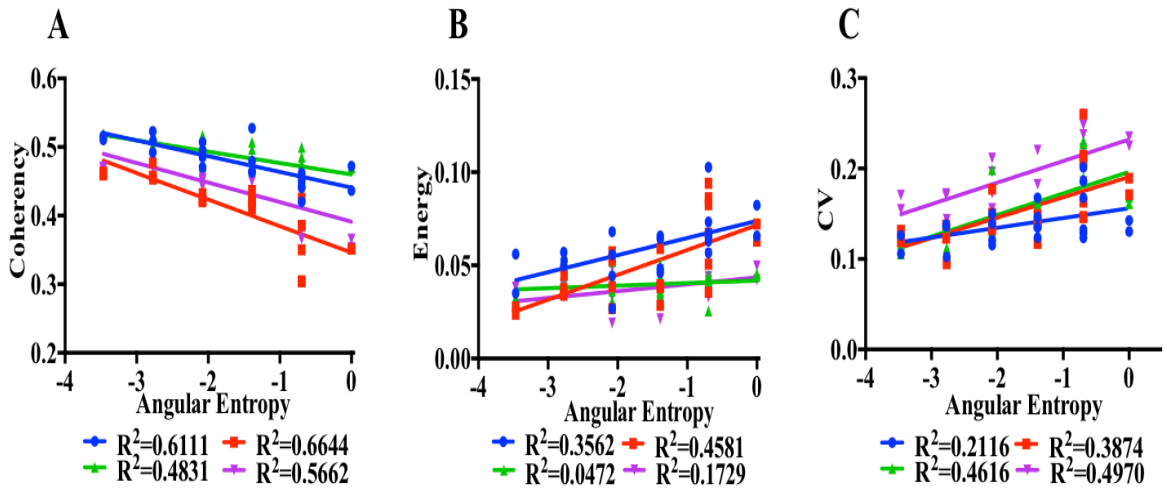

Fig. 3.31: Angular entropy correlation with histology structure tensor maps. Linear regression of angular entropy showed strong correlation with histology structure tensor ORO coherency map (A), moderate correlation with energy (B), and circular variance myelin debris map (C).

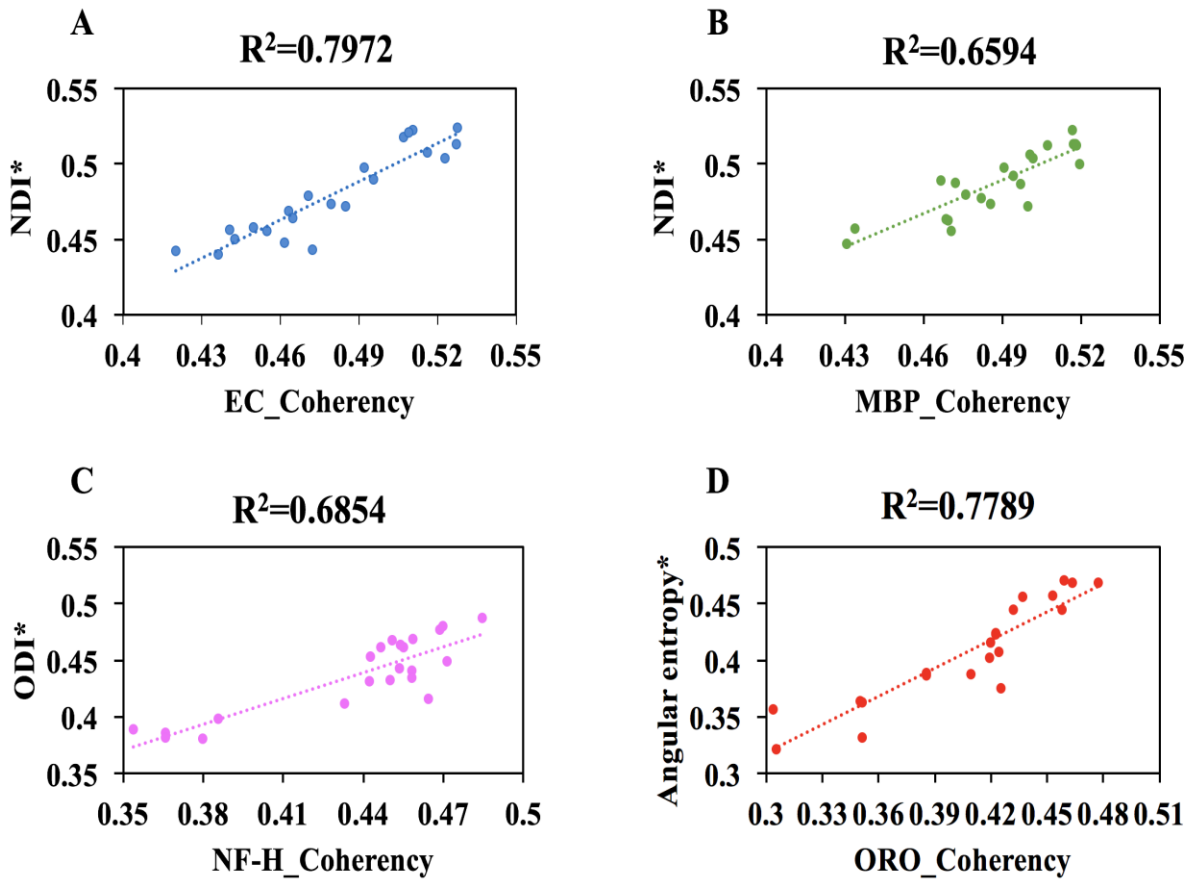

Fig. 3.32: Multivariate logistic regression of MRI metrics with histology structure tensor coherency maps. After exhaustive multivariate regression of all MRI metrics with every possible permutation in coherency maps, NDI showed strongest mean rank to myelin specific EC (A) and MBP (B) maps, ODI showed strongest mean rank to axon specific NF-H (C) map, and angular entropy showed strongest mean rank to myelin debris specific ORO (D) map.

3.3.5 Histology Structure Tensor Maps Complemented MRI on Region-Wise Analysis

Region-wise analysis of the corpus callosum using structure tensor maps in histology showed trends consistent with MRI. The mapping results showed significant changes ($p \leq 0.05$) over multiple time points for the genu, body, and splenium but the graphical observation of coherency and circular variance showed more pronounced changes than energy in the region-wise maps (Fig.

3.12, 3.13, 3.14, 3.16, 3.17, 3.18, 3.20, 3.21, 3.22). Coherency values gradually decreased in all the corpus callosum regions while on cuprizone diet. On the EC map, there was a $(23 \pm 7)\%$ decrease in the genu between week 2 to week 6 on diet ($p<0.05$). The body and splenium coherency maps showed a similar trend as compared to the genu between the same time point but did not achieve significance ($p>0.05$) (Fig. 3.12A, 3.13A, 3.14A). Coherency maps progressively increased after cessation of cuprizone from diet. The splenium had a $(12 \pm 9)\%$ increase at 8 weeks after diet compared to week 6 on diet and was statistically significant ($p<0.05$) whereas the genu and body showed increases within the same remyelination time point but did not prove statistically significant ($p>0.05$) (Fig. 3.12A, 3.13A, 3.14A). Moreover, the ORO ($p>0.05$) and NF-H coherency maps ($p<0.05$) decreased over week 2 to week 6 on cuprizone diet and increased from week 6 on diet to 8 weeks after diet ($p<0.01$) (Fig. 3.12B, 3.13B, 3.14B, 3.12D, 3.13D, 3.14D). MBP coherency maps also showed a similar trend in remyelination time points across regions but did not achieve significant changes ($p>0.05$).

Energy gradually increased in all the corpus callosum regions while on cuprizone diet and decreased after removal of cuprizone from diet but the changes were lesser than those seen in coherency and circular variance maps. The splenium EC energy map showed a significant difference between week 2 on diet to 1 week after diet and was statistically significant $(141 \pm 26)\%$ ($p<0.05$) (Fig. 3.16A, 3.17A, 3.18A). The ORO energy map showed an average $(442 \pm 67)\%$ increase from week 2 to week 6 on diet. The body and splenium ORO energy maps showed a similar trend as compared to the genu ORO energy map between the same time point but did not achieve statistical significance ($p>0.05$) (Fig. 3.16B, 3.17B, 3.18B). NF-H energy in the body and splenium increased by $(133 \pm 27)\%$ and $(117 \pm 19)\%$ respectively between week 6 on diet to 8 weeks after diet and showed statistical significance ($p<0.05$) whereas genu energy showed a

similar trend over the same time period but the changes were not statistically significant ($p>0.05$) (Fig. 3.16D, 3.17D, 3.18D). MBP energy values progressively increased in all the corpus callosum regions on cuprizone diet and decreased after removal of cuprizone from diet but did not achieve statistical significance ($p>0.05$) (Fig. 3.16C, 3.17C, 3.18C).

Circular variance gradually increased in all the corpus callosum regions while on the cuprizone diet and decreased progressively after cessation of cuprizone from diet but did not achieve statistical significance ($p>0.05$) in either EC or ORO over any time points (Fig. 3.20A, 3.21A, 3.22A, 3.20B, 3.21B, 3.22B). The genu showed a significant difference in both the MBP (39 ± 18)% and NF-H (22 ± 6)% maps at remyelination time points between 1 week to 8 weeks after diet whereas the splenium (37 ± 11)% only showed significant changes ($p<0.05$) at remyelination time points from week 6 on diet to 8 weeks after diet in NF-H circular variance map whereas the genu and body showed a similar trend but neither was statistically significant ($p>0.05$) (Fig. 3.20D, 3.21D, 3.22D).

3.3.6 NODDI Metrics Appeared to be More Specific to Pathological Changes than DTI Metrics

Linear regression was performed to determine the correlations between MRI and histology structure tensor analysis metrics. FA strongly correlated to EC coherency maps ($R2=0.7151$) whereas moderately correlated ($R2= 0.51 - 0.52$) to other coherency maps (Fig. 3.27A). MD also strongly correlated to EC coherency maps ($R2=0.6598$) whereas it had a low to moderate correlation to other coherency maps ($R2= 0.27 - 0.46$) (Fig. 3.28A). Angular entropy showed a strong correlation with ORO ($R2=0.6644$) and EC ($R2=0.6111$) coherency maps and a smaller, though still moderate correlation to the other coherency maps ($R2= 0.48 - 0.57$). NDI showed strong correlation with all the coherency maps, MBP ($R2=0.7099$) and EC ($R2=0.7078$) to be the strongest. ODI showed strong correlation with all the coherency maps, ORO ($R2=0.7438$) and NF-

H (R2=0.7218) to be the strongest, except for the moderate correlation with MBP coherency maps (R2=0.5756) (Fig. 3.30A). Correlation of MRI metrics with histology energy maps showed low correlation except for the ODI and NDI which correlated moderately to strongly with EC and ORO energy maps. EC energy map strongly correlated to NDI (R2=0.6058) as did ODI to ORO energy maps (R2=0.6020) (Fig. 3.29B, 3.30B). Angular entropy correlated relatively strongly to ORO stained coherency, energy, and circular variance maps compared to the DTI metrics FA and MD. ODI strongly correlated to NF-H (R2=0.7068) and ORO (R2=0.6865) circular variance maps whereas NDI and FA moderately correlated to all the circular variance maps, NDI ((R2= 0.48 - 0.57) correlated strongly than FA (R2= 0.41 - 0.49) (Fig. 3.27C, 3.29C, 3.30C).

Multivariate logistic regression with exhaustive search of MRI metrics with histology structure tensor coherency maps of myelin, axons, and myelin debris stained images was tested. Regression analysis revealed ranking of MRI metrics to pathological changes and picked the MRI metric with the largest F value in ANOVA. EC coherency as a measure of myelin was best predicted with NODDI metric NDI (F=74.50) ($p=2.04e^{-07}$) (Fig. 3.32A). MBP coherency as another measure of myelin also was best predicted with NDI (F=44.68) ($p=5.25e^{-06}$) (Fig. 3.32B). NF-H coherency as a measure of axon changes was best predicted with NODDI metric ODI (F=47.57) ($p=3.59e^{-06}$) (Fig. 3.32C); myelin debris specific staining ORO coherency was best predicted with texture angular entropy (F=47.55) ($p=5.10e^{-06}$) (Fig. 3.32D).

3.4 Discussion

Using a well-recognized cuprizone mouse model of MS, this study supported the proof of concept of the utility of several advanced MRI measures for assessing structural changes following de- and remyelination with both visual and quantitative histological outcomes. With a focus on the corpus callosum of mouse brain, all imaging measures showed a consistent trend with essentially

worsening during demyelinating and improving over remyelinating periods, consistent with histological observations in myelin, axons, and myelin debris staining. The NODDI metrics NDI and ODI and MRI texture angular entropy, in particular, appeared to be more sensitive to the structural changes than FA and MD from DTI. Moreover, the genu of corpus callosum seemed to change considerably and early both over de- and remyelination; in contrast, the splenium showed avid demyelination and early remyelination in most MRI measures, but the latter was not significant until 8 weeks after stopping of cuprizone diet, which was best detected by NDI. Almost all MRI metrics showed high sensitivity to demyelination in each region of the corpus callosum and remyelination in the genu, but NDI appeared to be the only measure sensitive to both de- and remyelination, including that in the splenium. In histology, tissue coherency from structure tensor analysis showed the best potential in validating the associated MRI measures, but the histology metrics, in general, were not as sensitive as MRI ones in detecting region-wise changes.

Precise measurement of tissue injury and repair in humans represents a long-term challenge in MS, largely due to the complexity of the pathology, lack of histological means to validate the potential methods, and due to lack of tissue as biopsy are not done routinely[213]. The cuprizone mouse model is widely used and well-known for studying the time course of tissue pathology in MS such as de- and remyelination. This model is ideal because of the multiple advantageous features it holds: 1) minimal inflammation, thereby bypassing the autoimmune component of MS[26,35-37]; 2) rapid onset of de- and remyelination, particularly with the C57BL/6 male mice, unlike other strains of mice[25,34,56,236,237,256]; and 3) well characterized and highly reproducible. Of importance, male mice are typically used in this model as they are reported to be more reliable than female mice with the C57BL/6 strain[63], probably due to loss of estrous cycle and hormonal changes in the latter. However, the same study group in another study found that sex difference

did not impact the reproducibility of this model [240]. Therefore, the sex preference of de- and remyelination in this model deserves further validation.

In this study, all the MRI and histology quantitative measures detected injury as a whole, comprising of both demyelination and axonal injury in the corpus callosum[239]. Initiation of demyelination at week 2, gradual increase in demyelination at week 4, and peak demyelination at week 6 on cuprizone diet are evident from changes in signal intensity over the corpus callosum in MRI metrics of cuprizone-fed mice over demyelination time points (Fig. 3.4, 3.5, 3.6, 3.7, 3.8). Decreasing myelin and axonal staining, and increase in myelin debris in the corpus callosum were also observed over demyelination time points validating our MRI findings. The significant changes in MRI between week 2 to week 4 on cuprizone diet likely indicate early demyelination. Specifically, over the demyelination time points, the NODDI metrics NDI and ODI showed higher sensitivity to demyelination throughout than DTI metrics FA and MD. Reduction in NDI may represent loss of neurite density, and increase in ODI indicate elevated dispersion of nerve fiber tracts[223,257], similar to the texture metric angular entropy. FA decreased as an indicator of overall damage, not to specific pathological changes[183,184]. The same applies to the increase in MD. Remyelination and axonal recovery were observed through increase in FA and NDI, decrease in MD, ODI, and angular entropy after cessation of cuprizone from diet reflecting expected changes over repair and are consistent with the existing literature, although most evidence are based only on 2 time points at weeks3 and 6 at remyelination[210,213]. Over the remyelination time series, DTI and NODDI metrics provide complementary information: NDI and ODI showed significant differences on early remyelination from week 6 on diet to 1 week after diet whereas NDI and FA showed significant differences on late remyelination from week 6 on diet to 8 weeks after diet.

Coherency is considered an indicator of structural regularity of nerve fibers[226]; it decreased on cuprizone diet and increased after removal of cuprizone. In histology structure tensor analysis, coherency maps across all the staining showed the most significant differences during whole corpus callosum analysis compared to the energy and circular variance maps. Coherency results of this study were consistent with the findings of Ansari *et al.*[226] in assessing demyelinating lesions of the spinal cord in a lysolecithin model of MS using EC-stained images. The decreasing trend in EC stained coherency maps in all mice from week 2 to week 6 on cuprizone diet indicated gradual demyelination. This is an expected trend during demyelination, as reported in literature[258]. Coherency maps from ORO as an indirect indicator of demyelination through myelin debris accumulation[25] and NF-H immunostaining for healthy axons together revealed that axons were heavily damaged and demyelinated resulting from the cuprizone diet. Axonal restoration and remyelination occurred after removal of cuprizone from diet. Comparison between week 2 and week 6 on diet in MBP and NF-H coherency maps indicated that demyelination and axonal loss occurred concurrently[259]. This observation agrees with existing findings that axonal damage occurs as a consequence of demyelination[162,259]. Only the NF-H coherency maps could detect a statistically significant increase in coherency from week 6 on diet to 1 week after diet, suggesting restoration of axonal health during early remyelination[45], emphasizing the role of axoglial interplay. Energy maps were not significant over time points in MBP staining. Energy maps showed minimal changes overall and were the least sensitive compared to coherency and circular variance maps. NF-H, EC, and ORO stained energy maps showed relatively higher differences, mainly at remyelination time points.

Circular variance represents the measure of angular variability of nerve fibers. It shows higher values if the clustering of nerve fibers is low indicating tissue dissociation. Circular variance

decreases if the clustering of nerve fibers is higher, indicating conservation of nerve fiber orientation[260]. Higher circular variance in NF-H map over the whole corpus callosum indicated axonal damage on cuprizone diet similar to ODI findings. This finding correlates to spinal cord pathology, as reported by Grussu *et al.*[44]. ORO circular variance from week 2 to week 6 on diet detected significant increase in circular variance, which indicates higher tissue injury due to presence of myelin debris[261].

Compared to control mouse, increased g-ratio in the midline splenium as the examination area of interest in cuprizone-fed animals at 6 weeks and 8 weeks after removal of cuprizone from diet revealed continuing remyelination in mice up to 8 weeks after cessation of cuprizone. The higher g-ratio at 6 weeks after diet indicated relatively lower remyelination than 8 weeks after diet. The g-ratio of Cuprizone-fed mice did not reach control animal g-ratio[236] even 8 weeks after diet, implying thinner myelin wrapping around nerve fibers compared to healthy animal, consistent to our MRI findings showing less than optimal recovery toward healthy mouse findings (data not shown). There was no significant difference between the g-ratio of control mouse and 8 weeks after diet mice at this later stages of remyelination, consistent with existing literature[254].

Region-wise, FA changes were pronounced in the genu and body compared to the splenium. The body showed more significant changes compared to the genu in remyelination time points. Comparative analysis of FA between week 6 on diet and 1 week after diet implied relatively higher repair in the body and splenium than genu. This phenomenon may be attributed to the changes in axon diameter between different regions of corpus callosum. As axons may be preserved during demyelination[45], higher FA values are expected in the large caliber axons of the body and splenium compared to the low caliber axons of the genu.

Changes in NODDI metrics showed a similar region-wise recovery pattern as the whole corpus callosum analysis. NDI was the only parameter that shows the capacity to detect both de- and remyelination associated changes, and across all corpus callosum regions. NDI was greater in the genu and splenium than the body at both week 4 and week 6 compared to week 2 demyelination time point. Specifically, it was the highest in the genu at week 4 on diet, indicating early demyelination wherein probably due to small caliber axons with higher density. Changes from week 4 to week 6 on diet showed higher decrease in NDI and increase in ODI indicating injury in the splenium compared to the other two regions, suggesting significant myelin and axonal damage in the splenium at later stages of cuprizone intoxication. It can also be said that demyelination began early at week 4 on diet compared to week 2 on diet in small caliber axons such as those present in the genu[233], and initiated relatively late in areas with large caliber axons such as the splenium and finally, the body[234]. Repair of axonal damage and remyelination as indicated by an increase in NDI values was observed in all the corpus callosum regions after replacing cuprizone with a normal diet, but this change was not evident in other MRI outcomes. Moreover, NDI was higher in the genu and splenium when comparing week 6 on diet to 1 week after diet, implying early, higher recovery than the body. In fact, at late remyelination time points in the splenium, NDI changes were greater, indicating relatively higher recovery in this structure. It can also be said that, remyelination began early in small caliber axons as seen in the genu[233], then large caliber axons in the splenium, and finally in the largest caliber axons of the three in low-density body[262]. Increase in ODI in the genu was higher compared to splenium from week 2 to week 6 on diet indicating higher injury in the former than the latter. A larger decrease in ODI in the splenium and body than the genu from week 6 on diet to 1 week after diet may be attributed to greater axonal repair in the former than the genu. It can also be said that, areas with higher axonal density such

as the genu[263] are more vulnerable to axonal damage due to higher orientational variability compared to areas with relatively sparse axonal density such as those in the body and splenium[235]. The genu also showed a higher degree of myelin damage probably due to the low axonal diameter that are more susceptible to damage[264]. ODI results were consistent with the NDI findings and both NODDI metrics were in agreement to FA results at remyelination time points.

Upon region-wise analysis of the corpus callosum in histology, the quantitative metrics from structure tensor analysis did not show as much significance as seen with the MRI measures. The most prominent changes were seen with the EC coherency maps showing a higher degree of demyelination in the genu compared to body and splenium, consistent with the MRI findings of this study. The EC coherency maps also implied that remyelination from week 6 on diet to 8 weeks after diet in the splenium was significant. This can be interpreted as considerable repair in the splenium at remyelination time points validating our MRI results. ORO and NF-H region-wise coherency maps showed significant changes in all the corpus callosum regions from week 6 on diet to 8 weeks after diet, thus confirming changes over remyelination time period. Comparative analysis of the NF-H coherency maps from week 6 on diet to 8 weeks after diet revealed that the body and splenium axonal recovery was higher compared to the genu. Our finding from NF-H may also confirm the theory of relative preservation of axonal health[45] during demyelination. The ORO energy map in the genu showed the highest degree of damage from week 2 to week 6 on diet compared to the body and splenium. This indicates relatively higher demyelination in the genu compared to body and splenium. NF-H energy maps in the body and splenium implied relatively higher axonal change in large caliber axon area compared to the low caliber axons of the genu, indicating preference of axonal damage in the body and splenium first, consistent to our MRI findings. Likewise, the recovery in both MBP and NF-H circular variance maps at remyelination

time points from 1 week to 8 weeks after diet in the genu also confirms repair in this structure. The splenium also showed improvement in NF-H maps from week 6 on diet to 8 week after diet indicating axonal repair corresponding to changes found in ODI and validated our MRI findings.

NDI and ODI correlated strongly with most of the structure tensor analysis maps compared to conventional DTI metrics, indicating high sensitivity of advanced diffusion maps to myelin and axonal pathology[265]. The high sensitivity also applies to the texture measure angular entropy maps compared to DTI. NDI correlated strongly with myelin maps whereas ODI correlated strongly with axon stained structure tensor indices. Similarly, Fukutomi *et al.*[244] recently found that NDI maps were strongly correlated to myelin content in the gray matter. Collective findings suggest that NDI is sensitive to myelin changes in both gray and white matter. Probable explanations for this could be 1) strong correlation of myelin and axonal density[266] and 2) strong correlation of NDI with myelinated axons compared to unmyelinated axons[267]. To be consistent, Grussu *et al.*[44] also showed the sensitivity of NDI to spinal cord myelin. NODDI metric NDI was specific to myelin changes, ODI specific to axons, and texture angular entropy specific to myelin debris even after multivariate logistic regression confirming specificity of advanced MRI metrics to underlying pathological changes in MS.

The study has limitations as the inherent cuprizone mouse model did miss inflammatory changes and autoimmune part of the MS pathology due to its mechanism of action, true complex pathology of MS was not fully covered as seen in humans. But other models such as EAE is also flawed as it cannot truly reflect demyelination or remyelination as precisely as cuprizone model which was the main focus of this study. Thus, cuprizone mouse model was the best suitable candidate for the study. The study also had relatively small sample size at individual time points, partially due to the extended number of time points used in our study. Although small sample sizes

are common in the cuprizone model, it may have caused missing significance and power in some of the findings for some metrics. Nonetheless, we identified a similar trend in MRI on both overall and on the longitudinal mice cohort, suggesting inter-subject differences were small; furthermore, histology metrics at all the time points were matched to the same animals for MRI when assessing correlation, further reducing variability. Colocalization of lesional pathology between MRI and histology was another challenge due to the higher resolution and thinner slice thickness of histology images over MRI, another common concern in this type of studies[210,243]. We matched our histology image resolution with our MRI using ImageJ (NIH, Bethesda, MD, U.S.) and verified our histology and MRI measures with the help of experienced raters in both imaging modalities. We addressed the slice thickness differences between MRI and histology by acquiring multiple histological images over the same region to match MRI slices within animals. Moreover, we did not have week 4 on cuprizone diet histology images to compare to their MRI counterpart due to scheduling complications, which prevented us to image enough mice for histology without sacrificing the longitudinal cohort. However, several other studies have found that histology changes at week 4 on cuprizone diet showed progression of demyelination and axonal damage[238], which goes in line with our MRI findings. Finally, we had only two control mice to compare to the cuprizone-fed mice. Existing literature shows negative control mice not exposed to toxins do not require additional examination as they do not exhibit pathological changes over time[268], consistent with our study. In the future, we seek to validate the role of sex differences in the cuprizone model of MS using advanced MRI measures over extensive time series[240]. We also plan to investigate changes in cortical gray matter with the help of non-invasive measures along with histological validation[256] in this model for better understanding of disease progression.

In summary, we demonstrated that advanced MRI measures such as NODDI and texture

measures can detect de- and remyelination and axonal pathology over time. Region-wise analysis of the corpus callosum provided insight into the mechanisms of early myelin and axonal damage in the genu on cuprizone diet and late repair in the splenium after cuprizone cessation. This implies that the degree and timing of myelin and axonal injury are related to the axonal morphology such as axonal density and diameter. In addition, this study has demonstrated the sensitivity of the NODDI metric, NDI, to both de- and remyelination, in addition to neurite density in brain white matter, suggesting the possibility of NDI being a novel biomarker of myelin pathology contributing to the existing literature and can work as a measure for neuroprotection in remyelination therapies in clinical translational studies. Overall, advanced NODDI and texture measures appear to be more sensitive and informative to MS-like pathology than DTI metrics and may serve as valuable compensatory tools in future human studies focusing on either disease monitoring or treatment development.

3.5. Supplementary Materials

All the supplementary figures are included at the end of the chapter.

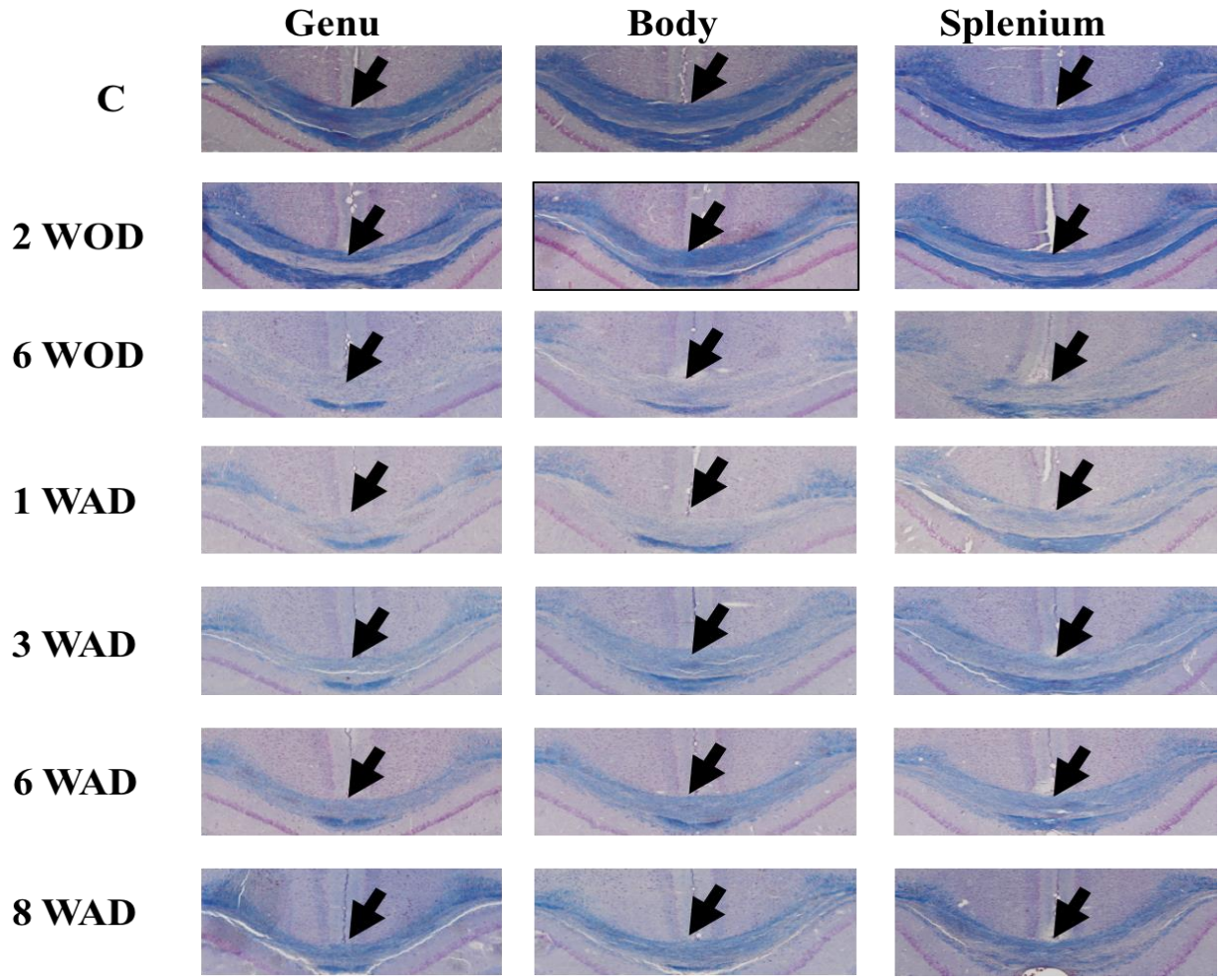

Supp. Fig. 3.1: Region-wise EC stained images. Example EC staining over genu, body, and splenium of corpus callosum over time specific for myelin showing gradual decrease in EC stained area on cuprizone diet and progressive increase in EC stained area after removal of cuprizone from diet (arrowed). Control animal shows uniform uptake of EC staining over corpus callosum (arrowed).

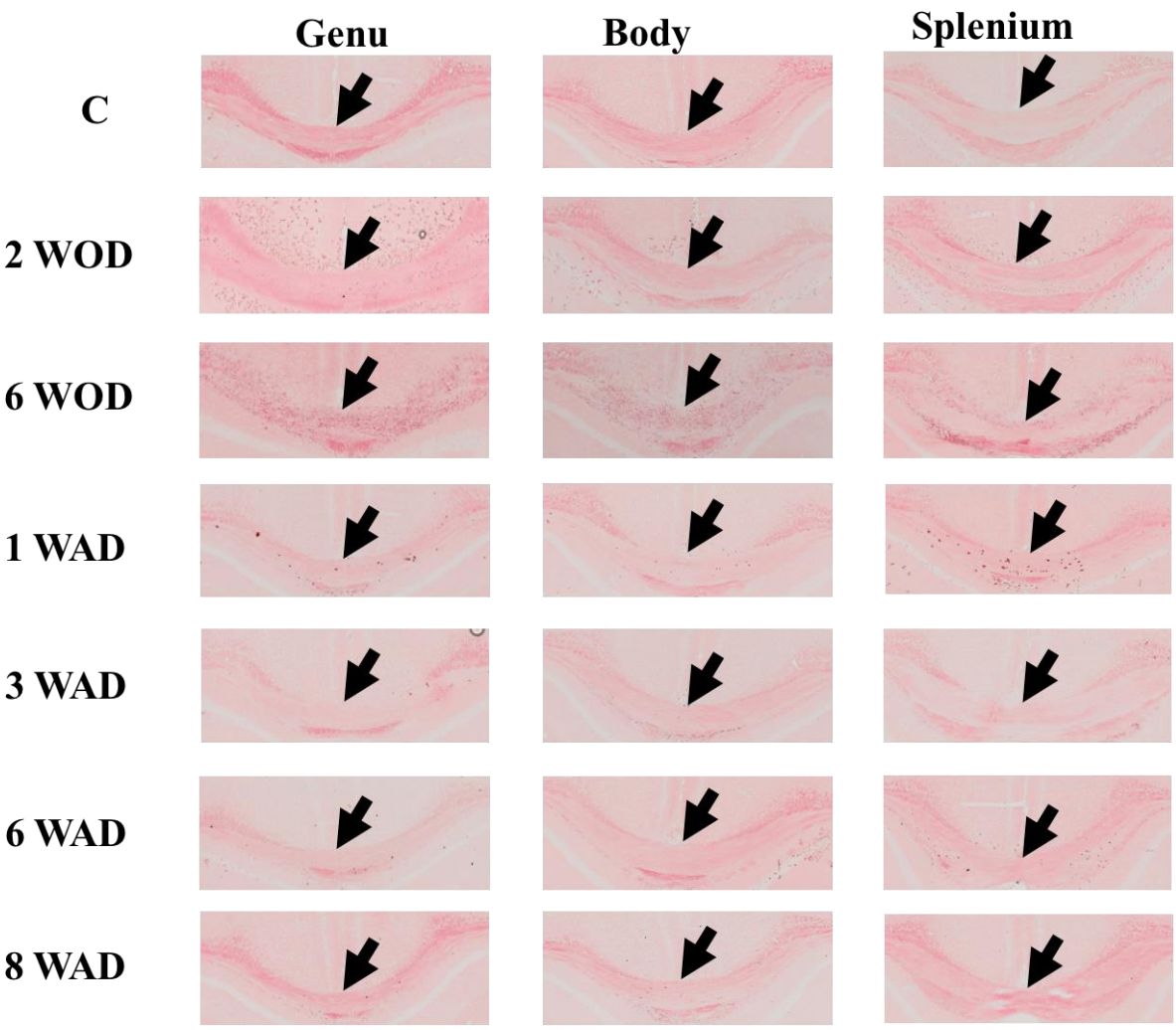

Supp. Fig. 3.2: Region-wise ORO stained images. Example ORO staining over genu, body, and splenium of corpus callosum over time specific for myelin debris showing gradual decrease in ORO stained area with speckle shaped droplets of myelin debris on cuprizone diet and progressive removal of myelin debris after cessation of cuprizone from diet (arrowed). Control animal shows uniform uptake of ORO staining over corpus callosum with no droplets of myelin debris (arrowed).

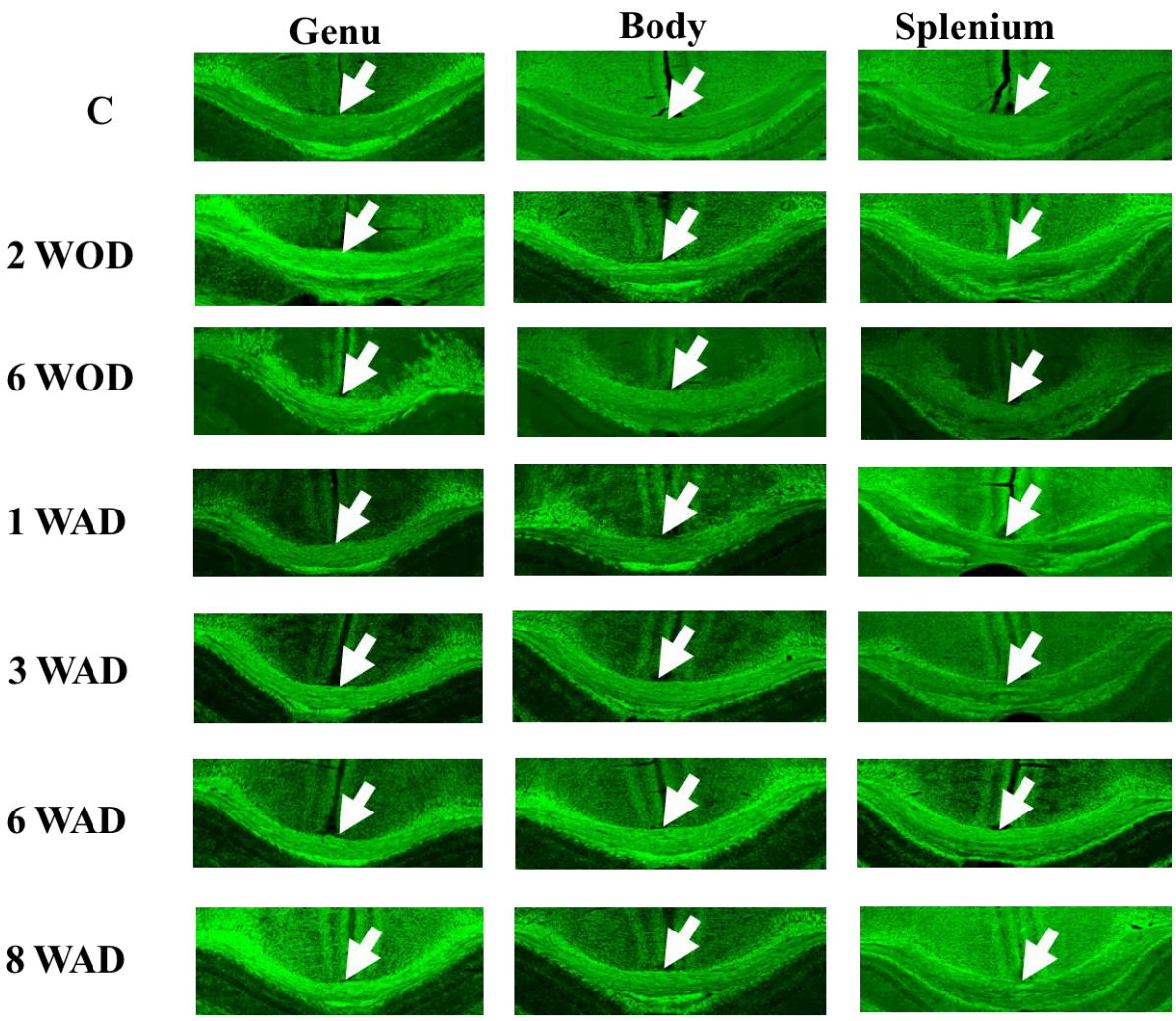

Supp. Fig. 3.3: Region-wise MBP stained images. Example MBP staining over genu, body, and splenium of corpus callosum over time specific for myelin showing gradual decrease and irregularity in MBP stained area on cuprizone diet and progressive increase and restoration of regularity in MBP stained area after removal of cuprizone from diet (arrowed). Control animal shows uniform uptake of MBP staining over corpus callosum (arrowed).

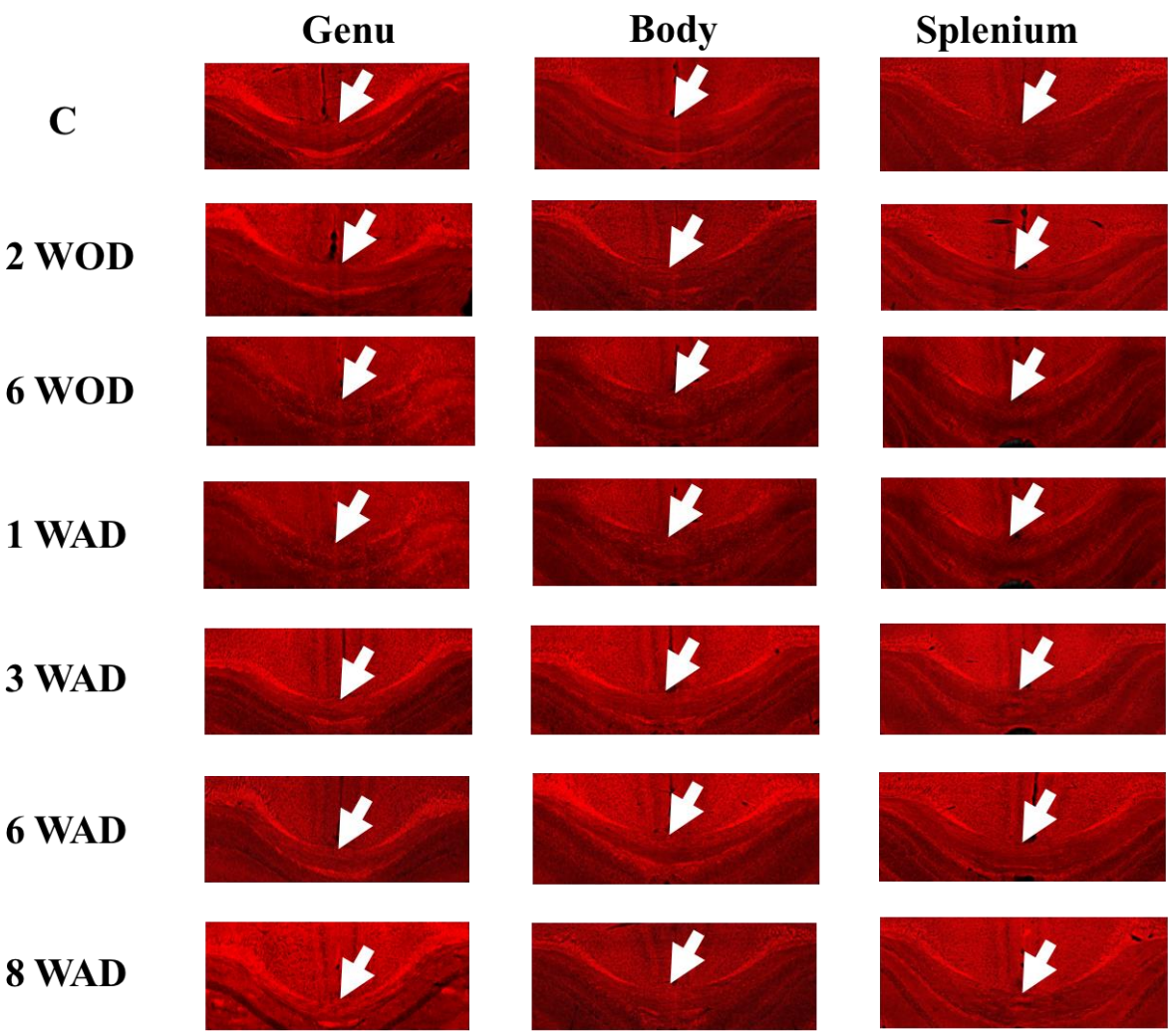

Supp. Fig. 3.4: Region-wise NF-H stained images. Example NF-H staining over genu, body, and splenium of corpus callosum specific for healthy axons over time showing gradual decrease in NF-H stained area on cuprizone diet and progressive increase in NF-H stained area after removal of cuprizone from diet (arrowed). Control animal shows uniform uptake of NF-H staining over corpus callosum (arrowed).

CHAPTER 4

Longitudinal advanced MRI analysis of the optic nerves in patients with acute optic neuritis as a clinically isolated syndrome of MS

As shown in chapter 3, MRI diffusion and texture metrics hold considerable promise to measure structural changes in nerve fiber tracts following a demyelinating insult. ON is one of the most common clinically isolated syndromes (CIS) of MS, and so it is often used as a model for understanding the consequences of inflammatory demyelination in the CNS. This chapter will investigate how advanced MRI measures evaluated and found to be highly correlated with other MRI metrics and histology in chapter 3 detect structural changes after AON in patients participating in a clinical trial of high dose Vitamin D.

4.1 Introduction

ON is an acute inflammatory disorder that is the presenting event in 20 - 21% of MS patients[38,39]. While ON symptoms often spontaneously recover, tissue injury persists in many patients and there is typically slow background injury to the optic nerves in MS patients throughout the disease course[269]. In AON, spontaneous remyelination is often observed in serial MRI[270] and may take place after resolution of inflammatory demyelination regardless the use of corticosteroids[271,272]. There are several theories postulated about the causation of injury and outcome in ON: a) association of inflammation with axonal loss[5]; b) temporary loss of vision[119] from acute axonal injury resulting from concurrent inflammation and demyelination[273-276]; and c) conservation of structural integrity despite severe demyelination[277]. Therefore, assessing the structural properties of the optic nerve following AON can play a crucial role in understanding the interplay between inflammation, de- and remyelination, and axonal injury occurring in MS[81,278].

Moreover, given the unique anatomical characteristics of the optic nerve, studying ON can also provide insight into the complex structural and functional relationships that occur in MS. The other benefit of studying ON is the rapid time course of injury and recovery which can be quantified using fast, effective clinical measures such as OCT and visual acuity. Studying the structural changes after AON can also provide further insight into the mechanisms of myelin and axonal injury and the structural and functional relationships. Moreover, this calls for precise measurement of structural changes in the optic nerve after the onset of AON.

Imaging of the optic nerve has been an ongoing challenge. Optic nerve imaging suffers from artifacts due to eye and head movement, the relatively small size of the optic nerve, and signal interference from surrounding tissues such as orbital fat, bone, and CSF[103,116]. Many studies have used DTI to study the microstructural changes in the optic nerve in ON. For example, AD correlate with axonal loss at one month after AON[177]. Naismith *et al.*[180] reported that RD can detect breakdown in myelin and axons within the optic nerve following ON after 6 months, and validated their finding with OCT and VEP. However, AD and RD findings are mixed. Wheeler-Kingshott *et al.*[208] showed that AD and RD are sensitive to pathological changes, inherently lacks specificity, and should be interpreted with caution for detecting myelin and axon properties. According to a previous study, MD of ON may also serve as a surrogate marker for axonal disruption[279]. Moreover, FA was reported to be sensitive in detecting tissue structural integrity in the optic nerve and optic radiation[280]; for example, in one study, FA detected structural integrity changes in the optic radiation in healthy controls and was compared to the affected and contralateral optic nerves of MS patients with ON; higher FA was observed in the healthy control optic radiation[181]. But FA is not specific to precise pathological processes.

NODDI can provide metrics that may be more specific to myelin and axonal pathologies following inflammatory injury in the CNS[44,210,243]. The NODDI metric, ODI, has detected neuroaxonal changes in cortical gray matter and is reported to be specific to axonal damage[213]. Grussu F *et al.*[44] reported NDI to be sensitive to spinal cord myelin changes. Fukutomi H *et al.*[244] has recently shown the specificity of NDI to myelin damage in cortical gray matter of MS patients. Our findings in the cuprizone animal model in chapter three of this thesis have also shown NDI to be specific to myelin changes in the corpus callosum. The thesis also showed the specificity of ODI to axonal pathology.

NODDI metrics are often derived using a two-shell diffusion acquisition. However, there is an increasing trend to treat high angular DTI as one-shell NODDI, where promising metrics such as ODI can be reliably derived and can be used for investigating white matter abnormalities[243,281] such as axonal changes. Nonetheless, the use of NODDI metrics in evaluating structural changes in ON is scarce. Likewise, advanced MRI texture measures have shown promise for evaluating myelin and axonal changes associated with ON pathology. Zhang Y. *et al.*[282] detected strong correlations between myelin and axonal density and texture heterogeneity, in lesional and peri-lesional areas of the MS brain. Texture features from spinal cord MRI in MS have detected remyelination that was correlated with myelin changes[221]. Texture measures have also quantified macroscopic lesions in MS patient spinal cords and have showed significant correlation with disability[219], and have distinguished MS lesions from normal-appearing white matter and normal white matter[220]. Moreover, MRI texture heterogeneity measures have detected changes in structural integrity in ON and predicted visual recovery 6 and 12 months following ON[216]. In addition, using the post-mortem brains of MS patients, a recent study by Sharma S. *et al.*[224] confirmed a strong relationship between the texture measure, angular entropy, and myelin and

axonal properties. Angular entropy measures in the animal model of this thesis also showed strong correlation with histologically stained imaging measures of both myelin and axons, with the latter being slightly stronger, in addition to the detection of over time changes.

In this study, using DTI, one-shell NODDI based on DTI and texture angular entropy measures, we evaluated tissue structural changes in the optic nerves of patients who were affected by AON and who were treated with either vitamin D or placebo as part of an ongoing clinical trial. Specifically, we investigated: 1) tissue changes in the affected versus non-affected optic nerve at baseline and 2) the relationship between MRI and clinical measures (vitamin D level, disability score).

4.2 Materials and Methods

4.2.1 Participants

This study is part of an ongoing phase II single centre double-blind, randomized controlled clinical trial of high-dose vitamin D in patients with AON (Fig. 4.1). Specifically, patients with a first episode of unilateral AON within two weeks of symptom onset were eligible. Other inclusion criteria for the patients were: 1) age between 18 and 45 years; 2) no significant medical history (other than ON as a CIS); 3) absence of high-dose vitamin D administration; 4) no MRI contraindications; 5) expanded disability status scale (EDSS) score of 0 - 5.5, and 6) serum vitamin D [25(OH)D] < 80 nmol/L. The EDSS is a measure of clinical disability in MS[283]. It ranges between 0 and 10, indicating no disability and death, respectively. For safety purposes, female participants were required to use a reliable form of contraception during the trial. Participants received treatment of either high-dose vitamin D (5 days of vitamin D 50,000 IU/d followed by 85 days of vitamin D 10,000 IU/d) or placebo (5 days of placebo and then 85 days of vitamin D 4,000 IU/d). Patients using corticosteroids or any medications other than additional vitamin D or calcium

supplementation during the 90-day treatment phase was also considered for inclusion in the study. All patients will have had ophthalmic, MRI, OCT, and neurological examinations at baseline, and again at 12 months following AON. However, this study focused on the MRI component of the study, as the study is ongoing and is not allowed to release post-treatment laboratory data which will remain blinded. At the time of analysis, this trial has recruited 9 patients. Each patient had a baseline MRI of the brain and optic nerves, and two had MRI at 12 months at the completion of the trial. Clinical measures such as EDSS score and baseline serum vitamin D [25(OH)D] level information were available for comparison, but 12-month serum vitamin D level was not available. Study personnel were also not informed about which optic nerve was involved. Ethical approval was obtained from the CHREB, the Conjoint Health Research Ethics Board of the University of Calgary and by Health Canada, written informed consent was obtained from each participant. The study was conducted in accordance with the ethical principles of the Declaration of Helsinki.

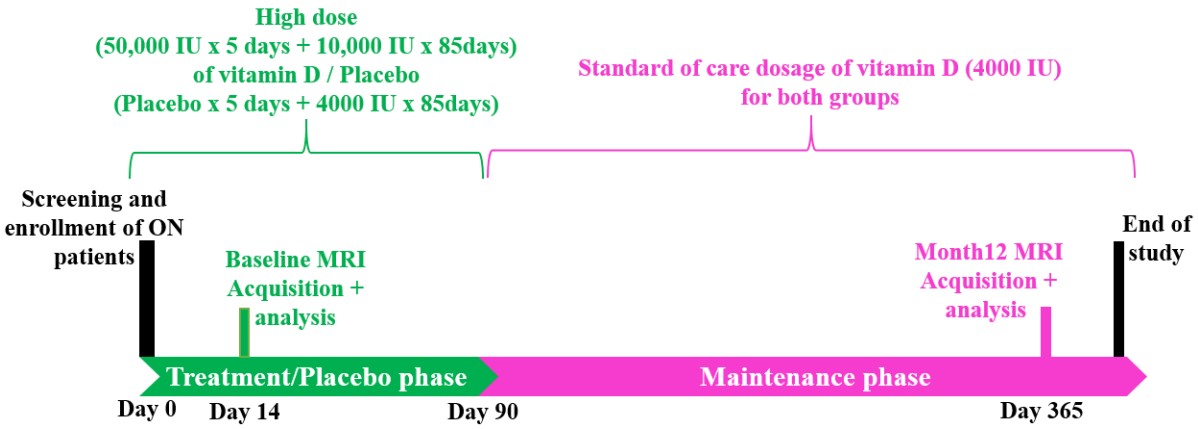

Fig. 4.1: Experimental plan of ON study. Study design for the clinical trial from which all the MRI were obtained at baseline and 12 months thereafter.

4.2.2 MRI Protocol

Patients were imaged using a 3T scanner (Discovery MR750, GE Healthcare, Milwaukee, WI, USA) using optimized optic nerve and brain protocols within 2 weeks of AON and no later than 14 days from treatment initiation. The imaging protocol included: Axial Fast spoiled gradient echo (FSPGR) T1-weighted pre- and 5-min post-contrast sequence [TE/TR = 3/8164 ms, slice thickness = 1 mm, matrix = 256 × 256, pixel size = 1 × 1 mm^2]; axial fast spoiled fast spin echo (FSFSE) T2-weighted sequence [TE/TR = 100/5814 ms, slice thickness = 3 mm, matrix = 512 × 512, pixel size = 0.469 × 0.469 mm^2]; axial multiplanar reconstruction (MPR) double inversion recovery (DIR) sequence [TE/TR = 184.738/7500 ms, slice thickness = 1.2 mm, matrix = 512 × 512, pixel size = 0.6 × 0.6 mm^2]; echo planar imaging (EPI) DTI sequence [TE/TR = 100/5600 ms; slice thickness = 2 mm; matrix = 256 × 256; 30 directions; b value = 1000; 1 b0 volume; pixel size = 0.625 × 0.625 mm^2], with identical settings across all sequences for the FOV, which was 1.6 × 1.6 cm^2 and 2.4 × 2.4 cm^2 for the optic nerve and brain, respectively. A 32-channel head coil was used and participants were instructed to close their eyes to limit movement during the imaging sessions to minimize artifacts. Total image acquisition time per scan was around 60 minutes.

4.2.3 Image Processing

The MRI scans underwent several image processing steps. Manual skull-stripping was done in pre-contrast T1, T2, and diffusion images by removing the surrounding tissues around the optic nerves and skull using ImageJ (NIH, Bethesda, MD, U.S.). Skull-stripping was done to enhance image quality, reliability, and reduce computation time. Manual skull-stripping was done due to the inability of available software such as FSL (FMRIB Software Library, Oxford, UK) to retain the optic nerve. Diffusion data were pre-processed using FSL to correct for potential eddy current-induced distortions and subject motion (linear registration tool, FLIRT). The DTI metrics

calculated were FA and MD, using FSL. Based on the DTI data, ODI was also calculated to obtain intra-voxel tissue structural information using an open-source NODDI Matlab toolbox (UCL, England). Only ODI from NODDI was obtained, as our data was equivalent to single shell diffusion data. NODDI is a multi-compartment model and typically uses multi-shell diffusion data to calculate intracellular compartment metric NDI[243]. Hence, NDI could not be obtained.

Diffusion parametric maps generated from DTI and NODDI were co-registered to the pre-contrast T1-weighted images acquired at baseline, to ensure comparability between imaging outcomes. The cross-sectional registration pipeline is illustrated in Fig. 4.2. Available 12-month diffusion maps were again co-registered to their baseline pre-contrast T1, after over-time co-registration of these images, to ensure position alignment between time points. All the aforementioned image registrations were performed using the FLIRT linear registration tool in FSL that transforms images of different datasets in different planes into one coordinate system to achieve spatial alignment without significant data loss[248]. Transformations used during co-registration were either affine (12 degrees of freedom, for cross-sectional registration, as affine transformation preserves points, straight lines, and planes within the homogeneous coordinates in the same time point images as in inter-modal images within the same time points[284,285]) or rigid body (6 degrees of freedom, for longitudinal registration, as rigid body transformation preserves the length by reflections, translations, and rotations to put 2 time point images in the same plane for better comparability[286]). The selected cost function was correlation ratio for inter-modal and normalized correlation for intra-modal registration. The selected interpolation method was sinc with Hanning window options.

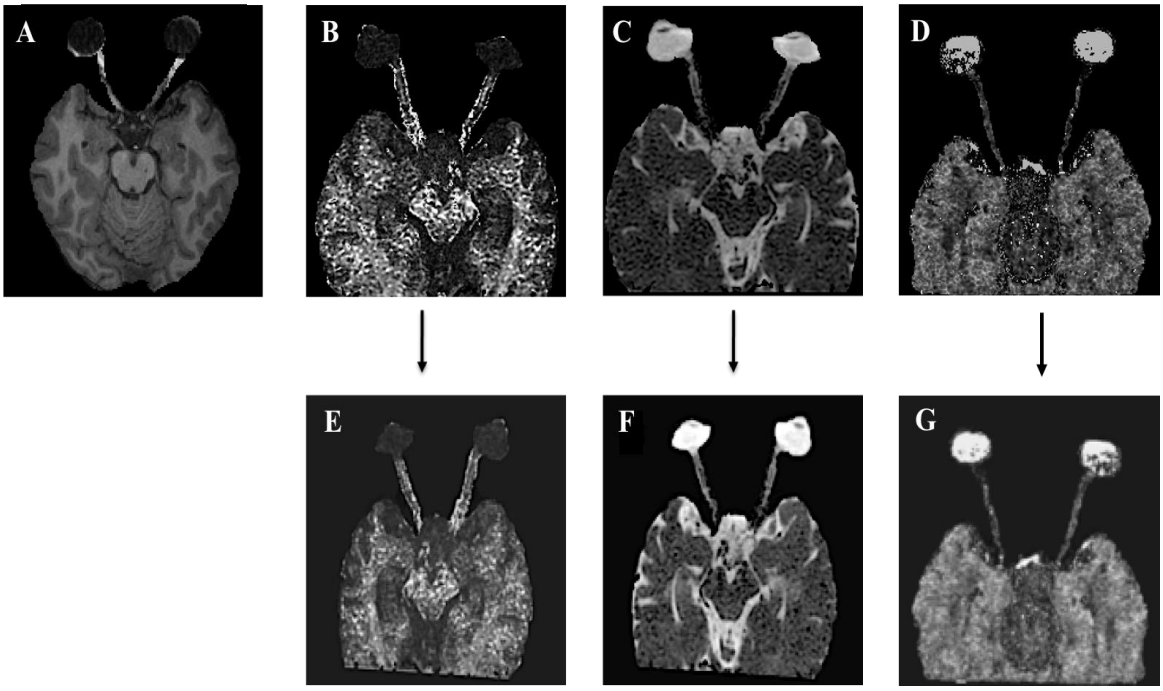

Fig. 4.2: Image registration. Example image registration between different MRI images. Cross-sectional image registration was done for baseline diffusion-weighted images using high-resolution pre-contrast T1-weighted images (A). Raw FA (B), MD (C), ODI (D) maps and registered. Final FA (E), MD (F), ODI (G) maps are shown.

T2-weighted images were used for lesion confirmation as well as texture analysis. The latter was focused on the validated parameter angular entropy from Chapter 3 and our earlier studies[223,224]. Histogram standardization of the masked T2-weighted images was done to reduce intensity variation between time points and to match tissue spatial information[249]. This was done by a standardized procedure implemented in Matlab (Mathworks, Natick, MA, U.S.) prior to image texture quantification. Available 12 months T2-weighted images were co-registered to their baseline T2 prior to longitudinal analysis. This image processing pipeline is illustrated in Fig. 4.3.

Angular entropy calculation used the same method as described in Chapter 3[223]. Essentially, it is a FT power spectrum-based method for assessing the aligning complexity of a tissue structure.

4.2.4 Image Analysis

The imaging metrics from DTI, NODDI, and texture analysis were used to evaluate tissue injury and repair in the affected and contralateral optic nerves after ON. ROIs were drawn by a blind observer manually in the segmented optic nerve over the baseline pre-contrast T1-weighted images, which were then matched to the co-registered diffusion maps. For angular entropy measures, the ROIs were drawn directly over the T2-weighted images. Over each optic nerve, a total of 3 ROIs were drawn to quantify diffusion indices from DTI and NODDI, and 2 ROIs were drawn to quantify angular entropy. The ROIs were carefully selected over the optic nerve to avoid inclusion of the surrounding fat signals to minimize partial volume effects. Afterward, the ROI values from the co-registered DTI parametric maps and texture angular entropy were calculated using ImageJ, and the averaged values from corresponding ROIs were used for quantitative analysis. To understand participant characteristics as an entirety, MRI brain lesions were also evaluated and detection ability was compared between different sequences including T2, post-contrast T1, and DIR, using the lesion volume measurement. DIR has shown an impressive lesion detection ability in previous MS studies, particularly those involving gray matter[287,288].

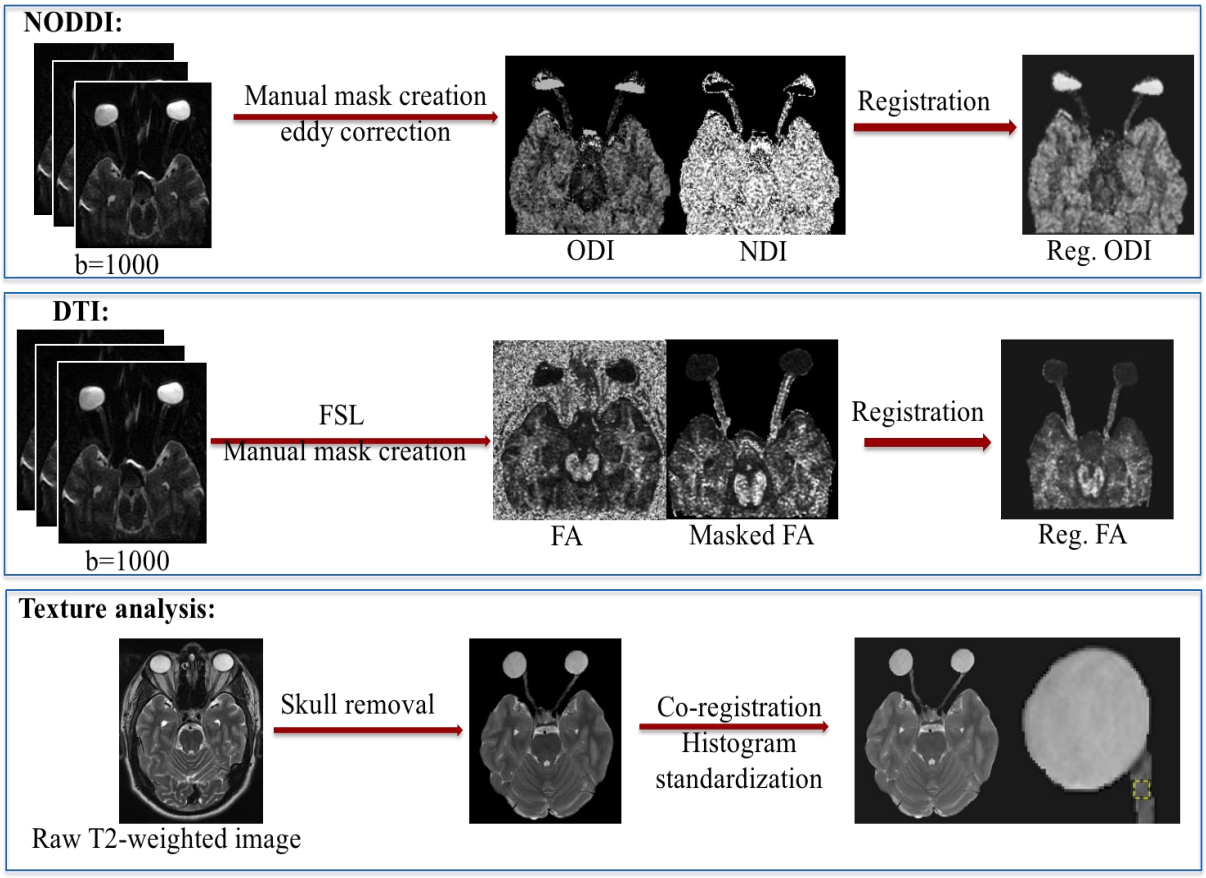

Fig. 4.3: Image processing pipeline. NODDI images were processed to generate an ODI map (top) and DTI were processed for FA and MD maps (middle). All DTI and NODDI metrics were registered to the high-resolution T1-weighted images for spatial alignment and better comparability. High-resolution T2-weighted images were processed for MR texture analysis (bottom).

4.2.5 Statistical Analysis

The analysis focused on both the affected and contralateral optic nerves. Results were expressed as mean ± standard error (SE). Data analysis used average values from different ROIs from the optic nerves. Statistical significance was determined using non-parametric Wilcoxon

paired sign-rank test followed by Holm-Sidak's test to correct for multiple comparisons. Linear regression analysis was done to explore the relationship between MR metrics and clinical measures including serum vitamin D level and EDSS scores, where the coefficient of determination (R^2) was determined. All statistical analyses were performed using GraphPad Prism 6 (GraphPad Software, San Diego, CA, U.S.). A p-value ≤ 0.05 was considered statistically significant and correlation between MR metrics and clinical measures was considered. Correlation between MRI and histology measures was considered low, moderate, and high using linear regression[289].

4.3 Results

4.3.1 Sample Characteristics

Out of the 9 ON patients all had an initial diagnosis of CIS with no MS patients among them, 4 had ON of the right eye and 5 of the left eye. The mean (range) age of all subjects was 27.8 ± 3.7 (21-32) year, six were female; mean EDSS score was 1.67 (0 – 3); serum vitamin D was 37.6 ± 15.9 nmol/L (15.6-61.9 nmol/L). Two patients completed 12 months follow up. Three subjects required high-dose corticosteroid to treat AON; none of them were on disease-modifying therapies; and the degree of visual recovery was rapid (within 3-4 weeks of occurrence) for all patients. Patient demographics for the study are shown in Table 4.1.

Table 4.1: Patient demographics and clinical characteristics at baseline.

Patient ID	Age	Gender	ON	Side of ON	Steroids ? Y/N	Serum vitamin D nmol/L	EDSS
A001	21	F	CIS	R	N	29.1	1
R002	31	M	CIS	L	N	15.6	0
H003	30	M	CIS (MS on MRI)	R	Y	27.6	3
W006	32	F	CIS	R	N	55.9	1
G009	27	F	CIS (MS on MRI)	L	N	61.9	3
D008	24	F	CIS	L	Y	43.9	1
R010	22	F	CIS (MS on MRI)	L	N	55.4	2
S013	28	M	CIS	R	Y	22.9	3
K015	26	F	CIS	L	N	26.5	1

4.3.2 MRI Outcomes at Baseline

All diffusion and texture metrics showed significant difference ($p \leq 0.05$) between affected and contralateral optic nerves. Mean FA (0.30 ± 0.04) was 31% lower in the affected optic nerve than in the contralateral optic nerve (0.43 ± 0.05); ($p=0.004$) (Fig. 4.4A). Mean MD (0.0013 ± 0.0003) was 46% higher in the affected than in the contralateral optic nerve (0.0009 ± 0.0001); ($p=0.0039$) (Fig. 4.4B). ODI was increased 39% in the affected optic nerve (0.24 ± 0.05) relative to the contralateral optic nerve (0.17 ± 0.04); ($p=0.0039$) (Fig. 4.4C). Angular entropy was 66%

higher in the affected optic nerve (-1.14 ± 0.55) compared to the contralateral optic nerve (-3.37 ± 1.30); (p=0.0039) (Fig. 4.4D).

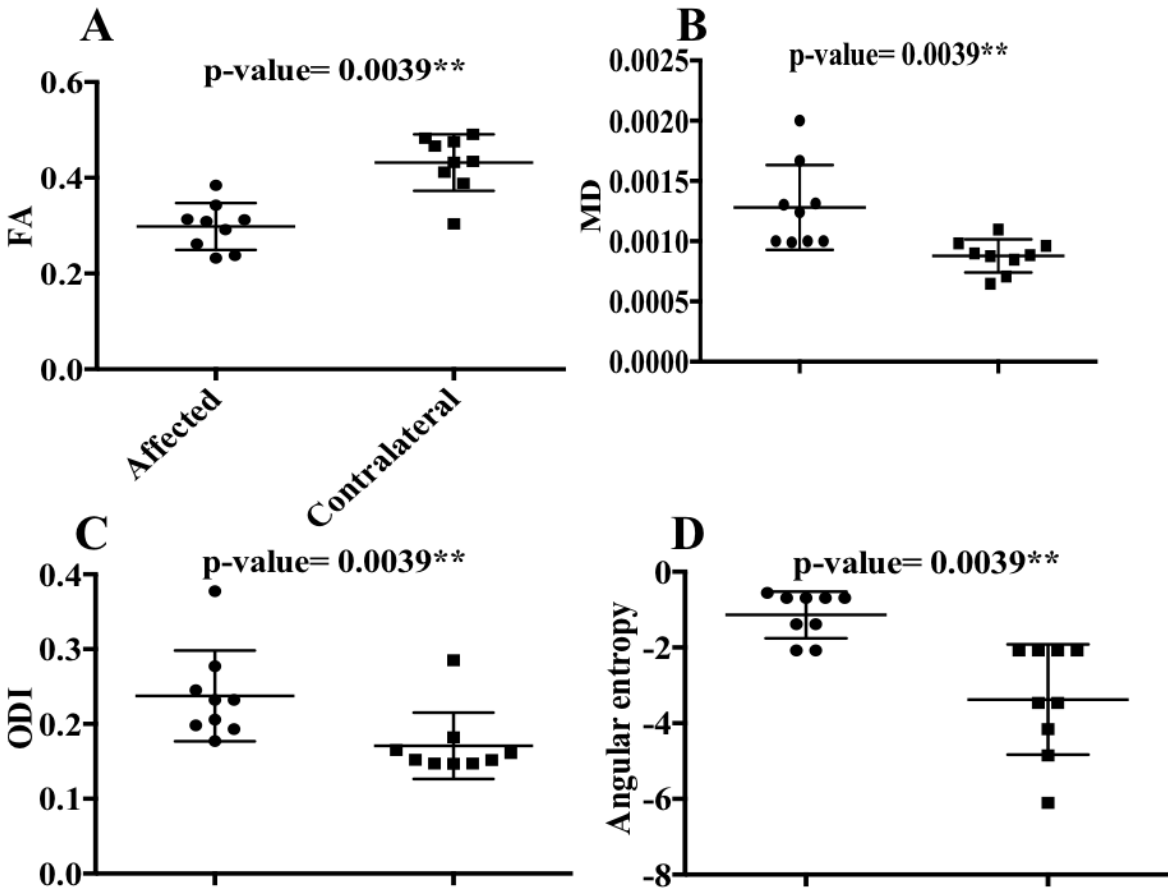

Fig. 4.4: Baseline MR image analysis. Results showed differences in MRI metrics between affected and contralateral optic nerve in DTI imaging metrics FA (A), MD (B), NODDI imaging metrics ODI (C), and texture angular entropy (D).

4.3.3 Longitudinal MRI Outcomes

Mean FA at 12 months' scan in the affected (0.39 ± 0.02) and contralateral optic nerve (0.44 ± 0.05) increased 47% and 3%, respectively, relative to the baseline affected and contralateral optic

nerve. MD at 12 months' decreased 15% and 45%, respectively in the affected (0.0013 ± 0.0) and contralateral (0.0012 ± 0.0002) optic nerve compared to baseline. Mean ODI at 12 months' in the affected (0.20 ± 0.04) and contralateral optic nerve (0.16 ± 0.01) decreased 32% and 25%, respectively, relative to the baseline affected and contralateral optic nerve. Angular entropy at 12 months' decreased 7% and 6%, respectively, in the affected (-1.04 ± 1.04) and contralateral (-2.21 ± 0.82) optic nerve relative to baseline.

4.3.4 The Relationship Between MRI and Clinical Measures

Linear regression was performed between MRI metrics and clinical measures serum vitamin D at baseline and EDSS at baseline. EDSS score was correlated with angular entropy (R^2=0.13; p-value=0.33), and no significant correlations were observed for any DTI metrics (Fig. 4.5A). ODI (R^2=0.36; p-value=0.09) and angular entropy (R^2=0.20; p-value=0.23) showed a negative trend in relation to the increase in serum vitamin D level. There were no other significant correlations between DTI and vitamin D measures (Fig. 4.5B).

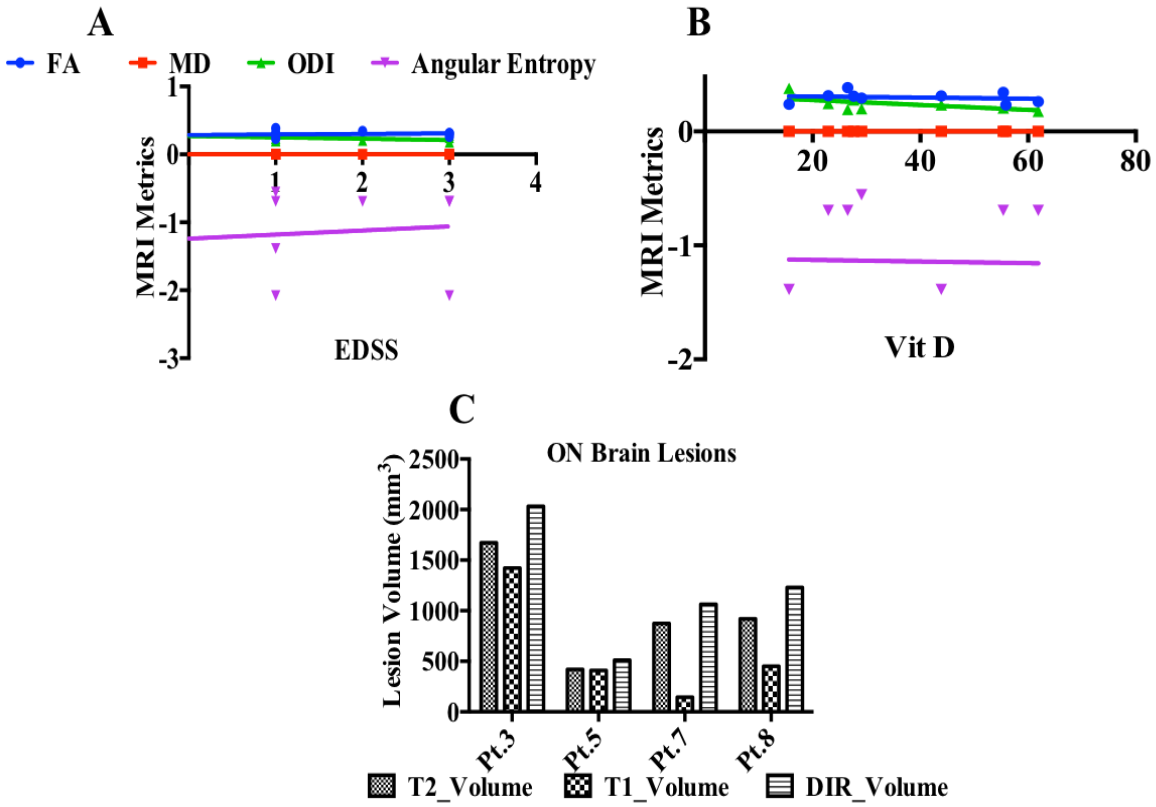

Fig. 4.5: Correlation of MRI metrics with clinical outcomes and brain lesion volume analysis. Linear regression results for MRI metrics showing correlation with clinical measures EDSS (A), Vitamin D (B) at baseline. Baseline brain lesion volumes showed lesion volume detection on different MRI sequences (C).

4.3.5 Brain MRI Lesion Outcomes in the ON Patients

Brain lesions were detected in 4 ON patients in axial T2, DIR, and post-contrast T1 sequences. The number of brain lesions per patient ranged from 4, seen with both T2 and post-contrast T1 sequences, to 58 detected with DIR. Patients showed non-enhancing lesions in post-

contrast T1 images, none of the patients had enhancing lesions. Lesions less than 3 voxels in diameter were excluded from the lesion volume analysis to avoid partial volume effects. The DIR sequence detected the most lesion volume across all the patients (Fig. 4.5C) and served as a reference to identify lesions with subtle signal abnormalities in other two sequences. DIR is the only one that clearly detected the presence of a gray matter lesion in one patient. DIR detected additional lesions in two other patients not evident in the T2 and post-contrast T1 sequences. All patients showing lesions in the brain had relatively higher EDSS score 2.75 (2 – 3), compared to rest of patients 0.71 (0 – 1) (Table 4.2).

Table 4.2: Brain lesion volume in ON patients for different MRI modalities. All lesion volumes are in mm^3.

Patient ID	**T2 Lesions (in mm^3)**	**T1 Lesions (in mm^3)**	**DIR Lesions (in mm^3)**	**EDSS**
H003	1673	1422	2033	3
G009	421	410	511	3
R010	874	144	1063	2
S013	920	451	1230	3

4.4. Discussion

In this study, we detected loss of structural integrity of the affected optic nerve relative to the non-affected contralateral optic nerve, as a result of neuroaxonal damage at baseline and relative recovery at 12 months following either high dose vitamin D or placebo, as determined by MRI diffusion and texture metrics. The NODDI metric ODI and texture measure angular entropy

correlated relatively better with clinical measures compared to DTI metrics. The DIR sequence outperformed T2 and post-contrast T1 sequences in detecting gray matter abnormalities. The fact that angular entropy as a relatively new measure of structural integrity of axons detected pathological changes in a longitudinal patient deserves further validation.

Two-thirds of our ON patients were female. Several other studies have also reported higher prevalence of ON in females than males[29,290]. All patients were young adults, and serum vitamin D was relatively low. Deficits in serum vitamin D in ON and MS patients have been reported in a number of studies and is thought to play a contributing factor to the progression of disease[10,291,292]. As changes in white matter hyperintensities on T2-weighted images are strongly associated with the level of serum vitamin D[293], it is expected that level of serum vitamin D will be associated with changes in structural integrity but this needs confirmation in future studies.

This study detected robust structural differences between affected and contralateral optic nerves. Our finding of decreased FA in the affected optic nerve is in line with the existing literature[178,294]. MD was higher in the affected optic nerve compared to the contralateral optic nerve at baseline indicating higher neuroinflammation as a result of loss of structural integrity, as seen previously[178,279]. ODI is an indicator of loss of orientational directionality of axonal nerve fibers[210]. Higher ODI in the affected optic nerve at baseline may indicate greater dispersion of nerve fibers. NODDI metrics have not been investigated in ON patients, but ODI in other white matter structures such as spinal cord and brain shared similar trends of increase in dispersion of myelinated axons in lesions compared to healthy tissue[210,211]. Texture measure angular entropy is an indicator of coherency and alignment of axonal nerve fibers[223]. Angular entropy was higher in the affected optic nerve compared to non-affected optic nerve at baseline, likely indicating alterations in axonal

pathology, as evidenced in other studies[224,245]. Multiple ROIs were drawn over different anatomical locations of optic nerve, as optic nerve regions vary in diameter and degree of injury[295].

Preliminary case studies demonstrated structural changes over time and showed resolution of inflammation and restoration of structural integrity in all MRI metrics. Compared to baseline, mean FA increased in both the affected and contralateral optic nerves at 12 months whereas mean MD, ODI, and angular entropy were decreased at 12 month scan. These longitudinal DTI findings are consistent with existing literature[296,297]. ODI has also been reported to decrease over time in the spinal cord of a mouse model, indicating restoration of the myelin sheath and nerve fiber re-alignment[210], similar to what is found in this study. Ansari MK *et al.*[226] verified using histological images from mouse spinal cord that angular entropy increases with demyelination, suggesting tissue disruption, and decreases in the remyelinated tissue indicating restoration of structural integrity. One patient in this study showed an increase in angular entropy in the affected optic nerve at 12 month scan relative to baseline. Multiple factors may contribute to this additional structural dissociation, including persistence of ON, recurrence of tissue injury, or treatment regimen received. Correlation with clinical outcomes in the future will help determine if directional angular entropy measures can help detect disease progression. Previously, MRI measures of texture heterogeneity were successful in detecting visual recovery following ON[216]. Longitudinal changes were not significant, however. Given the small sample size available for the current study, further validation is necessary.

Linear regression of MRI metrics with serum vitamin D and EDSS at baseline showed better correlation of texture angular entropy with EDSS score and ODI to serum vitamin D, relative to other metrics, none statistically significant. It can also be said that higher structural disorder of

axonal fibers is associated with greater EDSS scores and dispersion of axonal nerve fibers is restored with increase in serum vitamin D level.

The DIR sequence may be helpful in gray matter lesion detection[287] as shown in patient H003 (Table 4.2). The lesions appear very bright and are easy to detect visually, as DIR nullifies the signals from surrounding tissues[287]. It is reasonable to expect that the presence of MRI lesions in the brain at diagnosis are associated with 12-month outcomes in MRI. Strikingly, the patient with higher angular entropy in the affected optic nerve after 12 months also presented with brain lesions in the 12-month DIR scan, which were not visible at baseline in DIR or in the other two lesion detecting sequences. Post-contrast T1 is mostly used to detect active inflammatory lesions and so is not comparable to other sequences for lesion volume measurements[165,298]. The T2 sequence can detect relatively more lesions compared to pre- and post-contrast T1 sequences, and is widely used to identify the number and volume of clinically silent lesions in clinical studies and trials[143,144]. All patients showing lesions in different MRI sequences had higher EDSS score (Table 4.1) compared to others. This is consistent with findings in numerous prior studies, although the correlation coefficient is mostly low to moderate[299-301]. Likewise, the more lesion load in the ON patients may indicate greater damage in the visual pathway[4,146]. Conversely, lesion volume reduction may indicate repair or neuroprotection[126,147,148].

There are several limitations of the study, most notably the low sample size. Nonetheless, the homogeneous study population that only included a CIS cohort of ON was beneficial making up the small sample size. In addition, only single-shell diffusion data was used in this study, and thus, the NODDI metric NDI could not be calculated. As full NODDI fitting requires multi-shell diffusion acquisition, a much higher acquisition time would be required (>10 minutes)[243] making it challenging for optic nerves that are highly susceptible to moving artifacts[103,116], and in a clinical

trial setting where the overall scan duration is limited to 60 minutes. Zhang H *et al.*[243] showed that ODI measures from 1-shell and multi-shell data were similar, and the generation of ODI from one-shell data does not require any special attention. Hence, ODI analysis was reasonable for this study. The study had no control subjects. Even though the contralateral optic nerve did not exhibit any appreciable changes longitudinally, the literature suggests that it may still undergo subtle pathological changes following ON[216,279]. Future work should include a larger sample size with the inclusion of control subjects to allow appropriate comprehensive comparison. An association of MRI metrics with other visual outcomes such as visual acuity LogMAR score can be beneficial to further confirm whether advanced MRI techniques can predict visual outcomes and/or conversion of ON into MS. Moreover, evaluation of structural changes in the afferent visual pathway and visual cortex may also prove beneficial for better understanding of the consequences of ON and for disease mechanisms of MS.

CHAPTER 5

Conclusions

The ability to precisely measure changes in tissue pathophysiology and understand their relationship to patient function has been a long-term goal in the clinical management of MS. As a major component in the disease characterization pipeline, non-invasive imaging approaches based on MRI keep playing a central role in both the clinical and research settings. However, while a variety of conventional and advanced MRI techniques are available, there is still lack of methods that are specific to patient pathology or functional outcomes in MS.

Given the intimate relationship between myelin and axons, MRI methods that have the potential to measure both is desirable. The nerve fiber tracts in brain white matter are highly aligned and directionally coherent, making the movement of water molecules greatly anisotropic in a healthy condition. In theory, any potential changes in the anisotropic properties of tissue will implicate the alteration in structural integrity. The diffusion-based MRI methods are designed to detect such properties in water movement in tissue, especially the newer diffusion MRI techniques that make an intra-voxel assessment of myelin and axonal changes possible. Alternative methods that evaluate the inter-pixel relationships in an image have also shown the utility to measure myelin and axonal properties. Compared to diffusion MRI, such so-called texture analysis methods detect the macroscopic integrity of a structure. MS pathology, however, is unsurprisingly complex. Not only may it occur anywhere in the CNS, several pathological changes can also be present simultaneously within a single lesion. So any potential MRI method should survive systemic validations.

The motivation of this project was to establish new MRI measures of injury and repair such as MRI diffusion and texture metrics using specific models of MS. With a focus on de- and remyelination driven pathology, the first part of the thesis was to test how these measures change over time and how that compares with histology using a cuprizone mouse model of MS. The second part is to test the usefulness of the validated measures in measuring the consequences of inflammatory demyelination in patients with ON, a CIS model of MS.

In this chapter, I will first summarize the key research findings of the thesis. Then I will describe some of the limitations of the research, followed by significance and future directions.

5.1 Summary of key Research findings

The overall goal of the thesis was to test the hypothesis: HARDI-based NODDI and MRI directionality based texture measures can detect structural changes following de- and remyelination over time and can extract more pathology specific information than commonly available advanced MRI. In this regard, NODDI, angular entropy metrics as advanced and DTI metrics as commonly available imaging measures were applied in the two models of MS. The anatomical preference of pathological events associated with de- and remyelination was also tested by using both MRI and histology images in the corpus callosum in the cuprizone model, a well-studied white matter structure with well-known region-specific organization of nerve fibers in both mice and humans[25,223]. The feasibility of using NODDI and texture measure angular entropy in a clinical setting in human ON model was assessed to evaluate the structural integrity of another white matter tract, optic nerve. Therefore, the advanced MRI outcomes have been validated by using different approaches in two specific aims; 1) a toxicant-induced cuprizone mouse model over an extensive time series along with parallel confirmation using histological indices quantified using structure tensor analysis and myelin g-ratio and 2) in a different white matter structure, optic

nerve, in an inflammatory model of MS confirming the robustness of advanced imaging measures in detecting structural changes following the occurrence of acutely demyelinated lesions in the CNS.

Firstly, in the cuprizone mouse model, all the MRI metrics showed expected trends and detected progressive axonal changes associated with de- and remyelination over time. Further analysis was done into the corpus callosum in three anatomically distinct regions genu, body, and splenium to study whether anatomical preference and timing of pathological events varied across regions. Very intriguing results were observed in NODDI metric NDI showing both de- and remyelination began early in the small caliber, densely organized nerve fiber area genu; demyelination was also seen early but repair was noted late in the large caliber, less-packed nerve fiber area splenium. Body with relatively large caliber axons showed intermediate changes in detecting both injury and repair. Since histology measures serve as a gold standard for evaluation of tissue microstructure and are specific to pathological changes in both myelin and axons, the animals were matched over time and quantitative histology structure tensor analysis was conducted. Structure tensor analysis outcomes directly transfer histology measures for MRI to compare, including the region-wise MRI findings. Interestingly, the directionality based histology maps of structural integrity, alignment, and organization for myelin agrees with the advanced MRI findings of this study. Analysis showed earlier remyelination of small caliber axons compared to delayed remyelination in large caliber axons, which was also evident in morphological changes in histology images as measured using myelin g-ratio over time. Moreover, histology measures for axonal staining reinstated the claim that rapid axonal damage is detected in densely packed axonal fibers (genu) compared to loosely packed axonal area (splenium and body). Finally, for aim1, MRI and histology measures were correlated to detect their specificity to underlying pathology. NODDI

metrics NDI and ODI correlated better compared to the conventional DTI metrics indicating their higher specificity to underlying pathology. Surprisingly, NODDI metric NDI correlated strongly with myelin maps implying that NDI is sensitive to myelin and can serve as a potential measure for myelination status.

Second aim of this study focused on another promising model of MS, the optic nerves in ON patients, for further validation of the ability of advanced imaging measures in detecting structural integrity and the utility of these imaging measures in a clinical setting. Affected versus contralateral optic nerves comparison was done with advanced imaging measures and compared with DTI metrics. All the MR imaging metrics identified structural integrity changes in the affected versus contralateral optic nerves at baseline and longitudinally at 12 months scans. The correlation of MRI metrics with clinical measures such as serum vitamin D and EDSS score showed that texture angular entropy correlated best with EDSS scores. ODI showed the strongest correlation with serum vitamin D level compared to other imaging metrics. This finding demonstrates the potential of advanced imaging measures for using in a clinical setting. Lesion volume comparison between clinical MRI sequences revealed the DIR sequence to be better than other T2 or T1 in both white and gray matter lesion detection. Interestingly, all the ON patients with brain lesions had higher EDSS score than those who did not present with lesions. All these findings together validated the aim one and proved the hypothesis of the thesis that advanced imaging measures quantified tissue injury and repair, better predicted pathological changes over time in demyelinating diseases, and has the potential to be used in a clinical setting. However, further validation is warranted.

5.2 Limitations of the Thesis

The overall sample size for the human ON study was small but patient homogeneity for the study made up the small sample size. The sample size for cuprizone mouse model over multiple time points was relatively small due to the extended number of time points designed for a comprehensive understanding of the pathological changes, and the limited imaging time available at the dedicated scanner at some time points. However, histological measures over time helped validate the MRI outcomes further. The ROIs used in the MRI metrics were manually matched to the histology measures due to the much higher image resolution and very thin slice thickness of the histology images. Numerous histology slices were acquired to match the MRI ROI locations and downsizing of histology images helped as well. The use of directly transferrable structure tensor analysis metrics of myelin, myelin debris, and axon stained images also helped improve the accuracy of histological outcomes. Furthermore, both the animal and human models of the study had limited or no true controls to compare healthy status with pathological processes but literature shows that negative control mice not exposed to toxins do not require additional examination as don't exhibit pathological changes over time[268] and unilateral ON patients show negligible pathological changes over non-affected eye[119]. Finally, the ON study did not have multi-shell diffusion data, thus did not have NDI measured due to the time constraint of human imaging to be kept within 60 minutes, and the susceptibility of the optic nerve to moving artifacts. However, literature showed that single-shell diffusion data demonstrated similar findings in ODI compared to multi-shell data[243] and that was explored in this study. Further validation of the findings is necessary.

5.3 Significance of the Research

Potentially, advanced imaging measures can be used in disease progression studies for evaluating diffuse dynamic changes[132] of myelin and axons over time in lesional areas over the course of demyelinating diseases such as MS. De- and remyelination over extensive time series were evaluated in this study instead of only 2 or 3 time points typically done in the literature. Comprehensive investigation in this study also provided a unique opportunity to detect preference of de- and remyelination to different anatomical locations over corpus callosum. This preference of pathological processes was based on their axonal morphology of density and diameter in MS which can be extremely helpful for future translational use in humans. There is always growing need for non-invasive quantitative measures specific to myelin and this study tested the sensitivity of advanced imaging measures in white matter and detected NDI to be specific to myelination status and can serve as a measure for myelin integrity in clinical trials for developing new neuroprotective therapeutics. The study focused on changes over the entire corpus callosum and optic nerves along with focal lesional areas in MS which can prove to be pivotal in understanding tissue injury and repair and processes underlying MS pathology. Arguably, this study is the first to evaluate the feasibility of using advanced diffusion imaging method NODDI in ON patients and suggests the potential of using this measure in clinical studies which may help advance the diagnosis and management of this disease, and MS, with further validation.

5.4 Future Directions

In the future, the role of sex differences can be investigated in the models of MS with the help of advanced imaging measures as sex is thought to play a crucial role in the prevalence of MS and ON. Testing of 3D advanced imaging measures with validated 3D structure tensor analysis can also be explored in the future to confirm whether they are able to detect additional pathological

changes or can be true reflections of myelin regularity in comparison to axons. It will be very interesting to see if changes, as seen in white matter in this study, can be reflected in the cortical gray matter as gray matter abnormality is thought to be the major contributing factor to disability in MS patients. Multi-shell diffusion data can be tested in ON or MS patient studies to check the utility of NDI metric in detecting pathological changes specific to neurite pathology and whether able to detect conversion of ON into MS over time. Finally, with further validation using either animal models or post-mortem MS brain samples, monitoring disease evolution in humans in either focal lesions or lesion-free areas can also be investigated for these advanced imaging measures to assess the feasibility of using them routinely in a clinical setting and in future therapeutic intervention evaluations.

References

1. Gilmour H, Ramage-Morin PL, L.Wong S. Multiple sclerosis: Prevalence and impact. Statistics Canada 2018;29:3-8.
2. Noseworthy J, Lucchinetti C, Rodriguez M, Weinshenker B. Multiple Sclerosis. The New England Journal of Medicine 2000;343:938-52.
3. Karampampa K GA, Miltenburger C, Kindundu CM, Selchen DH. Treatment experience, burden, and unmet needs (tribune) in multiple sclerosis study: the costs and utilities of MS patients in Canada. J Popul Ther Clin Pharmacol 2012;19:e11-e25.
4. Palace J. Making the Diagnosis of Multiple Sclerosis. Journal of Neurology, Neurosurgery & Psychiatry 2001;71:ii3--ii8.
5. Dutta R, Trapp BD. Mechanisms of neuronal dysfunction and degeneration in multiple sclerosis. Progress in Neurobiology2011:1-12.
6. Correale J, Gaitan MI, Ysrraelit MC, Fiol MP. Progressive multiple sclerosis: from pathogenic mechanisms to treatment. Brain 2017;140:527-46.
7. Scalfari A, Neuhaus A, Daumer M, Ebers GC, Muraro PA. Age and disability accumulation in multiple sclerosis. Neurology 2011;77:1246-52.
8. Canada: Multiple Sclerosis (MS) Capital of the World. The National Benefit Authority, 2015. (Accessed July 1, 2019, at https://www.thenba.ca/disability-blog/canada-multiple-sclerosis-ms-capital-world/.)
9. McFarland HF, Martin R. Multiple sclerosis: A complicated picture of autoimmunity. Nature Immunology2007:913-9.
10. Burton JM, Costello FE. Vitamin D in multiple sclerosis and central nervous system demyelinating disease--a review. J Neuroophthalmol 2015;35:194-200.
11. Huynh JL, Casaccia P. Epigenetic mechanisms in multiple sclerosis: Implications for pathogenesis and treatment. The Lancet Neurology2013:195-206.
12. International Multiple Sclerosis Genetics C, Wellcome Trust Case Control C, Sawcer S, Hellenthal G, Pirinen M, Spencer CC, Patsopoulos NA, Moutsianas L, Dilthey A, Su Z, Freeman C, Hunt SE, Edkins S, Gray E, Booth DR, Potter SC, Goris A, Band G, Oturai AB, Strange A, Saarela J, Bellenguez C, Fontaine B, Gillman M, Hemmer B, Gwilliam R, Zipp F, Jayakumar A, Martin R, Leslie S, Hawkins S, Giannoulatou E, D'Alfonso S, Blackburn H, Martinelli Boneschi F, Liddle J, Harbo HF, Perez ML, Spurkland A, Waller MJ, Mycko MP, Ricketts M, Comabella M, Hammond N, Kockum I, McCann OT, Ban M, Whittaker P, Kemppinen A, Weston P, Hawkins C, Widaa S, Zajicek J, Dronov S, Robertson N, Bumpstead SJ, Barcellos LF, Ravindrarajah R, Abraham R, Alfredsson L, Ardlie K, Aubin C, Baker A, Baker K, Baranzini SE, Bergamaschi L, Bergamaschi R, Bernstein A, Berthele A, Boggild M, Bradfield JP, Brassat D, Broadley SA, Buck D, Butzkueven H, Capra R, Carroll WM, Cavalla P, Celius EG, Cepok S, Chiavacci R, Clerget-Darpoux F, Clysters K, Comi G, Cossburn M, Cournu-Rebeix I, Cox MB, Cozen W, Cree BA, Cross AH, Cusi D, Daly MJ, Davis E, de Bakker PI, Debouverie M, D'Hooghe M B, Dixon K, Dobosi R, Dubois B, Ellinghaus D, Elovaara I, Esposito F, Fontenille C, Foote S, Franke A, Galimberti D, Ghezzi A, Glessner J, Gomez R, Gout O, Graham C, Grant SF, Guerini FR, Hakonarson H, Hall P, Hamsten A, Hartung HP, Heard RN, Heath S, Hobart J, Hoshi M, Infante-Duarte C, Ingram G, Ingram W, Islam T, Jagodic M, Kabesch M, Kermode AG, Kilpatrick TJ, Kim C, Klopp N, Koivisto K, Larsson M, Lathrop M, Lechner-Scott JS, Leone MA, Leppa V, Liljedahl U, Bomfim IL, Lincoln RR, Link J, Liu J, Lorentzen AR, Lupoli S, Macciardi F, Mack

T, Marriott M, Martinelli V, Mason D, McCauley JL, Mentch F, Mero IL, Mihalova T, Montalban X, Mottershead J, Myhr KM, Naldi P, Ollier W, Page A, Palotie A, Pelletier J, Piccio L, Pickersgill T, Piehl F, Pobywajlo S, Quach HL, Ramsay PP, Reunanen M, Reynolds R, Rioux JD, Rodegher M, Roesner S, Rubio JP, Ruckert IM, Salvetti M, Salvi E, Santaniello A, Schaefer CA, Schreiber S, Schulze C, Scott RJ, Sellebjerg F, Selmaj KW, Sexton D, Shen L, Simms-Acuna B, Skidmore S, Sleiman PM, Smestad C, Sorensen PS, Sondergaard HB, Stankovich J, Strange RC, Sulonen AM, Sundqvist E, Syvanen AC, Taddeo F, Taylor B, Blackwell JM, Tienari P, Bramon E, Tourbah A, Brown MA, Tronczynska E, Casas JP, Tubridy N, Corvin A, Vickery J, Jankowski J, Villoslada P, Markus HS, Wang K, Mathew CG, Wason J, Palmer CN, Wichmann HE, Plomin R, Willoughby E, Rautanen A, Winkelmann J, Wittig M, Trembath RC, Yaouanq J, Viswanathan AC, Zhang H, Wood NW, Zuvich R, Deloukas P, Langford C, Duncanson A, Oksenberg JR, Pericak-Vance MA, Haines JL, Olsson T, Hillert J, Ivinson AJ, De Jager PL, Peltonen L, Stewart GJ, Hafler DA, Hauser SL, McVean G, Donnelly P, Compston A. Genetic risk and a primary role for cell-mediated immune mechanisms in multiple sclerosis. Nature 2011;476:214-9.

13. Cree BA. Multiple sclerosis genetics. Handb Clin Neurol 2014;122:193-209.

14. Alharbi FM. Update in vitamin D and multiple sclerosis. Neurosciences (Riyadh) 2015;20:329-35.

15. Popescu BFG, Pirko I, Lucchinetti CF. Pathology of multiple sclerosis: Where do we stand? CONTINUUM Lifelong Learning in Neurology2013.

16. Henstridge CM, Tzioras M, Paolicelli RC. Glial Contribution to Excitatory and Inhibitory Synapse Loss in Neurodegeneration. Front Cell Neurosci 2019;13:63.

17. Love S. Demyelinating diseases. J Clin Pathol 2006;59:1151-9.

18. Murray PD, McGavern DB, Sathornsumetee S, Rodriguez M. Spontaneous remyelination following extensive demyelination is associated with improved neurological function in a viral model of multiple sclerosis. Brain 2001;124:1403-16.

19. Keough M, Yong V. Remyelination therapy for multiple sclerosis. Neurotherapeutics 2013;10:44-54.

20. Taveggia C, Feltri ML, Wrabetz L. Signals to promote myelin formation and repair. Nature Reviews Neurology2010:276-87.

21. Armstrong RC, Mierzwa AJ, Marion CM, Sullivan GM. White matter involvement after TBI: Clues to axon and myelin repair capacity. Experimental Neurology2016:328-33.

22. Ratchford JN, Saidha S, Sotirchos ES, Oh JA, Seigo MA, Eckstein C, Durbin MK, Oakley JD, Meyer SA, Conger A, Frohman TC, Newsome SD, Balcer LJ, Frohman EM, Calabresi PA. Active MS is associated with accelerated retinal ganglion cell/inner plexiform layer thinning. Neurology 2013.

23. L. C, L.K. G. Ocular manifestations of multiple sclerosis. Current Opinion in Ophthalmology 2005.

24. Lucchinetti C, Bruck W, Parisi J, Scheithauer B, Rodriguez M, Lassmann H. Heterogeneity of multiple sclerosis lesions: implications for the pathogenesis of demyelination. Ann Neurol 2000;47:707-17.

25. Steelman AJ, Thompson JP, Li J. Demyelination and remyelination in anatomically distinct regions of the corpus callosum following cuprizone intoxication. Neuroscience Research 2012;72:32-42.

26. Lassmann H, Bradl M. Multiple sclerosis: experimental models and reality. Acta Neuropathol 2017;133:223-44.

27. Dominietto M, Rudin M. Could magnetic resonance provide in vivo histology? Front Genet 2014;4:298.
28. Traboulsee AL, Li DK. The role of MRI in the diagnosis of multiple sclerosis. Adv Neurol 2006;98:125-46.
29. Toosy AT, Mason DF, Miller DH. Optic neuritis. The Lancet Neurology2014.
30. Le Bihan D, Iima M. Diffusion Magnetic Resonance Imaging: What Water Tells Us about Biological Tissues. PLoS Biol 2015;13:e1002203.
31. Avola D, Cinque L, Placidi G. Customized first and second order statistics based operators to support advanced texture analysis of MRI images. Comput Math Methods Med 2013;2013:213901.
32. Harrison LC, Raunio M, Holli KK, Luukkaala T, Savio S, Elovaara I, Soimakallio S, Eskola HJ, Dastidar P. MRI texture analysis in multiple sclerosis: toward a clinical analysis protocol. Acad Radiol 2010;17:696-707.
33. Plemel JR, Liu WQ, Yong VW. Remyelination therapies: a new direction and challenge in multiple sclerosis. Nat Rev Drug Discov 2017;16:617-34.
34. Matsushima GK MP. The neurotoxicant, cuprizone, as a model to study demyelination and remyelination in the central nervous system. Brain Pathol 2001;11:107-16.
35. Bakker DA, Ludwin SK. Blood-brain barrier permeability during Cuprizone-induced demyelination. Implications for the pathogenesis of immune-mediated demyelinating diseases. J Neurol Sci 1987;78:125-37.
36. Gudi V, Gingele S, Skripuletz T, Stangel M. Glial response during cuprizone-induced de- and remyelination in the CNS: lessons learned. Front Cell Neurosci 2014;8:73.
37. Torkildsen O, Brunborg LA, Myhr KM, Bo L. The cuprizone model for demyelination. Acta Neurol Scand Suppl 2008;188:72-6.
38. Galetta SL, Villoslada P, Levin N, Shindler K, Ishikawa H, Parr E, Cadavid D, Balcer LJ. Acute optic neuritis: Unmet clinical needs and model for new therapies. Neurol Neuroimmunol Neuroinflamm 2015;2:e135.
39. Optic Neuritis Study Group TONS. Multiple sclerosis risk after optic neuritis: final optic neuritis treatment trial follow-up. Archives of neurology 2008.
40. Ikuta FU ZH. Distribution of plaques in seventy autopsy cases of multiple sclerosis in the United States. Neurology 1976:26-8.
41. Toussaint D, Perier O, Verstappen A, Bervoets S. Clinicopathological study of the visual pathways, eyes, and cerebral hemispheres in 32 cases of disseminated sclerosis. J Clin Neuroophthalmol 1983;3:211-20.
42. Franklin RJM, Ffrench-Constant C. Regenerating CNS myelin - from mechanisms to experimental medicines. Nat Rev Neurosci 2017;18:753-69.
43. Lubetzki C, Stankoff B. Demyelination in multiple sclerosis. Handb Clin Neurol 2014;122:89-99.
44. Grussu F, Schneider T, Tur C, Yates RL, Tachrount M, Ianus A, Yiannakas MC, Newcombe J, Zhang H, Alexander DC, DeLuca GC, Gandini Wheeler-Kingshott CAM. Neurite dispersion: a new marker of multiple sclerosis spinal cord pathology? Ann Clin Transl Neurol 2017;4:663-79.
45. Podbielska M, Banik NL, Kurowska E, Hogan EL. Myelin recovery in multiple sclerosis: the challenge of remyelination. Brain Sci 2013;3:1282-324.

46. Patrikios P, Stadelmann C, Kutzelnigg A, Rauschka H, Schmidbauer M, Laursen H, Sorensen PS, Bruck W, Lucchinetti C, Lassmann H. Remyelination is extensive in a subset of multiple sclerosis patients (vol 129, pg 3165, 2006). Brain 2007;130:879-.
47. Chari DM. Remyelination in multiple sclerosis. Int Rev Neurobiol 2007;79:589-620.
48. Chari DM, Blakemore WF. New insights into remyelination failure in multiple sclerosis: implications for glial cell transplantation. Mult Scler 2002;8:271-7.
49. Zaimi A, Duval T, Gasecka A, Cote D, Stikov N, Cohen-Adad J. AxonSeg: Open Source Software for Axon and Myelin Segmentation and Morphometric Analysis. Front Neuroinform 2016;10:37.
50. De Stefano N, Narayanan S, Francis GS, Arnaoutelis R, Tartaglia MC, Antel JP, Matthews PM, Arnold DL. Evidence of axonal damage in the early stages of multiple sclerosis and its relevance to disability. Arch Neurol 2001;58:65-70.
51. Denic A JA, Bieber A, Warrington A, et al. The relevance of animal models in multiple sclerosis research. Pathophysiology 2011;18:21-9.
52. Keough MB, Jensen SK, Yong VW. Experimental Demyelination and Remyelination of Murine Spinal Cord by Focal Injection of Lysolecithin. Journal of Visualized Experiments 2015.
53. Kuypers NJ, James KT, Enzmann GU, Magnuson DS, Whittemore SR. Functional consequences of ethidium bromide demyelination of the mouse ventral spinal cord. Exp Neurol 2013;247:615-22.
54. Praet J, Guglielmetti C, Berneman Z, Van der Linden A, Ponsaerts P. Cellular and molecular neuropathology of the cuprizone mouse model: clinical relevance for multiple sclerosis. Neurosci Biobehav Rev 2014;47:485-505.
55. Goldberg J, Clarner T, Beyer C, Kipp M. Anatomical Distribution of Cuprizone-Induced Lesions in C57BL6 Mice. Journal of Molecular Neuroscience 2015;57:166-75.
56. Liu L BA, Darnall L, Hu T et al. CXCR2-positive neutrophils are essential for cuprizone-induced demyelination: relevance to multiple sclerosis. Nat Neurosci 2010;13:319-26.
57. Venturini G. Enzymic activities and sodium, potassium and copper concentrations in mouse brain and liver after cuprizone treatment in vivo. J Neurochem 1973;21:1147-51.
58. Gudi V, Gingele S, Skripuletz T, Stangel M. Glial response during cuprizone-induced de- and remyelination in the CNS: lessons learned. Frontiers in Cellular Neuroscience 2014;8.
59. Peterson LK, Fujinami RS. Inflammation, demyelination, neurodegeneration and neuroprotection in the pathogenesis of multiple sclerosis. J Neuroimmunol 2007;184:37-44.
60. Gean-Marton AD, Vezina LG, Marton KI, Stimac GK, Peyster RG, Taveras JM, Davis KR. Abnormal corpus callosum: a sensitive and specific indicator of multiple sclerosis. Radiology 1991;180:215-21.
61. Suzuki K, Kikkawa Y. Status spongiosus of CNS and hepatic changes induced by cuprizone (biscyclohexanone oxalyldihydrazone). Am J Pathol 1969;54:307-25.
62. Xiao L, Xu H, Zhang Y, Wei Z, He J, Jiang W, Li X, Dyck LE, Devon RM, Deng Y, Li XM. Quetiapine facilitates oligodendrocyte development and prevents mice from myelin breakdown and behavioral changes. Mol Psychiatry 2008;13:697-708.
63. Taylor LC, Gilmore W, Matsushima GK. SJL mice exposed to cuprizone intoxication reveal strain and gender pattern differences in demyelination. Brain Pathol 2009;19:467-79.
64. Irvine KA, Blakemore WF. Remyelination protects axons from demyelination-associated axon degeneration. Brain 2008;131:1464-77.

65. Xing YL, Roth PT, Stratton JA, Chuang BH, Danne J, Ellis SL, Ng SW, Kilpatrick TJ, Merson TD. Adult neural precursor cells from the subventricular zone contribute significantly to oligodendrocyte regeneration and remyelination. J Neurosci 2014;34:14128-46.
66. Nathoo N, Yong VW, Dunn JF. Understanding disease processes in multiple sclerosis through magnetic resonance imaging studies in animal models. Neuroimage-Clin 2014;4:743-56.
67. Jeffery ND, Blakemore WF. Remyelination of mouse spinal cord axons demyelinated by local injection of lysolecithin. J Neurocytol 1995;24:775-81.
68. Rawji KS, Kappen J, Tang WW, Teo WL, Plemel JR, Stys PK, Yong VW. Deficient Surveillance and Phagocytic Activity of Myeloid Cells Within Demyelinated Lesions in Aging Mice Visualized by Ex Vivo Live Multiphoton Imaging. Journal of Neuroscience 2018;38:1973-88.
69. Bieber AJ, Warrington A, Asakura K, Ciric B, Kaveri SV, Pease LR, Rodriguez M. Human antibodies accelerate the rate of remyelination following lysolecithin-induced demyelination in mice. Glia 2002;37:241-9.
70. Rawji KS, Yong VW. The benefits and detriments of macrophages/microglia in models of multiple sclerosis. Clin Dev Immunol 2013;2013:948976.
71. Tillema JM, Pirko I. Neuroradiological evaluation of demyelinating disease. Therapeutic Advances in Neurological Disorders 2013;6:249-68.
72. de la Cruz J, Kupersmith MJ. Clinical profile of simultaneous bilateral optic neuritis in adults. Br J Ophthalmol 2006;90:551-4.
73. Costello F. The afferent visual pathway: designing a structural-functional paradigm of multiple sclerosis. ISRN neurology 2013.
74. Balcer LJ, Miller DH, Reingold SC, Cohen JA. Vision and vision-related outcome measures in multiple sclerosis. Brain2015.
75. Youl BD, Turano G, Miller DH, Towell AD, Macmanus DG, Moore SG, Jones SJ, Barrett G, Kendall BE, Moseley IF, Tofts PS, Halliday AM, Mcdonald WI. The pathophysiology of acute optic neuritis: An association of gadolinium leakage with clinical and electrophysiological deficits. Brain 1991.
76. Broadway DC. How to test for a relative afferent pupillary defect (RAPD). Community Eye Health 2012;25:58-9.
77. Hickman SJ, Toosy AT, Miszkiel KA, Jones SJ, Altmann DR, MacManus DG, Plant GT, Thompson AJ, Miller DH. Visual recovery following acute optic neuritis--a clinical, electrophysiological and magnetic resonance imaging study. J Neurol 2004.
78. PM G, RD. S. Cranial nerve II: vision. Psychiatry (Edgmont) 2009;6:32.
79. PM. K. Kanski's Clinical Ophthalmology: A Systematic Approach.
80. Bradl M, Lassmann H. Oligodendrocytes: Biology and pathology. Acta Neuropathologica2010.
81. Miller D, Barkhof F, Montalban X, Thompson A, Filippi M. Clinically isolated syndromes suggestive of multiple sclerosis, part I: Natural history, pathogenesis, diagnosis, and prognosis. Lancet Neurology2005.
82. Quinn TA, Dutt M, Shindler KS. Optic neuritis and retinal ganglion cell loss in a chronic murine model of multiple sclerosis. Frontiers in Neurology 2011.
83. Sakai RE, Feller DJ, Galetta KM, Galetta SL, Balcer LJ. Vision in multiple sclerosis: the story, structure-function correlations, and models for neuroprotection. J Neuroophthalmol 2011.

84. Jenkins T, Ciccarelli O, Toosy A, Miszkiel K, Wheeler-Kingshott C, Altmann D, Mancini L, Jones S, Plant G, Miller D, Thompson A. Dissecting structure-function interactions in acute optic neuritis to investigate neuroplasticity. Human Brain Mapping 2010;31:276-86.
85. Aktas O, Albrecht P, Hartung HP. Optic neuritis as a phase 2 paradigm for neuroprotection therapies of multiple sclerosis: update on current trials and perspectives. Curr Opin Neurol 2016;29:199-204.
86. Micieli JA, Margolin E. A 30-year-old woman with vision loss and painful eye movements. CMAJ 2015;187:673-5.
87. Fazzone HE, Lefton DR, Kupersmith MJ. Optic neuritis: correlation of pain and magnetic resonance imaging. Ophthalmology 2003;110:1646-9.
88. Owidzka M, Wilczynski M, Omulecki W. Evaluation of contrast sensitivity measurements after retrobulbar optic neuritis in Multiple Sclerosis. Graefes Arch Clin Exp Ophthalmol 2014;252:673-7.
89. Lueck CJ, Gilmour DF, McIlwaine GG. Neuro-ophthalmology: examination and investigation. J Neurol Neurosurg Psychiatry 2004;75 Suppl 4:iv2-11.
90. Wilhelm H, Schabet M. The Diagnosis and Treatment of Optic Neuritis. Dtsch Arztebl Int 2015;112:616-25; quiz 26.
91. Henderson APD, Altmann DR, Trip SA, Miszkiel KA, Schlottmann PG, Jones SJ, Garway-Heath DF, Plant GT, Miller DH. Early factors associated with axonal loss after optic neuritis. Annals of Neurology 2011.
92. Saidha S, Sotirchos ES, Ibrahim MA, Crainiceanu CM, Gelfand JM, Sepah YJ, Ratchford JN, Oh J, Seigo MA, Newsome SD, Balcer LJ, Frohman EM, Green AJ, Nguyen QD, Calabresi PA. Microcystic macular oedema, Thickness of the inner nuclear layer of the retina, and disease characteristics in multiple sclerosis: A retrospective study. The Lancet Neurology 2012.
93. Lamirel C, Newman NJ, Biousse V. Optical coherence tomography (OCT) in optic neuritis and multiple sclerosis. Rev Neurol (Paris) 2010;166:978-86.
94. Rebolleda G, Diez-Alvarez L, Casado A, Sanchez-Sanchez C, de Dompablo E, Gonzalez-Lopez JJ, Munoz-Negrete FJ. OCT: New perspectives in neuro-ophthalmology. Saudi J Ophthalmol 2015;29:9-25.
95. Walter SD, Ishikawa H, Galetta KM, Sakai RE, Feller DJ, Henderson SB, Wilson JA, Maguire MG, Galetta SL, Frohman E, Calabresi PA, Schuman JS, Balcer LJ. Ganglion cell loss in relation to visual disability in multiple sclerosis. Ophthalmology 2012;119:1250-7.
96. Frohman EM, Dwyer MG, Frohman T, Cox JL, Salter A, Greenberg BM, Hussein S, Conger A, Calabresi P, Balcer LJ, Zivadinov R. Relationship of optic nerve and brain conventional and non-conventional MRI measures and retinal nerve fiber layer thickness, as assessed by OCT and GDx: a pilot study. J Neurol Sci 2009;282:96-105.
97. Costello F, Burton JM. Retinal imaging with optical coherence tomography: a biomarker in multiple sclerosis? Eye Brain 2018;10:47-63.
98. Noval S, Contreras I, Munoz S, Oreja-Guevara C, Manzano B, Rebolleda G. Optical coherence tomography in multiple sclerosis and neuromyelitis optica: an update. Mult Scler Int 2011;2011:472790.
99. Yaqoob Z, Wu J, Yang C. Spectral domain optical coherence tomography: a better OCT imaging strategy. Biotechniques 2005;39:S6-13.
100. Saidha S, Syc SB, Ibrahim MA, Eckstein C, Warner CV, Farrell SK, Oakley JD, Durbin MK, Meyer SA, Balcer LJ, Frohman EM, Rosenzweig JM, Newsome SD, Ratchford JN, Nguyen

QD, Calabresi PA. Primary retinal pathology in multiple sclerosis as detected by optical coherence tomography. Brain 2011;134:518-33.
101. Costello F, Hodge W, Pan YI, Metz L, Kardon RH. Retinal nerve fiber layer and future risk of multiple sclerosis. The Canadian journal of neurological sciences Le journal canadien des sciences neurologiques 2008;35:482-7.
102. Vizzeri G, Balasubramanian M, Bowd C, Weinreb RN, Medeiros FA, Zangwill LM. Spectral domain-optical coherence tomography to detect localized retinal nerve fiber layer defects in glaucomatous eyes. Opt Express 2009;17:4004-18.
103. Kolappan M, Henderson AP, Jenkins TM, Wheeler-Kingshott CA, Plant GT, Thompson AJ, Miller DH. Assessing structure and function of the afferent visual pathway in multiple sclerosis and associated optic neuritis. J Neurol 2009;256:305-19.
104. Burton EV, Greenberg BM, Frohman EM. Optic neuritis: A mechanistic view. Pathophysiology 2011;18:81-92.
105. Walsh P, Kane N, Butler S. The clinical role of evoked potentials. J Neurol Neurosurg Psychiatry 2005;76 Suppl 2:ii16-22.
106. Kundra O. [The role of evoked potentials in neurological clinical practice]. Ideggyogy Sz 2005;58:364-79.
107. Grover LK, Hood DC, Ghadiali Q, Grippo TM, Wenick AS, Greenstein VC, Behrens MM, Odel JG. A comparison of multifocal and conventional visual evoked potential techniques in patients with optic neuritis/multiple sclerosis. Doc Ophthalmol 2008;117:121-8.
108. Kothari R, Bokariya P, Singh S, Singh R. A Comprehensive Review on Methodologies Employed for Visual Evoked Potentials. Scientifica (Cairo) 2016;2016:9852194.
109. Creel DJ. Visually Evoked Potentials by Donnell J. Creel. Webvision: The Organization of the Retina and Visual System 2016.
110. Klistorner A, Arvind H, Nguyen T, Garrick R, Paine M, Graham S, O'Day J, Yiannikas C. Multifocal VEP and OCT in optic neuritis: A topographical study of the structure - Function relationship. Documenta Ophthalmologica 2009;118:129-37.
111. Naismith RT, Tutlam NT, Xu J, Shepherd JB, Klawiter EC, Song SK, Cross AH. Optical coherence tomography is less sensitive than visual evoked potentials in optic neuritis. Neurology 2009;73:46-52.
112. Kim NH, Kim HJ, Park CY, Jeong KS, Cho JY. Optical Coherence Tomography versus Visual Evoked Potentials for Detecting Visual Pathway Abnormalities in Patients with Neuromyelitis Optica Spectrum Disorder. J Clin Neurol 2018;14:200-5.
113. Grecescu M. Optical coherence tomography versus visual evoked potentials in detecting subclinical visual impairment in multiple sclerosis. J Med Life 2014;7:538-41.
114. Kaunzner UW, Gauthier SA. MRI in the assessment and monitoring of multiple sclerosis: an update on best practice. Ther Adv Neurol Disord 2017;10:247-61.
115. Sahraian MA, Eshaghi A. Role of MRI in diagnosis and treatment of multiple sclerosis. Clin Neurol Neurosurg 2010;112:609-15.
116. Hickman SJ. Optic nerve imaging in multiple sclerosis. J Neuroimaging 2007;17 Suppl 1:42S-5S.
117. Swanton JK, Fernando KT, Dalton CM, Miszkiel KA, Altmann DR, Plant GT, Thompson AJ, Miller DH. Early MRI in optic neuritis: the risk for clinically definite multiple sclerosis. Mult Scler 2010;16:156-65.
118. Berg S, Kaschka I, Utz KS, Huhn K, Lammer A, Lammer R, Waschbisch A, Kloska S, Lee DH, Doerfler A, Linker RA. Baseline magnetic resonance imaging of the optic nerve provides

limited predictive information on short-term recovery after acute optic neuritis. PLoS One 2015;10:e0113961.
119. Hoorbakht H, Bagherkashi F. Optic neuritis, its differential diagnosis and management. Open Ophthalmology Journal 2012.
120. Kupersmith MJ WJ, Garvin M, Kardon R. Retinal ganglion cell layer thinning and vision outcome in optic neuritis over six months in multiple sclerosis. MULTIPLE SCLEROSIS JOURNAL 2014;20:358-9.
121. McMahon KL, Cowin G, Galloway G. Magnetic Resonance Imaging: The Underlying Principles. Journal of Orthopaedic & Sports Physical Therapy 2011;41:806-19.
122. Currie S, Hoggard N, Craven IJ, Hadjivassiliou M, Wilkinson ID. Understanding MRI: basic MR physics for physicians. Postgrad Med J 2013;89:209-23.
123. Lee N, Hyeon T. Designed synthesis of uniformly sized iron oxide nanoparticles for efficient magnetic resonance imaging contrast agents. Chem Soc Rev 2012;41:2575-89.
124. R W, PW S, J S. Handbook of the vulnerable plaque. 2007:256.
125. R B, G L, R P, S T, AR M, J S, C M, M C, S S, A N, TP R. MR pulse sequences: what every radiologist wants to know but is afraid to ask. Radiographics 2006;26:513-37.
126. JH S, L J, N S. T1-Hypointense Lesions (T1 Black Holes) in Mild-to-Moderate Disability Relapsing Multiple Sclerosis. InEarly Indicators Early Treatments Neuroprotection in Multiple Sclerosis 2004:135-9.
127. MA S, EW R, S H, L K. Black holes in multiple sclerosis: definition, evolution, and clinical correlations. Acta Neurologica Scandinavica 2010;122:1-8.
128. MA VW, W K, PH S, JH VW, R R, J V, CH P, F. B. Histopathologic correlate of hypointense lesions on T1-weighted spin-echo MRI in multiple sclerosis. Neurology 1998;50:1282-8.
129. Mallik S, Samson RS, Wheeler-Kingshott CAM, Miller DH. Imaging outcomes for trials of remyelination in multiple sclerosis. Journal of Neurology, Neurosurgery and Psychiatry 2014;85:1396-404.
130. Saidha S, Al-Louzi O, Ratchford JN, Bhargava P, Oh J, Newsome SD, Prince JL, Pham D, Roy S, Van Zijl P, Balcer LJ, Frohman EM, Reich DS, Crainiceanu C, Calabresi PA. Optical coherence tomography reflects brain atrophy in multiple sclerosis: A four-year study. Annals of Neurology 2015;78:801-13.
131. Rovira A, Auger C, Alonso J. Magnetic resonance monitoring of lesion evolution in multiple sclerosis. Therapeutic Advances in Neurological Disorders 2013;6:298-310.
132. SA T, DH M. Imaging in multiple sclerosis. Journal of Neurology, Neurosurgery & Psychiatry 2005;76:11-8.
133. Gajofatto A, Calabrese M, Benedetti MD, Monaco S. Clinical, MRI, and CSF markers of disability progression in multiple sclerosis. Disease Markers 2013;35:687-99.
134. Zhou Z, Lu ZR. Gadolinium-based contrast agents for magnetic resonance cancer imaging. Wiley Interdisciplinary Reviews: Nanomedicine and Nanobiotechnology 2013;5:1-18.
135. SN G, MA B, JG W, DA A, CB. S. MR contrast agents for liver imaging: what, when, how. . Radiographics 2006;26:1621-36.
136. Obermeier B, Daneman R, Ransohoff RM. Development, maintenance and disruption of the blood-brain barrier. Nature Medicine 2013;19:1584-96.
137. Al-Saeed O, Ismail M, Athyal R, Sheikh M. Fat-saturated post gadolinium T1 imaging of the brain in multiple sclerosis. Acta Radiologica 2011;52:570-4.

138. J G, J M, WD BJ, A M, RG Q. Enhancement and Demyefination of the Intraorbital Optic Nerve: Fat Suppression Magnetic Resonance Imaging. Ophthalmology 1992;99:713-9.
139. Kupersmith MJ, Alban T, Zeiffer B, Lefton D. Contrast-enhanced MRI in acute optic neuritis: relationship to visual performance. Brain : a journal of neurology 2002.
140. Wetzel SG, Johnson G, Tan AGS, Cha S, Knopp EA, Lee VS, Thomasson D, Rofsky NM. Three-dimensional, T1-weighted gradient-echo imaging of the brain with a volumetric interpolated examination. American Journal of Neuroradiology 2002;23:995-1002.
141. Bakshi R, Minagar A, Jaisani Z, Wolinsky JS. Imaging of multiple sclerosis: role in neurotherapeutics. NeuroRx 2005;2:277-303.
142. Kim KW, MacFall JR, Payne ME. Classification of white matter lesions on magnetic resonance imaging in elderly persons. Biol Psychiatry 2008;64:273-80.
143. Kaunzner UW, Gauthier SA. MRI in the assessment and monitoring of multiple sclerosis: An update on best practice. Therapeutic Advances in Neurological Disorders 2017;10:247-61.
144. Filippi M, Rocca MA, Ciccarelli O, De Stefano N, Evangelou N, Kappos L, Rovira A, Sastre-Garriga J, Tintorè M, Frederiksen JL, Gasperini C, Palace J, Reich DS, Banwell B, Montalban X, Barkhof F. MRI criteria for the diagnosis of multiple sclerosis: MAGNIMS consensus guidelines. The Lancet Neurology 2016;15:292-303.
145. McDonald WI, Miller DH, Barnes D. The pathological evolution of multiple sclerosis. Neuropathology and Applied Neurobiology 1992;18:319-34.
146. Reich DS, Smith SA, Gordon-Lipkin EM, Ozturk A, Caffo BS, Balcer LJ, Calabresi PA. Damage to the optic radiation in multiple sclerosis is associated with retinal injury and visual disability. Archives of Neurology 2009;66:998-1006.
147. HE K, A M, J. F. Optic neuritis with marked distension of the optic nerve sheath due to local fluid congestion. British journal of ophthalmology 2003;87:249.
148. Filippi M, Rocca MA. MR Imaging of Multiple Sclerosis. Radiology 2011;259:659-81.
149. Miller DH, Barkhof F, Frank JA, Parker GJM, Thompson AJ. Measurement of atrophy in multiple sclerosis: pathological\nbasis, methodological aspects and clinical relevance. Brain 2002;125:1676-95.
150. Y F, TM T, JX C. New imaging techniques in the diagnosis of multiple sclerosis. Expert opinion on medical diagnostics 2008;2:1055-65.
151. Gala F. Magnetic resonance imaging of optic nerve. Indian J Radiol Imaging 2015;25:421-38.
152. Aiken AH, Mukherjee P, Green AJ, Glastonbury CM. MR imaging of optic neuropathy with extended echo-train acquisition fluid-attenuated inversion recovery. AJNR Am J Neuroradiol 2011;32:301-5.
153. A P, MC P, NS P, M B, U A, V D, L. B. Usefulness of selective partial inversion recover (SPIR) sequences in optic nerve diseases. La Radiologia medica 1999;97:236-40.
154. Delfaut EM, Beltran J, Johnson G, Rousseau J, Marchandise X, Cotten A. Fat suppression in MR imaging: Techniques and pitfalls. Radiographics 1999;19:373-82.
155. Simha A, Irodi A, David S. Magnetic resonance imaging for the ophthalmologist: A primer. Indian J Ophthalmol 2012;60:301-10.
156. Wu J LLQ, Gu J.P., Yin X.D. The Application of Fat-Suppression MR Pulse Sequence in the Diagnosis of Bone-Joint Disease. International Journal of Medical Physics, Clinical Engineering and Radiation Oncology 2012;1:7.

157. Del Grande F, Santini F, Herzka DA, Aro MR, Dean CW, Gold GE, Carrino JA. Fat-suppression techniques for 3-T MR imaging of the musculoskeletal system. Radiographics 2014;34:217-33.
158. Bakshi R, Ariyaratana S, Benedict RH, Jacobs L. Fluid-attenuated inversion recovery magnetic resonance imaging detects cortical and juxtacortical multiple sclerosis lesions. Arch Neurol 2001;58:742-8.
159. Hodel J, Outteryck O, Bocher AL, Zéphir H, Lambert O, Benadjaoud MA, Chechin D, Pruvo JP, Vermersch P, Leclerc X. Comparison of 3D double inversion recovery and 2D STIR FLAIR MR sequences for the imaging of optic neuritis: pilot study. European Radiology 2014.
160. Trivedi R GR. Magnetic Resonance Imaging of Neurorogical Diseases in Tropics. 1st ed ed: Jaypee Medical Inc.; 2004.
161. Heath F, Hurley SA, Johansen-Berg H, Sampaio-Baptista C. Advances in noninvasive myelin imaging. Dev Neurobiol 2018;78:136-51.
162. Haines JD, Inglese M, Casaccia P. Axonal damage in multiple sclerosis. Mt Sinai J Med 2011;78:231-43.
163. Zaaraoui W, Deloire M, Merle M, Girard C, Raffard G, Biran M, Inglese M, Petry KG, Gonen O, Brochet B, Franconi JM, Dousset V. Monitoring demyelination and remyelination by magnetization transfer imaging in the mouse brain at 9.4 T. MAGMA 2008;21:357-62.
164. Cercignani M, Bozzali M, Iannucci G, Comi G, Filippi M. Magnetisation transfer ratio and mean diffusivity of normal appearing white and grey matter from patients with multiple sclerosis. J Neurol Neurosurg Psychiatry 2001;70:311-7.
165. Bakshi R, Thompson AJ, Rocca Ma, Pelletier D, Dousset V, Barkhof F, Inglese M, Guttmann CRG, Horsfield Ma, Filippi M. MRI in multiple sclerosis: current status and future prospects. Lancet neurology 2008;7:615-25.
166. Vavasour IM, Laule C, Li DK, Traboulsee AL, MacKay AL. Is the magnetization transfer ratio a marker for myelin in multiple sclerosis? J Magn Reson Imaging 2011;33:713-8.
167. Pike GB, De Stefano N, Narayanan S, Worsley KJ, Pelletier D, Francis GS, Antel JP, Arnold DL. Multiple sclerosis: magnetization transfer MR imaging of white matter before lesion appearance on T2-weighted images. Radiology 2000;215:824-30.
168. Filippi M, Rocca MA. Magnetization transfer magnetic resonance imaging in the assessment of neurological diseases. J Neuroimaging 2004;14:303-13.
169. Symms M, Jager HR, Schmierer K, Yousry TA. A review of structural magnetic resonance neuroimaging. J Neurol Neurosurg Psychiatry 2004;75:1235-44.
170. de Figueiredo EH, Borgonovi AF, Doring TM. Basic concepts of MR imaging, diffusion MR imaging, and diffusion tensor imaging. Magn Reson Imaging Clin N Am 2011;19:1-22.
171. Werring DJ, Brassat D, Droogan AG, Clark CA, Symms MR, Barker GJ, MacManus DG, Thompson AJ, Miller DH. The pathogenesis of lesions and normal-appearing white matter changes in multiple sclerosis: a serial diffusion MRI study. Brain 2000;123 (Pt 8):1667-76.
172. Alger JR. The diffusion tensor imaging toolbox. J Neurosci 2012;32:7418-28.
173. Sbardella E, Tona F, Petsas N, Pantano P. DTI Measurements in Multiple Sclerosis: Evaluation of Brain Damage and Clinical Implications. Mult Scler Int 2013;2013:671730.
174. Fields RD. White matter in learning, cognition and psychiatric disorders. Trends Neurosci 2008;31:361-70.
175. Andrew L. Alexander JEL, Mariana Lazar, Aaron S. Field. Diffusion Tensor Imaging of the Brain. Neurotherapeutics : the journal of the American Society for Experimental NeuroTherapeutics 2007.

176. Holdsworth SJ, Bammer R. Magnetic resonance imaging techniques: fMRI, DWI, and PWI. Semin Neurol 2008;28:395-406.
177. van der Walt A, Kolbe SC, Wang YE, Klistorner A, Shuey N, Ahmadi G, Paine M, Marriott M, Mitchell P, Egan GF, Butzkueven H, Kilpatrick TJ. Optic nerve diffusion tensor imaging after acute optic neuritis predicts axonal and visual outcomes. PLoS One 2013;8:e83825.
178. Smith SA, Williams ZR, Ratchford JN, Newsome SD, Farrell SK, Farrell JA, Gifford A, Miller NR, van Zijl PC, Calabresi PA, Reich DS. Diffusion tensor imaging of the optic nerve in multiple sclerosis: association with retinal damage and visual disability. AJNR Am J Neuroradiol 2011;32:1662-8.
179. Aung WY, Mar S, Benzinger TL. Diffusion tensor MRI as a biomarker in axonal and myelin damage. Imaging Med 2013;5:427-40.
180. Naismith RT, Xu J, Tutlam NT, Trinkaus K, Cross AH, Song SK. Radial diffusivity in remote optic neuritis discriminates visual outcomes. Neurology 2010;74:1702-10.
181. Mustafi SM, Harezlak J, Kodiweera C, Randolph JS, Ford JC, Wishart HA, Wu YC. Detecting white matter alterations in multiple sclerosis using advanced diffusion magnetic resonance imaging. Neural Regen Res 2019;14:114-23.
182. Inglese M, Bester M. Diffusion imaging in multiple sclerosis: research and clinical implications. NMR Biomed 2010;23:865-72.
183. Tuch DS, Reese TG, Wiegell MR, Makris N, Belliveau JW, Wedeen VJ. High angular resolution diffusion imaging reveals intravoxel white matter fiber heterogeneity. Magn Reson Med 2002;48:577-82.
184. Beaulieu C. The basis of anisotropic water diffusion in the nervous system - a technical review. NMR Biomed 2002;15:435-55.
185. Zhang H, Schneider T, Wheeler-Kingshott CA, Alexander DC. NODDI: practical in vivo neurite orientation dispersion and density imaging of the human brain. Neuroimage 2012;61:1000-16.
186. Assaf Y, Basser PJ. Composite hindered and restricted model of diffusion (CHARMED) MR imaging of the human brain. Neuroimage 2005;27:48-58.
187. Steven AJ, Zhuo J, Melhem ER. Diffusion kurtosis imaging: an emerging technique for evaluating the microstructural environment of the brain. AJR Am J Roentgenol 2014;202:W26-33.
188. Sowa P, Harbo HF, White NS, Celius EG, Bartsch H, Berg-Hansen P, Moen SM, Bjornerud A, Westlye LT, Andreassen OA, Dale AM, Beyer MK. Restriction spectrum imaging of white matter and its relation to neurological disability in multiple sclerosis. Mult Scler 2019;25:687-98.
189. Assaf Y, Ben-Bashat D, Chapman J, Peled S, Biton IE, Kafri M, Segev Y, Hendler T, Korczyn AD, Graif M, Cohen Y. High b-value q-space analyzed diffusion-weighted MRI: application to multiple sclerosis. Magn Reson Med 2002;47:115-26.
190. Barritt AW, Gabel MC, Cercignani M, Leigh PN. Emerging Magnetic Resonance Imaging Techniques and Analysis Methods in Amyotrophic Lateral Sclerosis. Front Neurol 2018;9:1065.
191. Tariq M, Schneider T, Alexander DC, Gandini Wheeler-Kingshott CA, Zhang H. Bingham-NODDI: Mapping anisotropic orientation dispersion of neurites using diffusion MRI. Neuroimage 2016;133:207-23.
192. Chen S, Li X. Functional magnetic resonance imaging for imaging neural activity in the human brain: the annual progress. Comput Math Methods Med 2012;2012:613465.

193. Tomassini V, Matthews PM, Thompson AJ, Fuglo D, Geurts JJ, Johansen-Berg H, Jones DK, Rocca MA, Wise RG, Barkhof F, Palace J. Neuroplasticity and functional recovery in multiple sclerosis. Nat Rev Neurol 2012;8:635-46.
194. Rogers BP, Morgan VL, Newton AT, Gore JC. Assessing functional connectivity in the human brain by fMRI. Magn Reson Imaging 2007;25:1347-57.
195. Raz N, Levin N. Cortical and white matter mapping in the visual system-more than meets the eye: on the importance of functional imaging to understand visual system pathologies. Front Integr Neurosci 2014;8:68.
196. Langkilde AR, Frederiksen JL, Rostrup E, Larsson HB. Functional MRI of the visual cortex and visual testing in patients with previous optic neuritis. Eur J Neurol 2002;9:277-86.
197. Jenkins TM, Toosy AT, Ciccarelli O, Miszkiel KA, Wheeler-Kingshott CA, Henderson AP, Kallis C, Mancini L, Plant GT, Miller DH, Thompson AJ. Neuroplasticity predicts outcome of optic neuritis independent of tissue damage. Ann Neurol 2010;67:99-113.
198. Filippi M, Rocca MA. Present and future of fMRI in multiple sclerosis. Expert Rev Neurother 2013;13:27-31.
199. Ford TC, Crewther DP. A Comprehensive Review of the (1)H-MRS Metabolite Spectrum in Autism Spectrum Disorder. Front Mol Neurosci 2016;9:14.
200. Moffett JR, Ross B, Arun P, Madhavarao CN, Namboodiri AM. N-Acetylaspartate in the CNS: from neurodiagnostics to neurobiology. Prog Neurobiol 2007;81:89-131.
201. Kirov, II, Patil V, Babb JS, Rusinek H, Herbert J, Gonen O. MR spectroscopy indicates diffuse multiple sclerosis activity during remission. J Neurol Neurosurg Psychiatry 2009;80:1330-6.
202. Narayana PA. Magnetic resonance spectroscopy in the monitoring of multiple sclerosis. J Neuroimaging 2005;15:46S-57S.
203. de Seze J, Blanc F, Kremer S, Collongues N, Fleury M, Marcel C, Namer IJ. Magnetic resonance spectroscopy evaluation in patients with neuromyelitis optica. J Neurol Neurosurg Psychiatry 2010;81:409-11.
204. Pfueller CF, Brandt AU, Schubert F, Bock M, Walaszek B, Waiczies H, Schwenteck T, Dorr J, Bellmann-Strobl J, Mohr C, Weinges-Evers N, Ittermann B, Wuerfel JT, Paul F. Metabolic changes in the visual cortex are linked to retinal nerve fiber layer thinning in multiple sclerosis. PLoS One 2011;6:e18019.
205. Tedeschi G, Bonavita S, McFarland HF, Richert N, Duyn JH, Frank JA. Proton MR spectroscopic imaging in multiple sclerosis. Neuroradiology 2002;44:37-42.
206. Hashimoto M, Ohtsuka K, Harada K. N-acetylaspartate concentration in the chiasm measured by in vivo proton magnetic resonance spectroscopy. Jpn J Ophthalmol 2004;48:353-7.
207. Chapter8 - Moving Beyond DTI: High Angular Resolution Diffusion Imaging (HARDI). Second Edition ed: ACADEMIC PRESS; 2014.
208. Wheeler-Kingshott CA, Cercignani M. About "axial" and "radial" diffusivities. Magn Reson Med 2009;61:1255-60.
209. Schneider T, Brownlee W, Zhang H, Ciccarelli O, Miller DH, Wheeler-Kingshott CG. Sensitivity of multi-shell NODDI to multiple sclerosis white matter changes: a pilot study. Funct Neurol 2017;32:97-101.
210. Luo T, Oladosu O, Rawji KS, Zhai P, Pridham G, Hossain S, Zhang Y. Characterizing Structural Changes With Devolving Remyelination Following Experimental Demyelination Using High Angular Resolution Diffusion MRI and Texture Analysis. J Magn Reson Imaging 2018.

211. M.S. Hossain OO, T. Lou , S. Sharma , Y. Zhang. Investigating the potential of high angular resolution diffusion imaging metrics and texture angular entropy for monitoring de- and remyelination in a cuprizone model of multiple sclerosis. 34th CONGRESS OF THE EUROPIAN COMMITTEE FOR TREATMENT AND RESEARCH IN MULTIPLE SCLEROSIS; 2018 Oct 10; Berlin, Germany; 2018.
212. De Santis S, Bastiani M, Droby A, Kolber P, Zipp F, Pracht E, Stoecker T, Groppa S, Roebroeck A. Characterizing Microstructural Tissue Properties in Multiple Sclerosis with Diffusion MRI at 7T and 3T: The Impact of the Experimental Design. Neuroscience 2019;403:17-26.
213. Granberg T, Fan Q, Treaba CA, Ouellette R, Herranz E, Mangeat G, Louapre C, Cohen-Adad J, Klawiter EC, Sloane JA, Mainero C. In vivo characterization of cortical and white matter neuroaxonal pathology in early multiple sclerosis. Brain 2017;140:2912-26.
214. By S, Xu J, Box BA, Bagnato FR, Smith SA. Application and evaluation of NODDI in the cervical spinal cord of multiple sclerosis patients. Neuroimage Clin 2017;15:333-42.
215. Tur C, Goodkin O, Altmann DR, Jenkins TM, Miszkiel K, Mirigliani A, Fini C, Gandini Wheeler-Kingshott CA, Thompson AJ, Ciccarelli O, Toosy AT. Longitudinal evidence for anterograde trans-synaptic degeneration after optic neuritis. Brain 2016;139:816-28.
216. Zhang Y, Metz LM, Scott JN, Trufyn J, Fick GH, Costello F. MRI texture heterogeneity in the optic nerve predicts visual recovery after acute optic neuritis. NeuroImage: Clinical 2014.
217. Zhang Y. MRI texture analysis in multiple sclerosis. Int J Biomed Imaging 2012;2012:762804.
218. Haralick RM. Statistical and Structural Approaches to Texture. P Ieee 1979;67:786-804.
219. Mathias JM, Tofts PS, Losseff NA. Texture analysis of spinal cord pathology in multiple sclerosis. Magn Reson Med 1999;42:929-35.
220. Zhang J, Tong L, Wang L, Li N. Texture analysis of multiple sclerosis: a comparative study. Magn Reson Imaging 2008;26:1160-6.
221. Yu O, Steibel J, Mauss Y, Guignard B, Eclancher B, Chambron J, Grucker D. Remyelination assessment by MRI texture analysis in a cuprizone mouse model. Magn Reson Imaging 2004;22:1139-44.
222. Zhang Y, Moore GRW, Laule C, Bjarnason TA, Kozlowski P, Traboulsee A, Li DKB. Pathological correlates of magnetic resonance imaging texture heterogeneity in multiple sclerosis. Annals of Neurology 2013;74:91-9.
223. Sharma S, Zhang Y. Fourier transform power spectrum is a potential measure of tissue alignment in standard MRI: A multiple sclerosis study. PLoS ONE 2017;12.
224. Sharma S, Laule C, Moore GRW, Li DKB, Zhang Y. Correlating new directional measures of myelin and axonal integrity in T2-weighted MRI with quantitative histology in multiple sclerosis. J Neurosci Methods 2019;311:369-76.
225. Liu HJ, Zhou HF, Zong LX, Liu MQ, Wei SH, Chen ZY. MRI Histogram Texture Feature Analysis of the Optic Nerve in the Patients with Optic Neuritis. Chin Med Sci J 2019;34:18-23.
226. Ansari MK, Yong HY, Metz L, Yong VW, Zhang Y. Changes in tissue directionality reflect differences in myelin content after demyelination in mice spinal cords. J Struct Biol 2014;188:116-22.
227. Bigun J. Vision with Direction: A Systemic Introduction to Image Processing and Computer Vision Germany: Springer; 2006.
228. Rezakhaniha R, Agianniotis A, Schrauwen JT, Griffa A, Sage D, Bouten CV, van de Vosse FN, Unser M, Stergiopulos N. Experimental investigation of collagen waviness and orientation in

the arterial adventitia using confocal laser scanning microscopy. Biomech Model Mechanobiol 2012;11:461-73.
229. Budde MD, Frank JA. Examining brain microstructure using structure tensor analysis of histological sections. Neuroimage 2012;63:1-10.
230. Abou Zeid N, Bhatti MT. Acute inflammatory demyelinating optic neuritis: evidence-based visual and neurological considerations. Neurologist 2008;14:207-23.
231. Payne SC, Bartlett CA, Harvey AR, Dunlop SA, Fitzgerald M. Myelin sheath decompaction, axon swelling, and functional loss during chronic secondary degeneration in rat optic nerve. Invest Ophthalmol Vis Sci 2012;53:6093-101.
232. Martola J, Stawiarz L, Fredrikson S, Hillert J, Bergstrom J, Flodmark O, Kristoffersen Wiberg M. Progression of non-age-related callosal brain atrophy in multiple sclerosis: a 9-year longitudinal MRI study representing four decades of disease development. J Neurol Neurosurg Psychiatry 2007;78:375-80.
233. Sepehrband F, Alexander DC, Clark KA, Kurniawan ND, Yang Z, Reutens DC. Parametric Probability Distribution Functions for Axon Diameters of Corpus Callosum. Front Neuroanat 2016;10:59.
234. de Waegh SM, Lee VM, Brady ST. Local modulation of neurofilament phosphorylation, axonal caliber, and slow axonal transport by myelinating Schwann cells. Cell 1992;68:451-63.
235. Huang SY, Tobyne SM, Nummenmaa A, Witzel T, Wald LL, McNab JA, Klawiter EC. Characterization of Axonal Disease in Patients with Multiple Sclerosis Using High-Gradient-Diffusion MR Imaging. Radiology 2016;280:244-51.
236. Stidworthy MF, Genoud S, Suter U, Mantei N, Franklin RJM. Quantifying the early stages of remyelination following cuprizone-induced demyelination. Brain pathology (Zurich, Switzerland) 2003;13:329-39.
237. Xie M, Tobin JE, Budde MD, Chen CI, Trinkaus K, Cross AH, McDaniel DP, Song SK, Armstrong RC. Rostrocaudal analysis of corpus callosum demyelination and axon damage across disease stages refines diffusion tensor imaging correlations with pathological features. Journal of Neuropathology and Experimental Neurology 2010;69:704-16.
238. Wu QZ, Yang Q, Cate HS, Kemper D, Binder M, Wang HX, Fang K, Quick MJ, Marriott M, Kilpatrick TJ, Egan GF. MRI identification of the rostral-caudal pattern of pathology within the corpus callosum in the cuprizone mouse model. J Magn Reson Imaging 2008;27:446-53.
239. Ozturk A, Smith SA, Gordon-Lipkin EM, Harrison DM, Shiee N, Pham DL, Caffo BS, Calabresi PA, Reich DS. MRI of the corpus callosum in multiple sclerosis: association with disability. Mult Scler 2010;16:166-77.
240. Taylor LC, Gilmore W, Ting JP, Matsushima GK. Cuprizone induces similar demyelination in male and female C57BL/6 mice and results in disruption of the estrous cycle. J Neurosci Res 2010;88:391-402.
241. Basser PJ, Pierpaoli C. Microstructural and physiological features of tissues elucidated by quantitative-diffusion-tensor MRI. J Magn Reson B 1996;111:209-19.
242. Filippi M, Dousset V, McFarland HF, Miller DH, Grossman RI. Role of magnetic resonance imaging in the diagnosis and monitoring of multiple sclerosis: consensus report of the White Matter Study Group. J Magn Reson Imaging 2002;15:499-504.
243. Zhang H, Schneider T, Wheeler-Kingshott CA, Alexander DC. NODDI: Practical in vivo neurite orientation dispersion and density imaging of the human brain. NeuroImage 2012;61:1000-16.

244. Fukutomi H, Glasser MF, Zhang H, Autio JA, Coalson TS, Okada T, Togashi K, Van Essen DC, Hayashi T. Neurite imaging reveals microstructural variations in human cerebral cortical gray matter. Neuroimage 2018;182:488-99.
245. Sharma S, Zhang Y. Fourier transform power spectrum is a potential measure of tissue alignment in standard MRI: A multiple sclerosis study. PLoS One 2017;12:e0175979.
246. Tagge I, O'Connor A, Chaudhary P, Pollaro J, Berlow Y, Chalupsky M, Bourdette D, Woltjer R, Johnson M, Rooney W. Spatio-Temporal Patterns of Demyelination and Remyelination in the Cuprizone Mouse Model. PLoS One 2016;11:e0152480.
247. Jones DK, Horsfield MA, Simmons A. Optimal strategies for measuring diffusion in anisotropic systems by magnetic resonance imaging. Magn Reson Med 1999;42:515-25.
248. Jenkinson M, Smith S. A global optimisation method for robust affine registration of brain images. Med Image Anal 2001;5:143-56.
249. Robitaille N, Mouiha A, Crepeault B, Valdivia F, Duchesne S, The Alzheimer's Disease Neuroimaging I. Tissue-based MRI intensity standardization: application to multicentric datasets. Int J Biomed Imaging 2012;2012:347120.
250. Begin S, Belanger E, Laffray S, Aube B, Chamma E, Belisle J, Lacroix S, De Koninck Y, Cote D. Local assessment of myelin health in a multiple sclerosis mouse model using a 2D Fourier transform approach. Biomed Opt Express 2013;4:2003-14.
251. Stefanovic D, Stefanovic M, Lalosevic D. Use of eriochrome cyanine R in routine histology and histopathology: is it time to say goodbye to hematoxylin? Biotech Histochem 2015;90:461-9.
252. Zarella MD, Yeoh C, Breen DE, Garcia FU. An alternative reference space for H&E color normalization. PLoS One 2017;12:e0174489.
253. Mollink J, Kleinnijenhuis M, Cappellen van Walsum AV, Sotiropoulos SN, Cottaar M, Mirfin C, Heinrich MP, Jenkinson M, Pallebage-Gamarallage M, Ansorge O, Jbabdi S, Miller KL. Evaluating fibre orientation dispersion in white matter: Comparison of diffusion MRI, histology and polarized light imaging. Neuroimage 2017;157:561-74.
254. Bai CB, Sun S, Roholt A, Benson E, Edberg D, Medicetty S, Dutta R, Kidd G, Macklin WB, Trapp B. A mouse model for testing remyelinating therapies. Exp Neurol 2016;283:330-40.
255. Clemons TD, Bradshaw M, Toshniwal P, Chaudhari N, Stevenson AW, Lynch J, Fear MW, Wood FM, Iyer KS. Coherency image analysis to quantify collagen architecture: implications in scar assessment. Rsc Adv 2018;8:9661-9.
256. Skripuletz T, Lindner M, Kotsiari A, Garde N, Fokuhl J, Linsmeier F, Trebst C, Stangel M. Cortical demyelination is prominent in the murine cuprizone model and is strain-dependent. Am J Pathol 2008;172:1053-61.
257. Colgan N, Siow B, O'Callaghan JM, Harrison IF, Wells JA, Holmes HE, Ismail O, Richardson S, Alexander DC, Collins EC, Fisher EM, Johnson R, Schwarz AJ, Ahmed Z, O'Neill MJ, Murray TK, Zhang H, Lythgoe MF. Application of neurite orientation dispersion and density imaging (NODDI) to a tau pathology model of Alzheimer's disease. Neuroimage 2016;125:739-44.
258. Medina-Rodriguez EM, Bribian A, Boyd A, Palomo V, Pastor J, Lagares A, Gil C, Martinez A, Williams A, de Castro F. Promoting in vivo remyelination with small molecules: a neuroreparative pharmacological treatment for Multiple Sclerosis. Sci Rep 2017;7:43545.
259. DeLuca GC, Williams K, Evangelou N, Ebers GC, Esiri MM. The contribution of demyelination to axonal loss in multiple sclerosis. Brain 2006;129:1507-16.

260. Grussu F, Schneider T, Yates RL, Zhang H, Wheeler-Kingshott C, DeLuca GC, Alexander DC. A framework for optimal whole-sample histological quantification of neurite orientation dispersion in the human spinal cord. J Neurosci Methods 2016;273:20-32.
261. Alizadeh A, Dyck SM, Karimi-Abdolrezaee S. Myelin damage and repair in pathologic CNS: challenges and prospects. Front Mol Neurosci 2015;8:35.
262. Phillips KA, Stimpson CD, Smaers JB, Raghanti MA, Jacobs B, Popratiloff A, Hof PR, Sherwood CC. The corpus callosum in primates: processing speed of axons and the evolution of hemispheric asymmetry. Proc Biol Sci 2015;282:20151535.
263. Witelson SF. Hand and sex differences in the isthmus and genu of the human corpus callosum. A postmortem morphological study. Brain 1989;112 (Pt 3):799-835.
264. Sepehrband F, Alexander DC, Kurniawan ND, Reutens DC, Yang Z. Towards higher sensitivity and stability of axon diameter estimation with diffusion-weighted MRI. NMR Biomed 2016;29:293-308.
265. De Santis S, Bastiani M, Droby A, Kolber P, Zipp F, Pracht E, Stoecker T, Groppa S, Roebroeck A. Characterizing Microstructural Tissue Properties in Multiple Sclerosis with Diffusion MRI at 7 T and 3 T: The Impact of the Experimental Design. Neuroscience 2019;403:17-26.
266. Schmierer K, Wheeler-Kingshott CAM, Boulby PA, Scaravilli F, Altmann DR, Barker GJ, Tofts PS, Miller DH. Diffusion tensor imaging of post mortem multiple sclerosis brain. Neuroimage 2007;35:467-77.
267. Jespersen SN, Bjarkam CR, Nyengaard JR, Chakravarty MM, Hansen B, Vosegaard T, Ostergaard L, Yablonskiy D, Nielsen NC, Vestergaard-Poulsen P. Neurite density from magnetic resonance diffusion measurements at ultrahigh field: Comparison with light microscopy and electron microscopy. Neuroimage 2010;49:205-16.
268. Johnson PD, Besselsen DG. Practical aspects of experimental design in animal research. ILAR J 2002;43:202-6.
269. Brusa A, Jones SJ, Plant GT. Long-term remyelination after optic neuritis: A 2-year visual evoked potential and psychophysical serial study. Brain 2001;124:468-79.
270. Hickman SJ, Toosy AT, Jones SJ, Altmann DR, Miszkiel KA, MacManus DG, Barker GJ, Plant GT, Thompson AJ, Miller DH. A serial MRI study following optic nerve mean area in acute optic neuritis. Brain 2004;127:2498-505.
271. Bennett JL, Nickerson M, Costello F, Sergott RC, Calkwood JC, Galetta SL, Balcer LJ, Markowitz CE, Vartanian T, Morrow M, Moster ML, Taylor AW, Pace TW, Frohman T, Frohman EM. Re-evaluating the treatment of acute optic neuritis. J Neurol Neurosurg Psychiatry 2015;86:799-808.
272. Grauer O, Offenhäusser M, Schmidt J, Toyka KV, Gold R. [Glucocorticosteroid therapy in optic neuritis and multiple sclerosis. Evidence from clinical studies and practical recommendations]. Nervenarzt 2001;72:577-89.
273. Hickman SJ, Brierley CM, Brex PA, MacManus DG, Scolding NJ, Compston DA, Miller DH. Continuing optic nerve atrophy following optic neuritis: a serial MRI study. Mult Scler 2002;8:339-42.
274. Kapoor R, Davies M, Blaker PA, Hall SM, Smith KJ. Blockers of sodium and calcium entry protect axons from nitric oxide-mediated degeneration. Ann Neurol 2003;53:174-80.
275. Trapp BD, Peterson J, Ransohoff RM, Rudick R, Mork S, Bo L. Axonal transection in the lesions of multiple sclerosis. N Engl J Med 1998;338:278-85.

276. Petzold A, Rejdak K, Plant GT. Axonal degeneration and inflammation in acute optic neuritis. J Neurol Neurosurg Psychiatry 2004;75:1178-80.
277. Duncan ID, Brower A, Kondo Y, Curlee JF, Jr., Schultz RD. Extensive remyelination of the CNS leads to functional recovery. Proc Natl Acad Sci U S A 2009;106:6832-6.
278. Burman J, Raininko R, Fagius J. Bilateral and recurrent optic neuritis in multiple sclerosis. Acta Neurol Scand 2011;123:207-10.
279. Hickman SJ, Wheeler-Kingshott CA, Jones SJ, Miszkiel KA, Barker GJ, Plant GT, Miller DH. Optic nerve diffusion measurement from diffusion-weighted imaging in optic neuritis. AJNR Am J Neuroradiol 2005;26:951-6.
280. Sun HH, Wang D, Zhang QJ, Bai ZL, He P. Magnetic resonance diffusion tensor imaging of optic nerve and optic radiation in healthy adults at 3T. Int J Ophthalmol 2013;6:868-72.
281. Timmers I, Roebroeck A, Bastiani M, Jansma B, Rubio-Gozalbo E, Zhang H. Assessing Microstructural Substrates of White Matter Abnormalities: A Comparative Study Using DTI and NODDI. PLoS One 2016;11.
282. Zhang Y, Moore GR, Laule C, Bjarnason TA, Kozlowski P, Traboulsee A, Li DK. Pathological correlates of magnetic resonance imaging texture heterogeneity in multiple sclerosis. Ann Neurol 2013;74:91-9.
283. Kahraman T, Savci S, Coskuner Poyraz E, Ozakbas S, Idiman E. Utilization of the Expanded Disability Status Scale as a distinctive instrument for walking impairment in persons with multiple sclerosis with mild disability. NeuroRehabilitation 2016;38:7-14.
284. Li M, Li J, He H, Wang Z, Lv B, Li W, Hailla N, Yan F, Xian J, Ai L. Directional diffusivity changes in the optic nerve and optic radiation in optic neuritis. Br J Radiol 2011;84:304-14.
285. Jenkinson M, Smith S. A global optimisation method for robust affine registration of brain images. Medical Image Analysis 2001;5:143-56.
286. Jenkinson M. Image registration and Motion Correction.
287. van de Pavert SH, Muhlert N, Sethi V, Wheeler-Kingshott CA, Ridgway GR, Geurts JJ, Ron M, Yousry TA, Thompson AJ, Miller DH, Chard DT, Ciccarelli O. DIR-visible grey matter lesions and atrophy in multiple sclerosis: partners in crime? J Neurol Neurosurg Psychiatry 2016;87:461-7.
288. Calabrese M, Favaretto A, Martini V, Gallo P. Grey matter lesions in MS: from histology to clinical implications. Prion 2013;7:20-7.
289. Mukaka MM. Statistics corner: A guide to appropriate use of correlation coefficient in medical research. Malawi Med J 2012;24:69-71.
290. Martínez-Lapiscina EH, Fraga-Pumar E, Pastor X, Gómez M, Conesa A, Lozano-Rubí R, Sánchez-Dalmau B, Alonso A, Villoslada P. Is the incidence of optic neuritis rising? Evidence from an epidemiological study in Barcelona (Spain), 2008-2012. Journal of Neurology 2014.
291. Burton JM, Kimball S, Vieth R, Bar-Or A, Dosch HM, Cheung R, Gagne D, D'Souza C, Ursell M, O'Connor P. A phase I/II dose-escalation trial of vitamin D3 and calcium in multiple sclerosis. Neurology 2010;74:1852-9.
292. Malik MT, Healy BC, Benson LA, Kivisakk P, Musallam A, Weiner HL, Chitnis T. Factors associated with recovery from acute optic neuritis in patients with multiple sclerosis. Neurology 2014;82:2173-9.
293. Prager JM, Thomas C, Ankenbrandt WJ, Meyer JR, Gao Y, Ragin A, Sidharthan S, Hutten R, Wu YG. Association of white matter hyperintensities with low serum 25-hydroxyvitamin D levels. AJNR Am J Neuroradiol 2014;35:1145-9.

294. Kolbe S, Chapman C, Nguyen T, Bajraszewski C, Johnston L, Kean M, Mitchell P, Paine M, Butzkueven H, Kilpatrick T, Egan G. Optic nerve diffusion changes and atrophy jointly predict visual dysfunction after optic neuritis. Neuroimage 2009;45:679-86.
295. B. S, L. B-S, S. C, S. F. Optic nerve sheath diameter on MR imaging: Establishment of norms and comparison of pediatric patients with idiopathic intracranial hypertension with healthy controls. American Journal of Neuroradiology 2012;33:366-9.
296. Naismith RT, Xu J, Tutlam NT, Lancia S, Trinkaus K, Song SK, Cross AH. Diffusion tensor imaging in acute optic neuropathies: predictor of clinical outcomes. Arch Neurol 2012;69:65-71.
297. Chen J, Zhu L, Li H, Lu Z, Chen X, Fang S. Diffusion tensor imaging of occult injury of optic radiation following optic neuritis in multiple sclerosis. Exp Ther Med 2016;12:2505-10.
298. Absinta M, Sati P, Reich DS. Advanced MRI and staging of multiple sclerosis lesions. Nat Rev Neurol 2016;12:358-68.
299. Fisniku LK, Brex PA, Altmann DR, Miszkiel KA, Benton CE, Lanyon R, Thompson AJ, Miller DH. Disability and T2 MRI lesions: a 20-year follow-up of patients with relapse onset of multiple sclerosis. Brain 2008;131:808-17.
300. Nakamura Y, Gaetano L, Matsushita T, Anna A, Sprenger T, Radue EW, Wuerfel J, Bauer L, Amann M, Shinoda K, Isobe N, Yamasaki R, Saida T, Kappos L, Kira JI. A comparison of brain magnetic resonance imaging lesions in multiple sclerosis by race with reference to disability progression. J Neuroinflammation 2018;15:255.
301. Brex PA, Ciccarelli O, O'Riordan JI, Sailer M, Thompson AJ, Miller DH. A longitudinal study of abnormalities on MRI and disability from multiple sclerosis. N Engl J Med 2002;346:158-64.